Corrosion Effects on the Ductile Fracture, Strength and Reliability of Membranes, Plates and Shells

by

Weiwei Yu

A dissertation submitted in partial fulfillment
of the requirements for the degree of
Doctor of Philosophy
(Naval Architecture and Marine Engineering)
in The University of Michigan
2009

Doctoral Committee:

Associate Professor Dale G. Karr, Chair
Professor Michael M. Bernitsas
Assistant Professor Samantha Hayes Daly
Pedro M. Vargas, Chevron Energy Technology Company

To my dearest grandparents, Xinwen Liu and Shufang Zheng.

ACKNOWLEDGEMENTS

Thank you to my advisor Prof. Karr for your invaluable vision, support, patience and leadership. Without these, I could not have been achieved what I have already. Thank you also for being a good life instructor, from which I have gained strength. Thank you Prof. Troesch for helping me out academically and personally. Many opportunities will not favor me without your support, trust and introduction. I am so honored to be your student.

Thank you Prof. Perlin, Prof. Bernitsas, Prof. Lamb, Prof. Singer, Prof. Smith, Prof. Sun, and Prof. Vlahopoulos from the Department of Naval Architecture and Marine Engineering; Prof. Samantha H. Daly and Prof. Jwo Pan from the Department of Mechanical Engineering; Prof. Peter David Washabaugh from the Department of Aerospace Engineering and Ms. Verena Ward from Art, Architecture and Engineering Library for all your kind academic help and true support. Many thanks to Shanna Jessee, Kathy Stolaruk, Kay Drake and Suzanne Taylor for helping me on the academic life and making me feel studying in the department as home.

I also want to give my sincerest gratitude to: Aimin Wang, Zhigang Tian, Ying Wang, Zhen Li, Wei Wu, Yanhui Xie, Handa Xi, Hyun Chung, Ellie Kirtley, Tracy Phillips, Piotr Bandyk, Jingting Guo, Oscar Tascon, Nabanita Datta, Kamaldev Raghavan, Jing Zhou, Zheng Zhang, Yong Lei, Yang Jiang, Yunyan Tao, Zhibin Yang, Shanshan Hu, Zhe Huang, Linlin Shi, Jing Tang, Hui Wang, Hongtao Ding, Yu

Liao, Yingbai Zhu, Vladimir Calugaru, Alana Leahy-Dios, Chia-Yin Lin, Jing-May Lin to help me along the way. Two special friends, Kristian Liu and Che-Chun(Jim) Chang gave me their unwavering support all the time. Kristina, I so enjoy each time we meet each other and share our experience. You always set a good example to me to widen my vision. Jim, I so cherish the family-member-kind friendship established between us. You are always supporting me, comforting me and trusting me, from which I have acquired unlimited strength. I feel extreme happy to have grown up with you within these years.

As I spent totally almost 12 months in industry during summers, supervisors and mentors I met in industry helped me re-recognize and re-establish myself. Some of them become life-long friends. They are: Neal Fine and Dave Kring from Flight Safety Technologies; J.-C. Sun, Nancy Sun, Ray Laio from American Bureau of Shipping; Dr. Sandstrom, Scott Slocum, Karina Molina from ExxonMobil Upstream Research Company; Jen-Hua Chen, Hugh Thompson, Pedro Vargas, Guangyu Wu, Paul Devlin, Hailing An from Chevron Energy Technology Company. I especially appreciate the funding assistance for the pipe bending experiment from Chevron Energy Technology Company.

Last but not least, I want to thank tremendous times deeply to my families, especially to my dearest parents: Shengliang Yu and Yanping Liu. Without your love, I am not able to go this far.

TABLE OF CONTENTS

LIST OF FIGURES

Figure

LIST OF TABLES

Table

ABSTRACT

Corrosion Effects on the Ductile Fracture, Strength and Reliability of Membranes, Plates and Shells

by

Weiwei Yu

Chair: Dale G. Karr

Corrosion is a degradation of material properties and strength due to interactions with the environment. This dissertation details the analyses of corrosion effects on two failure modes: ductile fracture and bending strength of membranes, plates and shells. Furthermore, corrosion induced stress or strain concentration effects are incorporated in reliability studies.

Annular elastic membrane deformation is studied analytically. Large out-of-plane ship hull deformation in ship grounding or collision is often analyzed by using membrane theory. It has been found that older ships with corrosion are more susceptible to fracture in grounding or collision. Therefore, corrosion effects on ductile fracture initiation are studied next. Corrosion effects inducing strain localization are revealed by a $3D$ model based on the finite element method. The relationship between local and overall strain and model size effects are examined for a rectangular plate under uniaxial and biaxial tension. The ductile fracture of corroded plates is also studied under different pit intensities, distributions and loading conditions.

Corrosion also degrades the bending capacity of pipelines. Previous research focused mainly on burst capacity of corroded pipelines. Key points of finite element analyses of corroded pipelines in bending are addressed in detail. An experimental testing program is fully reported and validates the finite element analysis results.

Bending strength reduction because of corrosion has been revealed. Secondary effects in the experimental testing are also discussed.

Finally, corrosion induced high local stress and strain levels are evaluated by means of stress and strain concentrations. Both analytical and numerical analyses are performed including the use of Neuber's stress concentration theory. Such studies are further incorporated into the reliability analyses of corroded plates. Structural failure probability and partial safety factors are calculated by considering the randomness of corrosion geometry and of the applied nominal strain. A reliability study is applied on a corroded bottom shell of a double bottom oil tanker in ship grounding.

CHAPTER 1

Introduction

Ships and offshore structures are subjected to numerous mechanisms which degrade their mechanical properties and threaten their integrity, safety and service life. These include wear, stress cycles (fatigue), mechanical shock and impact, creep, rupture, embrittlement and corrosion. Among them, corrosion is one of the most critical degrading mechanisms of structural strength. Moreover, corrosion of most metals is often an inevitable process. Corrosion compromises structural integrity by reducing fracture elongation and strength, yield and ultimate strength, and fatigue life. When localized or pit corrosion occurs, strength reduction can be difficult to establish because of the complicated effects of uneven surfaces and uneven material properties on the stress fields and failure modes of the structure. In order to accurately estimate hull structure life, it is important to understand and evaluate corrosion effects on overall ductile fracture, bending capacity and the corresponding local strength.

Most ship structures are composed of thousands of plates of a variety of shapes. In industry, it is routine to analyze stress and strain distributions, yielding, and fracture in these structures. Classification rules from different shipping bureaus are used in design applications. Finite element modeling is also a method to estimate local and overall strength as well as to verify rule based designs. Depending on combined body,

machinery, cargo, and wave loading, the failure mode of hull structures may vary and be complex.

Many uncertain factors are presented in the above mentioned loading and environmental conditions. Additionally, structural strength itself is affected by many uncertain quantities. For example, the material defect geometry and its propagation process all should be quantified by random variables. The randomness of the structure and from environmental conditions influence the structure failure analysis. Therefore, probability based analysis is becoming more preferred over the deterministic analysis to predict structure failure.

One common example for ship hull structure study is in ship grounding or collision. When ship grounding or collision occurs, ship hull structures are very likely to fracture. If groundings or collisions occur on oil tankers, such accidents will also lead to severe environment pollution. Therefore, it is very necessary to prevent fracture of ship hull structures when groundings or collisions happen.

As it is the large out-of-plane deformations that probably lead to fracture, we first focus on such large deformation analysis. A very common assumption in the study of such large out-of-plane deformation is that in-plane deformation is neglected; so membrane theory can be applied. Membranes are defined as thin plates with a thickness normally less than one twentieth of the characteristic dimension of the plate. Due to its geometric features, a membrane cannot sustain significant bending and its flexural rigidity is neglected. When large deformations occur in thin plates, in-plane membrane stress will overcome the bending stress and become more important for plate failure. Such membrane stress develops when ship hulls undergo severe impact, grounding, collision or tearing. When membrane stresses dominate, hull plantings may also undergo large plastic deformation.

The structural idealizations involving elasto-plastic membrane deformation can be highly simplified, for example as a circular membrane model subject to vertical loadings. A first step in understanding the large membrane deformation is elastic membrane analyses. The fundamental elastic membrane theories are the Föppl [32] and Hencky [44] nonlinear membrane theories. Föppl's theory laid the foundation for nonlinear elastic membrane analyses under small deformation and small strains, such that the linear elastic stress-strain relations are valid. Hencky was the first person to apply Föppl's theory to an important particular application. He provided power series solutions for a flat circular membrane under uniform vertical pressure in which the flexural rigidity is neglected. More circular membrane analyses will be presented in Chapter 2. My research focuses on the analytical study of an annular membrane, as it allows comparing annular membrane deformation to that of, for example, a circular membrane with a corrosion pit in the center to examine the strain distribution along the inner circumference of a membrane.

Membrane theory has been widely used in marine, mechanical, civil and biomechanical engineering applications. The thin plates on ships may be modeled as membranes. Although these plates are sometimes not really "thin", under grounding, collision or dynamic loading conditions their behavior (large plastic out-of-plane deformation) can be better approximated by membrane theory than by plate theory. In mechanical engineering, one common application is the indentation problem [121]. Ponding pressures acting on a circular membrane as a result of the weight of a liquid filling the space created by the deflection of a membrane is also important in civil engineering design, for example in roofs [112]. Besides those applications, membrane theory is employed in biomechanical engineering. Clinical interventions, for example a rigid fixation during a surgery, result in distributed stress and strain fields with

potentially strong gradients in tissues. To design better surgical procedures, membrane analyses are applied to understand cellular responses to altered mechanical stress [25].

In the study of ship hull deformation in grounding or collision, another finding is that older ships are more susceptible to fracture than newer ships. One reason for this is due to corrosion. Corrosion is a common phenomenon in aging ships, necessitating a reasonable strength and service duration estimation. Usually, ships in service for longer than $10-15$ years require a full inspection. Corrosion degrades the structural resistance to fracture, so efforts need to be put on the study of corrosion effects on fracture, especially for ship hull or offshore structures.

Based on the severity and intensity of corrosion, the material loss can be converted into an overall reduction in plate thickness and a corresponding decrease in the strength of the structure. Although the concept of an overall thickness reduction is simple to apply, it may be inaccurate as some important local phenomena may be overlooked. Another phenomenon of pit corrosion is that it is susceptible to strain localization. *There has been no generally accepted method for establishing acceptable levels of strain for corroded steel plates.* The lack of relation between local strain or stress tolerance, and global average strain or stress, motivates my research on strength reduction and fracture initiation of pit corroded plates under various loading conditions. In this sense, membrane analysis and fracture estimation are valuable supplements to linear plate bending analyses. To fully understand and visualize corrosion effects, one must understand plate deformation and fracture behavior both with and without structural initial imperfections.

The effects of corrosion on aging hull plating has been examined to a limited extent in the existing literature. Material defects are known to affect the strain-to-

failure of ductile metals by notably increasing plastic localization and reducing the ship hull's buckling strength [71, 72], shear strength [74] and collapse strength [72]. Success lies in conducting experimental tests on corroded plates and verifying results from finite element analyses. Nakai et al. [71, 72] conducted experimental testing on tensile strength and ultimate collapse strength of pit-corroded plates. He compared test results to those from finite element analyses with good agreement. He found that "tensile strength decreases gradually while the elongation decreases dramatically in pitted plates" [75]. Additionally, his work indicates that finite element analyses are able to simulate the plate deformation with pit corrosion [75].

An empirical formula for strength reduction factor was found in the literature [82, 83]. However, the application of the formula is quite limited. A corroded plate compressive ultimate strength reduction factor is introduced by taking the smallest cross sectional area into consideration. Furthermore, from experimental and numerical analyses, a plate under pit corrosion is converted to one with an equivalent plate thickness under general corrosion with the same strength reduction [82]. This conversion provides an alternate accounting for corrosion effects.

Offshore structures, for example, oil platform and oil/gas pipelines, are other types of structures that are highly susceptible to corrosion. As the geometry features of such in- and out-of-water structures, corrosion effects on shell structures are of special interest in studying the corrosion effects on pipelines. For pipelines, internal and external pressures, and bending moments are regarded as the most important loading conditions. Pipelines sustain huge external pressures from water and soil, internal pressures from transmitted oil or gas and bending moments due to thermal expansion and curved lay-out. When these pipes are corroded from either external or internal (or both), burst and bending capacities are decreased; thus, the structural

integrity is significantly affected. Therefore, guidelines are needed for the estimation and calculation of these reductions.

The American Society of Mechanical Engineering (ASME) B31G, modified ASME B31G [8] and Det Norske Veritas (DNV) $RP - F101$ provide coded methods to evaluate the structural integrity of corroded pipelines. The above methods are all based on the analytical analyses of pipelines under internal and external pressures. Besides these guidelines, Zheng et al. [125] and Kim et al. [53, 101] also proposed an analytical formula for the burst capacity of corroded pipelines. Under similar loading conditions, Roy et al. [94], Katsumasa et al. [68] and Shinji et al. [2] conducted experimental tests of various size pipes. They analyzed corroded pipelines failure modes and conducted parametric studies regarding the failure of corroded pipes. These analyses provide a valuable database to compare to and verify the numerical results.

However, the above mentioned analyses focused on the burst capacity of corroded pipelines but not the bending capacity. Even though some literature does cover bending capacities calculation, the calculations are applied for pipes in the chemical refinery field, which have a very large diameter to wall thickness ratio ($D/t \approx 100$). The dimension of these pipes are quite different from those used in the oil/gas industry, where D/t is typically about 20.

Conventional deterministic analyses of corrosion effects on ductile fracture initiation and bending capacity of ship and offshore structures are meaningful in that they reflect the fundamental corrosion compromising effects on structure mechanical response. The qualitative prediction of changes in the structural response caused by corrosion helps to efficiently control and prevent fracture in ship grounding or collision. However, corrosion distribution, geometry and propagation are random and

affected by environment, loading conditions, material properties and other factors. This randomness lead to another concern in the ship grounding or collision. That is, how much more susceptible to fracture during grounding are older ships as compared to newer ships? Hence, to answer this question and also approach actual scenarios closer, uncertainties in structural strength, response and loading should be considered. Thus, a probability based reliability analysis is a logical extension beyond the deterministic study.

Reliability analysis has been widely used in structural system design, test and maintenance to estimate structure failure probability. The analysis is related to the definition of a limit state. The limit state design was developed by the Comité Européen du Béton and the Fédération Internationale de la Précontrainte [56]. Statistical methods are employed to reveal different uncertainty levels of these random variables in the limit state design. The cumulative effect of these various uncertainty levels affect the structure safety level. A limit state function is usually used to express critical load-strength (resistance) effects. Through a limit state function, structural integrity is quantified by a reliability safety index corresponding to the probability of failure.

Based on the classification system of the Joint Committee on Structural Safety [46, 47], there are three different structure reliability analyses: Level 3, Level 2 and Level 1. A reliability safety index directly related to the failure probability is included in both Level 2 and Level 1 studies. Moreover, partial safety factors quantifying each individual random variable's safety concern is provided in the Level 1 study. General methods to execute the above reliability analyses are: the first-order reliability method (FORM) method, the second-order reliability method (SORM) and Monte Carlo (MC) method [12]. The first two are analytical methods, with the

merits of simplicity for application and less cost of computational recourses. MC is a simulation method, which generally yields a high level of accuracy, but is often computationally expensive.

In the field of naval architecture and marine engineering, reliability analysis has been given much attention, especially because of the stochastic nature of the marine environment. For example, Dunbar et al. [5], Garbatov [105] and Guedes Soares [106] presented time variant formulations to account for the effect of corrosion and fatigue on the reliability of ship hulls. The degrading effect of general corrosion is reflected in the decreased thickness of the plating, which in turn decreases the moment of inertia of the ship cross section and thus induces higher stress levels for the same applied bending moments. The formulation is able to accurately assess the degrading effects of both crack growth due to fatigue and corrosion on instantaneous and time-dependent reliability. Parunov and Guedes Soares [86] further considered the reinforcement of initial designed members and calculated ultimate failure probability of both initial designed and reinforced ship hull. The calculation is performed separately for two independent failure modes: sagging and hogging. Both sensitivity and parametric studies are performed and the results show that the ultimate strength is the most important random variable for the reliability calculation.

Corrosion affects the overall ship hull bending capacity by reducing plates thickness. Corrosion can also decrease the structure capacity locally, which can directly lead to failure. In ship grounding or collapse, large out-of-plane plastic deformation occurs. When corrosion appears on such highly deformed ship hull plates, high strain localization may appear on the corroded plate, exceeding the fracture strain and directly resulting in fracture. The reliability study of local failure considering corrosion effects is also important, but has not been discussed a great deal in existing

literature.

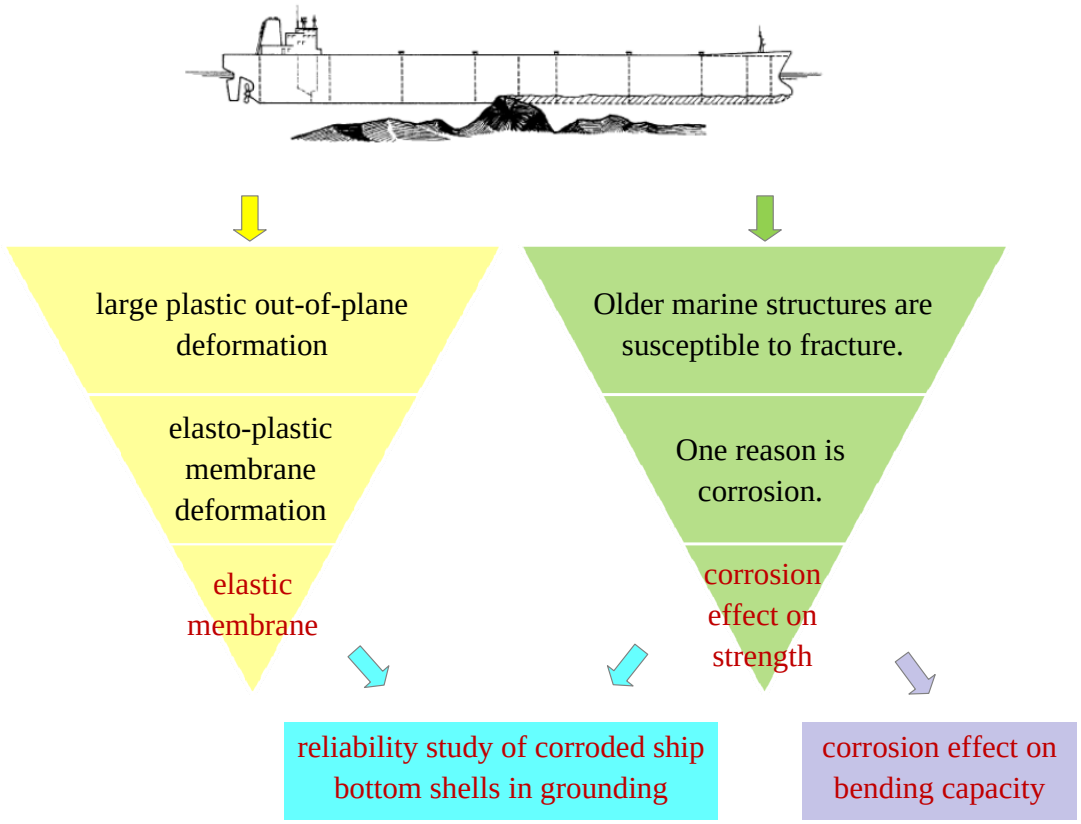

Figure 1.1: Overall research structure; the ship grounding picture is from "Plate Tearing and Bottom Damage in Ship Grounding" [124]

Regarding to three main concerns in ship hull grounding or collision, the overall construction of this thesis is shown in Fig. 1.1. Here, we will first show the axisymmetrical solutions for an edge-loaded annular membrane under elastic deformation. The Föppl-Hencky nonlinear membrane theory is employed in Chapter 2 to study the axisymmetric deformation of annular elastic membranes under the assumption of small deflection. General solutions for displacements and stresses are established for arbitrary edge boundary conditions. New exact solution results are developed for central loading and edge forcing conditions. Both positive and negative radial stress solutions are found. Comparisons are made for special cases to previously known solutions with excellent agreement.

Local strain concentration and fracture strain studies are included in Chapter 3 for plates subjected to axial loading with local geometric defects caused by corrosion. A $3D$ model based on the finite element method is used for predicting the ductile fracture of plating, which also validates the application of a $1D$ three-piece model on the strain localization of pit-corroded plate. Results of the strain localization for particular corrosion states are presented for common ship hull steel ($A36$ steel). The strain to failure is shown to be dependent on the ratio of pit size to overall model length. Fracture strain is also studied under different corrosion states and loading conditions.

Chapter 4 presents the bending capacity of corroded pipelines. The corrosion effect on bending moment capacity is studied numerically and experimentally. Finite element (FE) analyses are preformed regarding various shapes of corrosion, meshing refinement levels and meshing techniques. The performed experimental tests allow deeper understanding of mechanical mechanism of corroded pipelines as well as the validation of the FE analyses. Both studies tally nicely with each other. Some issues revealed in the experimental testing need special attention: particularly the added axial tension and the end-cap effect.

Details of corrosion on ductile fracture initiation and bending capacity are fully studied in Chapters 3 and 4. Corrosion is one type of geometrical defect which causes stress concentration. Local stress and strain rapidly increasing is a phenomenon of stress/strain concentration. Therefore, in essence, the corrosion analysis can be addressed via stress concentration study. In Chapter 5, stress concentration induced by pit corrosion is first studied numerically. Neuber's study of elastic and inelastic formula is applied to the pit corrosion induced stress concentration factor calculation. The FE method is then employed to model this problem numerically and to calculate

the stress concentration factor for an semi-oblate spheroidal pit.

Furthermore, corrosion development is a process with many random factors such as the geometry and the growth rate. A realistic reflection of the corrosion effects on structure failure is to put it into the framework of reliability analysis. The reliability procedure is demonstrated in an example of a highly deformed bottom shell panel during ship grounding in Chapter 5. By knowing the analytical formula of stress concentration factor, reliability analyses are conducted to calculate the reliability safety index of the panel based on a strain control. Partial safety factors of two random variables which describe pit corrosion geometry and the effective nominal strain level are also calculated. The reliability safety index is directly related to the structural failure probability. Recommendations for using partial safety factors are provided.

CHAPTER 2

Symmetrical Solutions for Edge-Loaded Annular Elastic Membranes

The development of nonlinear elastic membrane theory began a century ago with the work of Föppl [32]. Within this theory, strains are presumed to be small enough that linear elastic stress-strain relationships are valid. The nonlinearity arises from the effects of small rotations of membrane elements. This nonlinearity is also present in the plate theory attributed to Von Karman [49] and Way [115], which coupled the effects of bending and in-plane stretching. An important particular application of Föppl's theory is that by Hencky [44]. Hencky provided power series solutions for a flat circular membrane under uniform vertical pressure in which the flexural rigidity is neglected.

A more general theory applicable for axisymmetric deformation including large rotations was developed by Reissner [91, 92]. The range of applicability of the Föppl-Hencky theory and the Reissner theory for flat annular membrane problems was provided by Weinitschke [116]. Dickey [27] derived an exact theory for a plane circular membrane subjected to a vertical pressure, showing that the Föppl theory corresponded to the first term expansion for the exact theory.

The solutions to the nonlinear elastic membrane problem vary according to the methods applied. Dickey [26] employed a numerical integration scheme to find ax-

isymmetric solutions for a circular membrane under a vertical pressure. Weinitschke [117] applied an iterative method to develop detailed analyses of an annular membrane under surface and edge loads, in which existence and uniqueness of tensile and compressive conditions were examined. Callegari and Reiss [20] applied a shooting method to solve boundary value problems for axisymmetric deformation of a circular membrane, like Weinitschke, examining existence and uniqueness. Kelkar, Elber and Raju [50] used a finite difference technique to analyze a circular membrane with fixed peripheral edges, and found displacement and stresses under three different loading conditions. Grabmüllen and Novak [36] developed a refined integral equation solution technique, proving that tensile solutions may cease to exist when large radial displacements are prescribed at the inner radius. As discussed in Section 2.2, this phenomenon is consistent with our findings.

Most recently, Plaut studied the large deformation [88] and vibration [89] of linear elastic annular and circular membranes under radial, transverse and torsional loading conditions. He compared displacements, strains, stress resultants by considering three different theories: Föppl theory, Reissner's theory and a generalized Reissner's theory [88]. He discussed solutions by different boundary conditions according to different industry applications and further addressed the membrane instability issues under certain boundary conditions. Especially, he studied torsional deformation of an annular membrane, which is not included in my work. Some of his conclusions emphasized the annular membrane deformation and its dependency on Poisson's ratio. However, he mentioned available closed-form solutions only for Poisson's ratio $\nu = \frac{1}{3}$. Closed-form solutions for all possible Poisson's ratios are developed in this thesis.

In this study, we develop new exact axisymmetric solutions for annular membranes

subjected to edge forcing, applying the Föppl theory. We follow closely the approach of Schwerin [96], who first presented some exact solutions for annular membrane problems for loading and edge conditions. Of particular interest is Schwerin's analysis of the problem of an elastic membrane subjected to a vertical force acting at the interior of the membrane. Analytical solutions were given with Poisson's ratio less than or equal to one third. Unlike Schwerin, we reduce the governing differential equations to a single nonlinear ordinary differential equation in terms of a single dependent variable. As a result of this reduction, in addition to positive stress, negative radial stress solutions are found. Closed-form solutions for Poisson's ratio larger than $\frac{1}{3}$ are also developed. These findings are also summarized in Yu and Karr [123].

Such analyses of nonlinear elastic membranes have numerous applications. For example, applications of circular membrane theory for indentation of tires were pointed out by Yang and Hsu [121]. Chen and Chang [22] analyzed ponding pressures acting on a large roof. The membrane deformation was initiated as a result of the weight of a liquid. It filled the space created by the deflection of a membrane. If the membrane's self weight is negligible relative to the liquid pressure, an unloaded outer circular region is thus developed. They developed an iterative technique to solve for the displacements in both the loaded and unloaded portions of the membrane.

Similar indentation problems arise for marine, land and air vehicles, when thin plates are subjected to impact load. A common hypothesis is that membrane stresses predominate for large deformations [28]. Circular membrane analyses are a first-order approximation of the geometry for impact experiments and analyses [50, 119].

Recent applications in clinical procedures [25, 69] include the analysis of circular holes in nonlinear circular membranes in an effort to characterize the effects of

cavities and implanted rigid fixations introduced into thin tissue. Annular membrane analysis is applied to quantify the stress and strain field change resulting from fixations. Annular membrane models are also used in mechanical testing of soft materials such as polymers, elastomers and bio-materials [97], and in the analysis of electrostatic deflection on elastic membranes for micro-electromechanical actuators [87]. Begley and Mackin [15] presented theoretical and experimental results for spherical indentation of freestanding thin films; they also compare their results with the classical Schwerin-type analyses.

2.1 Analysis

As mentioned, Schwerin [96] analyzed the problem of an elastic membrane with radial and vertical displacements u and w, respectively, equal to zero at the outer radius $r = r_a$. The central region of the membrane $0 < r < r_i$ consisted of a rigid disc subjected to a vertical force resultant of magnitude P acting at the center of the membrane. The annular region, $r_i < r < r_a$, was subjected to a uniformly distributed vertical pressure p. Given those boundary conditions, he found deformation and stress distribution on the membrane. However, his solutions were constrained to $\nu \leq \frac{1}{3}$.

In the following, in a manner similar to that of Schwerin, we develop the general axisymmetric solution to the governing differential equations of the elastic membrane with $p = 0$, as shown in Fig. 2.1. Our analysis pertains to the annular region, $r_i < r < r_a$ with loading provided by the stresses or displacements prescribed at the boundaries. Solutions for selected displacement boundary value problems are presented. For the particular case with the boundary conditions $u(r_i) = u(r_a) = w(r_a) = 0$, our solutions are the same as those found by Schwerin provided $\nu \leq \frac{1}{3}$. For these boundary conditions, we also find that solutions exist for $\nu > \frac{1}{3}$, in contrast

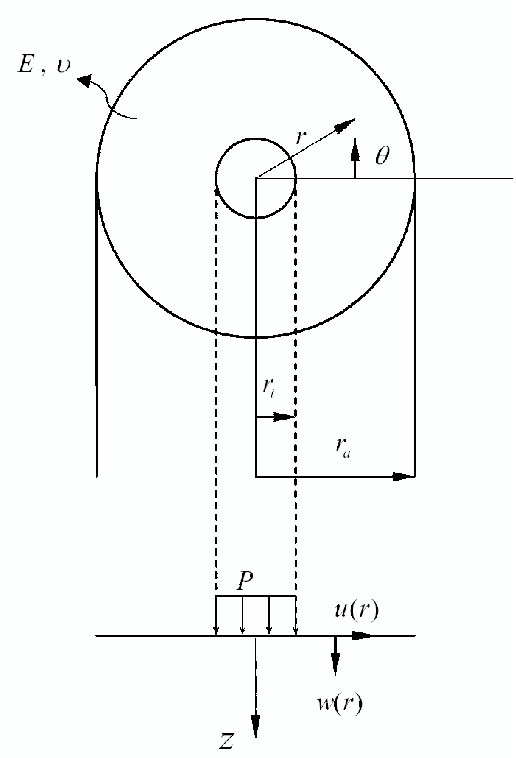

Figure 2.1: Geometry and notation for a center-loaded membrane. The inner portion provides a net vertical force P. The resulting edge-loaded annular membrane $r_i < r < r_a$ is analyzed.

to Schwerin's conclusion that axisymmetric solutions exist only for $\nu \leq \frac{1}{3}$.

For axisymmetric plane stress conditions, the circumferential strain and radial strain are related to the circumferential stress and radial stress by, respectively,

$$\varepsilon_\theta = \frac{1}{E}(\sigma_\theta - \nu\sigma_r) \tag{2.1}$$

$$\varepsilon_r = \frac{1}{E}(\sigma_r - \nu\sigma_\theta) \tag{2.2}$$

The strain-displacement relationships are

$$\varepsilon_\theta = \frac{u}{r} \tag{2.3}$$

$$\varepsilon_r = \frac{\mathrm{d}u}{\mathrm{d}r} + \frac{1}{2}(\frac{\mathrm{d}w}{\mathrm{d}r})^2 \tag{2.4}$$

where u is the displacement in the radial direction and w is the displacement in the z-direction. Substitution of the expressions for strain in Eq. 2.1 into Eq. 2.3 yields

the displacement-stress relation,

$$u = \frac{r}{E}(\sigma_\theta - \nu\sigma_r) \tag{2.5}$$

Differentiating Eq. 2.5 and substituting this result, along with Eq. 2.2, into Eq. 2.4 yields

$$\frac{1}{2}(\frac{\mathrm{d}w}{\mathrm{d}r})^2 = \frac{1}{E}[(1+\nu)(\sigma_r - \sigma_\theta) - r(\frac{\mathrm{d}\sigma_\theta}{\mathrm{d}r} - \nu\frac{\mathrm{d}\sigma_r}{\mathrm{d}r})] \tag{2.6}$$

From the summation of forces in the radial direction, equilibrium of a differential element yields

$$\frac{\mathrm{d}\sigma_r}{\mathrm{d}r} + \frac{1}{r}(\sigma_r - \sigma_\theta) = 0 \tag{2.7}$$

Summation of forces in the vertical direction yields

$$\sigma_r\frac{\mathrm{d}^2w}{\mathrm{d}r^2} + \frac{1}{r}\sigma_\theta\frac{\mathrm{d}w}{\mathrm{d}r} = 0 \tag{2.8}$$

Equations 2.6, 2.7 and 2.8 involve three nonlinear differential equations of first order in σ_r and σ_θ, and of second order in displacement w. Accordingly, in the applications that follow, the solutions involve four boundary conditions for axisymmetric deformation of the membrane.

The system of equations can be further reduced in several ways. The approach preferred most often is to introduce the stress function ϕ, from which we find,

$$\sigma_r = \frac{1}{r}\frac{\mathrm{d}\phi}{\mathrm{d}r} \tag{2.9}$$

$$\sigma_\theta = \frac{\mathrm{d}^2\phi}{\mathrm{d}r^2} \tag{2.10}$$

Then, Eq. 2.7 is satisfied identically and equations 2.6 and 2.8 may be rewritten as, respectively,

$$\frac{E}{2}(\frac{\mathrm{d}w}{\mathrm{d}r})^2 + r\frac{\mathrm{d}}{\mathrm{d}r}(\frac{\mathrm{d}^2\phi}{\mathrm{d}r^2} + \frac{1}{r}\frac{\mathrm{d}\phi}{\mathrm{d}r}) = 0 \tag{2.11}$$

and

$$\frac{\mathrm{d}}{\mathrm{d}r}(\frac{\mathrm{d}\phi}{\mathrm{d}r}\frac{\mathrm{d}w}{\mathrm{d}r}) = 0 \tag{2.12}$$

Equations 2.11 and 2.12 are special homogeneous cases of the nonlinear axisymmetric membrane theory, corresponding to a zero pressure on the membrane.

The number of governing equations 2.6, 2.7 and 2.8 can also be reduced by solving Eq. 2.7 first. It is not hard to observe from Eq. 2.7 that, σ_θ can be expressed in terms of σ_r,

$$\sigma_\theta = \frac{\mathrm{d}(r\sigma_r)}{\mathrm{d}r} \tag{2.13}$$

Substituting this result (Eq. 2.13) into Eq. 2.6 yields

$$\frac{E}{2}(\frac{\mathrm{d}w}{\mathrm{d}r})^2 + r\frac{\mathrm{d}}{\mathrm{d}r}[\sigma_r + \frac{\mathrm{d}(r\sigma_r)}{\mathrm{d}r}] = 0 \tag{2.14}$$

Also, substituting Eq. 2.13 into 2.8 yields,

$$\frac{d}{dr}[r\sigma_r\frac{\mathrm{d}w}{\mathrm{d}r}] = 0 \tag{2.15}$$

Tuan [112] used equations of this form in an analysis of ponding of circular membranes using a fourth-order Runge-Kutta method. From Eq. 2.15 and from equilibrium condition of the central disc, for the condition in which no pressure is applied to the annular region, we find

$$r\sigma_r\frac{\mathrm{d}w}{\mathrm{d}r} + \frac{P}{2\pi h} = 0 \tag{2.16}$$

Equations 2.14 and 2.16 now correspond to equations 5b and 4b, respectively, of Schwerin's article [96].

In order to further reduce the two governing equations to one, we introduce the function

$$y \equiv r^2\frac{\sigma_r}{E} \tag{2.17}$$

and substituting it into Eq. 2.14 and 2.15 yields, respectively, two equations for $y(r)$ and $w(r)$

$$\frac{1}{2}(\frac{\mathrm{d}w}{\mathrm{d}r})^2 + \frac{\mathrm{d}^2y}{\mathrm{d}r^2} - \frac{1}{r}\frac{\mathrm{d}y}{\mathrm{d}r} = 0 \tag{2.18}$$

and

$$\frac{\mathrm{d}}{\mathrm{d}r}(\frac{y}{r}\frac{\mathrm{d}w}{\mathrm{d}r}) = 0 \tag{2.19}$$

Integrating Eq. 2.19 yields the solution for the product

$$\frac{y}{r}\frac{\mathrm{d}w}{\mathrm{d}r} = 2a_1 \tag{2.20}$$

where a_1 is a constant of integration and the factor 2 is used to simplify expressions that follow. Further simplification can be achieved by introducing the new independent variable

$$x = r^2 \tag{2.21}$$

A single nonlinear ordinary differential equation for y is then found by substituting the result, Eq. 2.20, into Eq. 2.18

$$y^2\frac{\mathrm{d}^2y}{\mathrm{d}x^2} = -\frac{1}{2}a_1^2 \tag{2.22}$$

The physical significance of the constant a_1 can be interpreted by noting the net vertical force of any circular region of the membrane is

$$P = -2\pi r\frac{\mathrm{d}w}{\mathrm{d}r}\sigma_r h \tag{2.23}$$

Then from Eq. 2.17 and 2.20 we find,

$$a_1 = -\frac{P}{4\pi Eh} \tag{2.24}$$

Note that in the following we address only problems in which P, and hence a_1, are nonzero. This also implies, from Eq. 2.22, that $\frac{\mathrm{d}^2y}{\mathrm{d}x^2} < 0$. By introducing the nondimensional variable V,

$$V \equiv -K_1 y \tag{2.25}$$

where $K_1 = \frac{1}{r_a^2}\sqrt[3]{\frac{2r_a^2}{a_1^2}}$ and the nondimensional independent variable ξ,

$$\xi \equiv \frac{x}{r_a^2} \tag{2.26}$$

We can now reduce Eq. 2.22 to the equivalent form,

$$\frac{\mathrm{d}^2 V}{\mathrm{d}\xi^2} = \frac{1}{V^2} \tag{2.27}$$

By introducing

$$\rho \equiv \frac{\mathrm{d}V}{\mathrm{d}\xi} \tag{2.28}$$

we find

$$\rho \mathrm{d}\rho = \frac{1}{V^2}\mathrm{d}V \tag{2.29}$$

Integrating Eq. 2.29 yields

$$\frac{1}{2}\rho^2 = -\frac{1}{V} - \frac{a_2}{2} \tag{2.30}$$

where a second constant of integration, a_2, has been introduced. From Eq. 2.28 and 2.30, we also find

$$\mathrm{d}\xi = \pm\frac{1}{\sqrt{2}}\frac{\mathrm{d}V}{\sqrt{-\frac{1}{V} - \frac{a_2}{2}}} \tag{2.31}$$

Integration of Eq. 2.31 yields, with the introduction of a third integration constant, a_3,

$$\xi + a_3 = \pm\frac{1}{\sqrt{2}}\int \frac{\mathrm{d}V}{\sqrt{-\frac{1}{V} - \frac{a_2}{2}}} \tag{2.32}$$

The result of the integration of the right hand side of Eq. 2.32 depends upon whether a_2 is less than, greater than, or equal to zero. We introduce two parameters φ and τ for conditions in which a_2 is a nonzero variable. Both parameters help relate ξ and V in Eq. 2.32:

$$\varphi \equiv 2\cot^{-1}\left(\frac{1}{\sqrt{a_2}}\sqrt{-\frac{2}{V} - a_2}\right), \quad a_2 > 0 \quad V < 0 \tag{2.33}$$

$$\tau \equiv 2\tanh^{-1}(\frac{1}{\sqrt{-a_2}}\sqrt{-\frac{2}{V}-a_2}), \quad a_2<0 \quad V>0 \tag{2.34}$$

$$\tau \equiv 2\coth^{-1}(\frac{1}{\sqrt{-a_2}}\sqrt{-\frac{2}{V}-a_2}), \quad a_2<0 \quad V<0 \tag{2.35}$$

Equation 2.32 yields, using Eq. 2.33, 2.34 and 2.35 respectively,

$$\xi + a_3 = \pm(\frac{1}{a_2})^{\frac{3}{2}}(\sin\varphi - \varphi), \quad a_2>0 \quad V<0 \tag{2.36}$$

$$\xi + a_3 = \pm(\frac{1}{-a_2})^{\frac{3}{2}}(\sinh\tau + \tau), \quad a_2<0 \quad V>0 \tag{2.37}$$

$$\xi + a_3 = \mp(\frac{1}{-a_2})^{\frac{3}{2}}(\sinh\tau - \tau), \quad a_2<0 \quad V<0 \tag{2.38}$$

A fourth solution exists when $a_2 = 0$ in the form,

$$\xi + a_3 = \mp\frac{\sqrt{2}}{3}(-V)^{\frac{3}{2}}, \quad a_2=0 \quad V<0 \tag{2.39}$$

Expressions for V in terms of φ and τ are found from 2.33, 2.34 and 2.35 respectively,

$$V = -\frac{1}{a_2}(1-\cos\varphi), \quad a_2>0 \quad V<0 \tag{2.40}$$

$$V = -\frac{1}{a_2}(1+\cosh\tau), \quad a_2<0 \quad V>0 \tag{2.41}$$

$$V = \frac{1}{a_2}(\cosh\tau - 1), \quad a_2<0 \quad V<0 \tag{2.42}$$

Solutions for the vertical displacement are now determined from Eq. 2.20, which can be rewritten as

$$\frac{\mathrm{d}w}{\mathrm{d}\xi} = -\frac{1}{V}\sqrt[3]{2a_1r_a^2} \tag{2.43}$$

Integration of Eq. 2.43 upon substitution of either Eq. 2.39, 2.40, 2.41 or 2.42 as the case may be, yields

$$w + a_4 = \mp\sqrt[3]{2a_1r_a^2}\frac{1}{\sqrt{a_2}}\varphi, \quad a_2>0 \quad V<0 \tag{2.44}$$

$$w + a_4 = \mp\sqrt[3]{2a_1r_a^2}\frac{1}{\sqrt{-a_2}}\tau, \quad a_2<0 \quad V>0 \tag{2.45}$$

$$w + a_4 = \mp \sqrt[3]{2a_1 r_a^2} \frac{1}{\sqrt{-a_2}} \tau, \quad a_2 < 0 \quad V < 0 \tag{2.46}$$

$$w + a_4 = \mp \sqrt[3]{2a_1 r_a^2} \sqrt{-2V}, \quad a_2 = 0 \quad V < 0 \tag{2.47}$$

The constant of integration a_4 represents a vertical rigid body translation. Solutions for the horizontal displacement are now determined from Eq. 2.5, which can be rewritten as

$$u = \frac{1}{K_1 r_a} \sqrt{\xi} [\mp 2 \sqrt{-\frac{2}{V} - a_2} + \frac{V}{\xi}(1+\nu)] \tag{2.48}$$

Substitution of either Eq. 2.39, 2.40, 2.41 or 2.42 yields the radial displacement

$$u = \frac{1}{K_1 r_a} \sqrt{\xi} [\mp 2 \sqrt{a_2} \cot \frac{\varphi}{2} - \frac{(1-\cos\varphi)}{\xi a_2}(1+\nu)], \quad a_2 > 0 \quad V < 0 \tag{2.49}$$

$$u = \frac{1}{K_1 r_a} \sqrt{\xi} [\mp 2 \sqrt{-a_2} \tanh \frac{\tau}{2} - \frac{(1+\cosh\tau)}{\xi a_2}(1+\nu)], \quad a_2 < 0 \quad V > 0 \tag{2.50}$$

$$u = \frac{1}{K_1 r_a} \sqrt{\xi} [\mp 2 \sqrt{-a_2} \coth \frac{\tau}{2} + \frac{(\cosh\tau - 1)}{\xi a_2}(1+\nu)], \quad a_2 < 0 \quad V < 0 \tag{2.51}$$

$$u = \frac{1}{K_1 r_a} \sqrt{\xi} [\mp 2 \sqrt{-\frac{2}{V}} + \frac{V}{\xi}(1+\nu)], \quad a_2 = 0 \quad V < 0 \tag{2.52}$$

Note that from equations 2.17 and 2.25, V is of the opposite sign of the radial stress σ_r. Positive values of V thus correspond to negative radial stress, changing the stability state of the membrane [14, 21]. This is the first time so far, closed-form solutions are available for an explicit relating to the negative radial stress, which initiates the instability of membrane deformation.

2.2 Results and Discussion

The above equations will be solved simultaneously with regards to different values of a_2 combined with different boundary conditions. According to scenarios whether the inner radius slides outward or not, friction and frictionless cases are discussed, respectively. Furthermore, the results are compared to previous known literature studies.

2.2.1 Boundary Condition Application of Friction Case

In this section, a membrane with uniformly distributed load around an inner circumference is studied. For all the calculations shown in the following figures, we nondimensionalize the stresses $\bar{\sigma} = \frac{\sigma}{E}$, vertical force $\bar{P} = \frac{P}{Ehr_a}$, and displacements $\bar{u} = \frac{u}{r_a}$ and $\bar{w} = \frac{w}{r_a}$.

First, the relationships between vertical displacement $w(r)$ and the net force P applied uniformly around the inner circumference with various Poisson's ratios are examined. The boundary conditions of the problem are:

- $w(r_i)$ is prescribed
- $w(r_a) = 0$
- $u(r_a) = 0$
- $u(r_i) = 0$

Force-displacement relations are shown for $\frac{r_i}{r_a} = 0.5$ in Fig. 2.2. A system of simultaneous equations must be solved to obtain these results. The system of equations depends on the signs of the constant a_2 and variable V. One particular method we found efficient is to first solve for a_1 in terms of a given vertical force P using Eq. 2.24. The solution of a_1 also provides a value for K_1. Evaluating ξ at the inner and outer boundaries yields values of $\xi_1 = 0.25$ and $\xi_2 = 1$, respectively. Substituting these values into Eq. 2.36 yields two expressions for ϕ_1 and ϕ_2 as follows (assuming $a_2 > 0$):

$$0.25 + a_3 = \pm(\frac{1}{a_2})^{\frac{3}{2}}(\sin\varphi_1 - \varphi_1), \quad a_2 > 0 \tag{2.53}$$

$$1 + a_3 = \pm(\frac{1}{a_2})^{\frac{3}{2}}(\sin\varphi_2 - \varphi_2), \quad a_2 > 0 \tag{2.54}$$

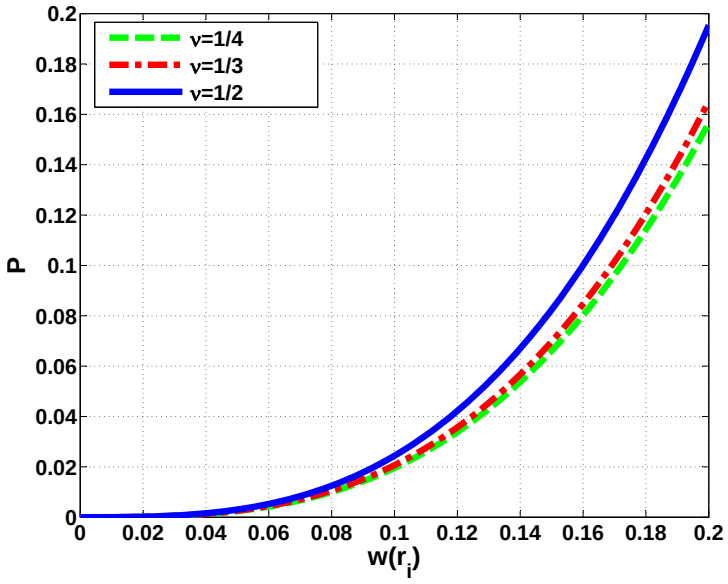

Figure 2.2: Vertical force P, applied at the inner boundary versus vertical displacement at inner boundary $w(r_i)$ for different Poisson's ratios with prescribed $w(r_a) = u(r_i) = u(r_a) = 0$, and $\frac{r_i}{r_a} = 0.5$

Two more equations arise from the boundary condition on the radial displacement at the inner and outer edges. $u(r_a) = 0$ and $u(r_i) = 0$ being zero yield, from Eq. 2.49

$$0 = \frac{1}{K_1}\sqrt{0.25}[\mp 2\sqrt{a_2}\cot\frac{\varphi_1}{2} - \frac{(1-\cos\varphi_1)}{0.25a_2}(1+\nu)] \tag{2.55}$$

$$0 = \frac{1}{K_1}[\mp 2\sqrt{a_2}\cot\frac{\varphi_2}{2} - \frac{(1-\cos\varphi_2)}{a_2}(1+\nu)] \tag{2.56}$$

The above system involves four equations 2.53, 2.54, 2.55 and 2.56 in four unknowns, ϕ_1, ϕ_2, a_2 and a_3. These equations are solved with the Matlab package [64]. The boundary condition for $w(r_a) = 0$ yields, from Eq. 2.44,

$$a_4 = \mp\sqrt[3]{2a_1}\frac{1}{\sqrt{a_2}}\varphi_2 \tag{2.57}$$

Then, we applied Eq. 2.44 to determine the displacement at the inner boundary for the given applied force, specifically:

$$w(r_i) = \mp\sqrt[3]{2a_1(0.25)^2}\frac{1}{\sqrt{a_2}}\varphi_1 - a_4 \tag{2.58}$$

Note that our solutions for Poisson's ratios $\upsilon \leq \frac{1}{3}$ are in full agreement with Schwerin's [96]. However, we find that axisymmetric solutions for $\upsilon > \frac{1}{3}$ exist as per equations 2.46 and 2.51. As indicated in Fig. 2.2, larger Poisson's ratios increase the stiffness of the membrane. Figure 2.3 shows the displacement $u(r)$ for the same boundary conditions with various Poisson's ratios with $w(r_i) = 0.1$. Note that only for $\upsilon = \frac{1}{3}$ is $u(r) = 0$. One important result by performing the analysis in this way demonstrates that maximum horizontal displacements are about three orders of magnitude smaller than the maximum vertical displacement. A logical assumption may be made that the radial displacement is zero. However, a positive radial displacement is corresponding a membrane wrinkles, which is different fundamentally different from a membrane with zero radial displacement.

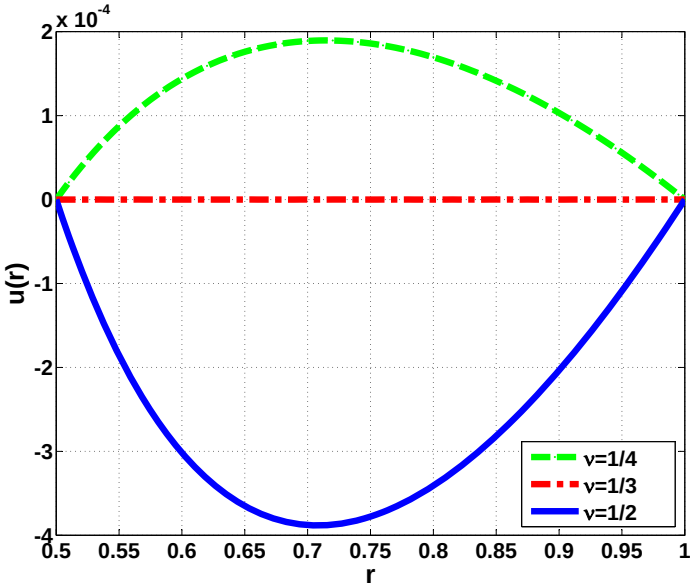

Figure 2.3: Horizontal displacement $u(r)$ for different Poisson's ratios with prescribed vertical displacement $w(r_i) = 0.1$, $w(r_a) = u(r_i) = u(r_a) = 0$, and $\frac{r_i}{r_a} = 0.5$

In order to establish the physical significance of the integration constant a_2, we studied the special case with $\frac{r_i}{r_a} = 0.5$, the outer edge displacement zero, and the

inner edge nondimensional vertical displacement fixed at 0.1. Figure 2.4 shows results as the inner radial displacement is varied for three different Poisson's ratios. Note that even when membrane sustain contraction along the radial direction (positive u values), the combined effects of positive vertical displacement and contraction along the radial direction yield overall radial tension. These solutions are often regarded as stable solutions. Moreover, the general trend is for the constant a_2 to increase as the inner radial displacement increases. This trend implies that as the radial membrane tensile strains increase, the constant a_2 decreases for a given inner vertical displacement. It is also noticeable that in general a_2 equals zero is not corresponding to zero radial displacement, except for Poisson's ratio equal to $\frac{1}{3}$. This behavior is reflected in Fig. 2.5 where Poisson's ratio is held at $\frac{1}{3}$ and the inner vertical displacement is varied.

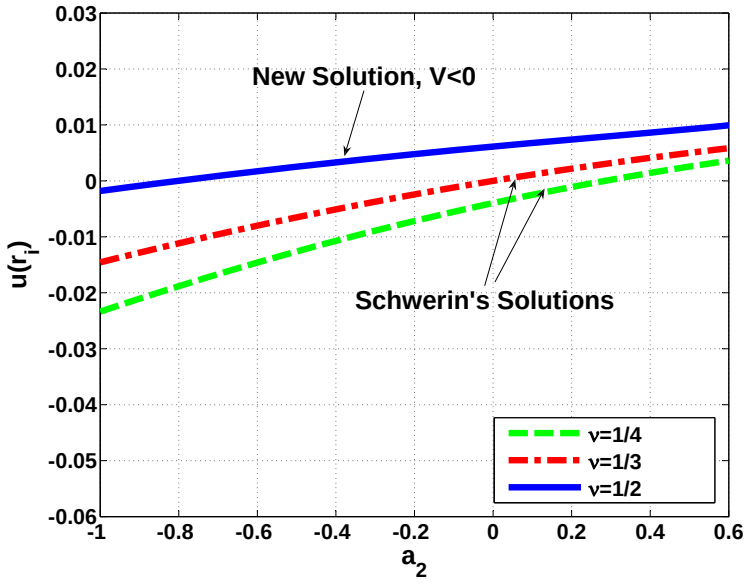

Figure 2.4: Integration constant a_2 versus horizontal displacement at inner boundary $u(r_i)$ with prescribed vertical edge displacement $w(r_i) = 0.1$, $w(r_a) = u(r_a) = 0$

In a wider region of a_2, we note that there is a discontinuity in solutions with

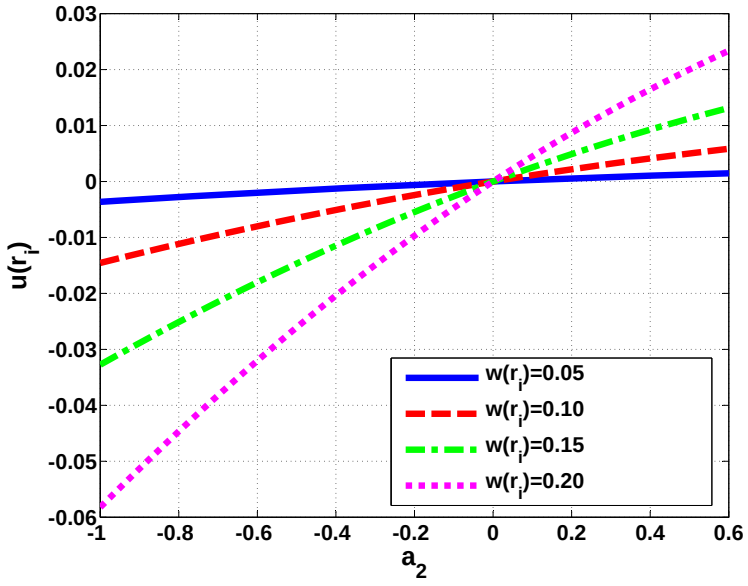

Figure 2.5: Integration constant a_2 versus horizontal displacement at inner boundary $u(r_i)$ for various vertical displacements $w(r_i)$ with Poisson's ratio $\nu = \frac{1}{3}$

$a_2 > 1$ as shown in Fig. 2.6. These solutions involve large slopes $\frac{\mathrm{d}w}{\mathrm{d}r}$, and are thus beyond the scope of the Föppl theory, which assumes that strains and rotations (slope) are small. Also as seen from Fig. 2.6, multiple solutions exist. In addition to the solution with $V < 0$ (tensile radial stress), two solutions can be found for a single value of a_2. Two particular solutions for $V > 0$, which corresponds to compressive radial stresses, are labeled A and B in Fig. 2.6. These negative radial stress solutions are often discussed in the membrane instability analysis, for example wrinkling studies [61]. Point A corresponds to solutions from equations 2.45 and 2.51 using the negative of the $\mp$ option, hence the "top" label in the figure. Point B corresponds to solutions using the positive option. The solutions for vertical displacement versus radial position are shown in Fig. 2.7. Note that positive radial displacements are found at $r = r_i = 0.5$. In these two cases, the positive radial displacement combined with the positive vertical displacement results in compressive values of radial stress.

The resulting radial and circumferential stresses are shown in Fig. 2.8.

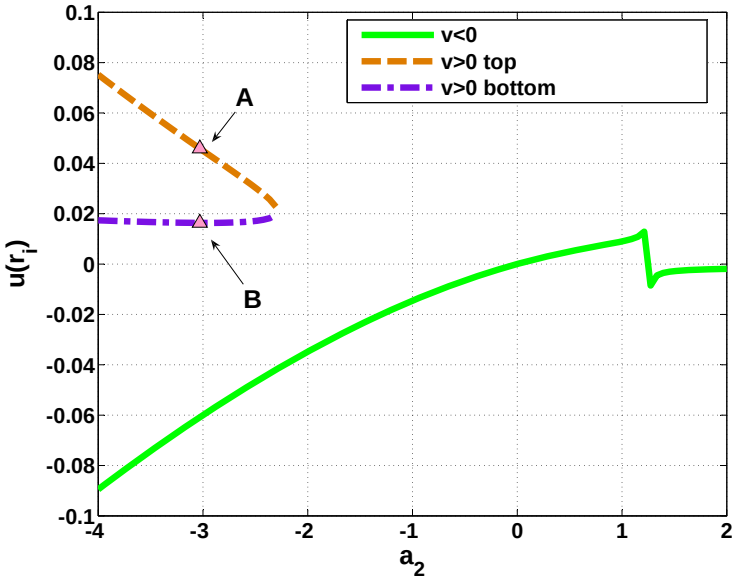

Figure 2.6: Integration constant a_2 versus horizontal displacement at inner boundary $u(r_i)$, with vertical displacement $w(r_i) = 0.1$, poisson's ratio $\nu = \frac{1}{3}$ and $\frac{r_i}{r_a} = 0.5$

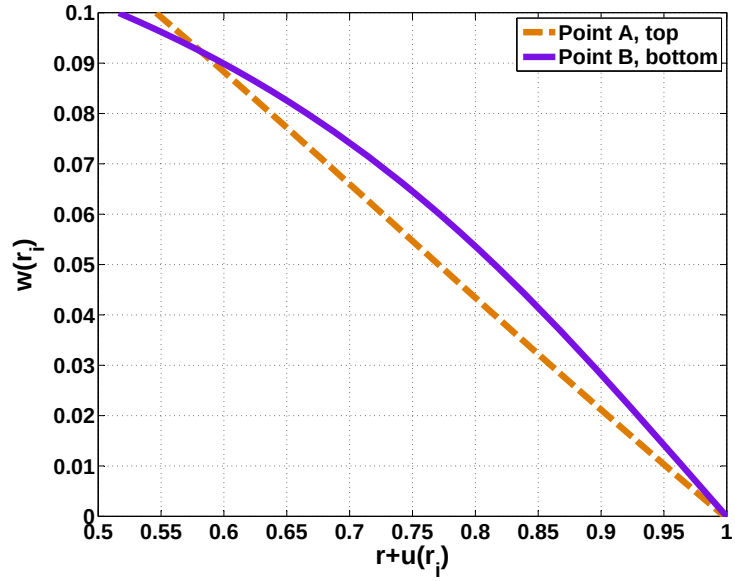

Figure 2.7: Vertical displacements $w(r)$ of points A and B of Figure 2.6 versus radial position $r + u(r_i)$

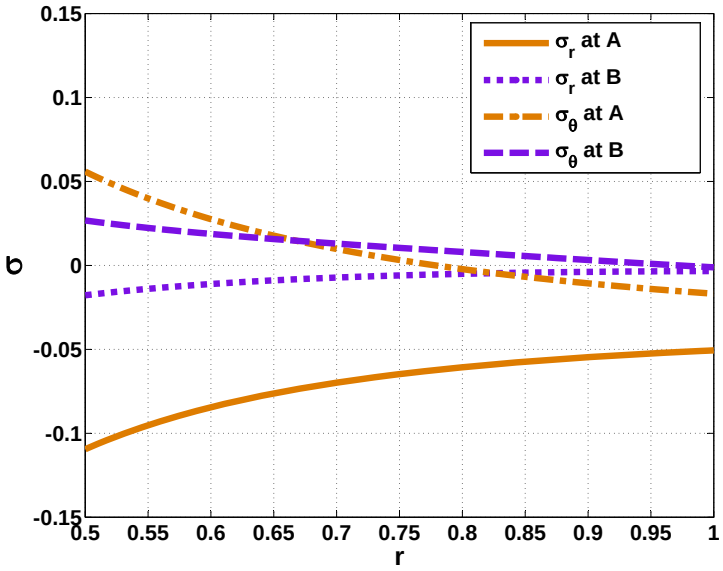

Figure 2.8: Nondimensional radial and circumferential stresses of points A and B of Fig. 2.6 versus radial position r

2.2.2 Comparison

Comparisons of our results are made to previous results of other researchers. As shown in Table 2.1, nondimensionalized radial and circumferential stresses and vertical displacement agree very well with Schwerin's [96] results for $u(r_i) = u(r_a) = 0$, $w(r_a) = 0$ and $P = 12.57$. We use the same nondimensionalized method that Schwerin used: $\overline{\sigma_r} = \frac{\sigma_r}{E} \cdot \sqrt[3]{\frac{32\pi^2 E^2 h^2 r_a^2}{P^2}}$, $\overline{\sigma_\theta} = \frac{\sigma_\theta}{E} \cdot \sqrt[3]{\frac{32\pi^2 E^2 h^2 r_a^2}{P^2}}$, and $\overline{w} = \frac{w}{r_a} \cdot \sqrt[3]{\frac{2\pi r_a h E}{P}}$.

Also, Tuan's [112] results of radial and circumferential stresses at the outer boundary are compared in Table 2.2. Table 2.3 shows the membrane geometry and material properties. Differences of only 1.37% and 1.70% in radial and circumferential stresses, respectively, are found between the present results and Tuan's. This is presumably due to the differences in calculation accuracy between the analytical and numerical methods.

For Tuan's problem, finite element analysis is further conducted by using the

Table 2.1: Comparison of results with Schwerin's

	$\xi = (\frac{r_i}{r_a})^2$	0.25	0.284	0.362	0.557	0.6755	0.8095	1.000
$\overline{\sigma_r}$	Results	2.630	2.515	2.311	1.989	1.860	1.747	1.622
	Schwerin's	2.630	2.510	2.310	1.990	1.860	1.750	1.620
$\overline{\sigma_\theta}$	Results	0.789	0.759	0.702	0.606	0.565	0.528	0.487
	Schwerin's	0.790	0.760	0.700	0.610	0.565	0.530	0.490
$\overline{w}$	Results	0.678	0.628	0.527	0.326	0.226	0.126	0.000
	Schwerin's	0.680	0.630	0.530	0.330	0.225	0.125	0.000

Table 2.2: Comparison of results with Tuan's

	σ_r at $r = r_a$[MPa]	σ_θ at $r = r_a$[MPa]
Results	15.80	5.21
Tuan's	16.02	5.30

Table 2.3: Membrane geometry and material properties in Tuan's study

Name	Data
Membrane material	304 stainless steel
Membrane outer radius, $r_a[m]$	1.857
Membrane inner radius, $r_i[m]$	0.9053
Membrane thickness, $t[mm]$	0.051
Young's modulus, $E[GPa]$	208
Poisson's ratio, ν	0.33

commercial software [3], ABAQUS. Quadratic shell elements with six degrees of freedom at each node are used to capture the membrane deformation. The vertical displacement w, radial displacement u and the membrane Von Mises stress $\sigma_{VonMises}$ in the finite element analysis are compared to the corresponding analytical solutions, as shown in Fig. 2.9(a), (b) and (c), respectively. The Von Mises stress for this $2D$ membrane problems is

$$\sigma_{VonMises} = \sqrt{\sigma_r^2 + \sigma_\theta^2 - \sigma_r \sigma_\theta} \tag{2.59}$$

Excellent agreements are shown in both displacements and Von Mises stress comparisons.

2.2.3 Frictionless Case

We examine the frictionless indentation of a circular membrane. A rigid circular indenter of radius r_i is presumed to have no frictional stress between it and that portion of the membrane in contact with the indenter. The flat membrane in contact with the indenter is thus subjected to in-plane stresses and for a given indentation state a point at the indentor edge, denoted $r = r_c$, is defined by $u(r_c) + r_c = r_i$.

For a given r_c and r_i, the radial stress in the contact portion of the radial membrane is determined. This stress is then matched with the stresses on the inner portion of the unloaded annular membrane. Varying the transition point (r_c) enables us to determine the resulting vertical force to provide the results shown in Fig. 2.10. As a comparison of Fig. 2.10 and Fig. 2.2 shows, smaller pressure is needed for the same displacement in the frictionless case, as expected.

2.3 Conclusion

The nonlinear axisymmetric elastic annular membrane problem is solved for prescribed edge loading. Vertical and horizontal displacements and radial and circumferential stresses of the membrane are determined. Axisymmetric closed-form solutions

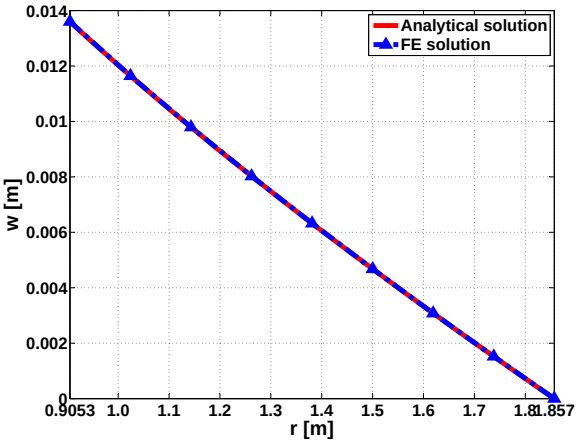

(a) Vertical displacement

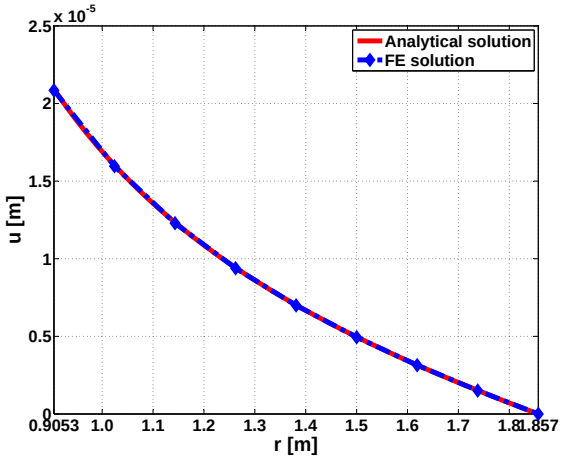

(b) Radial displacement

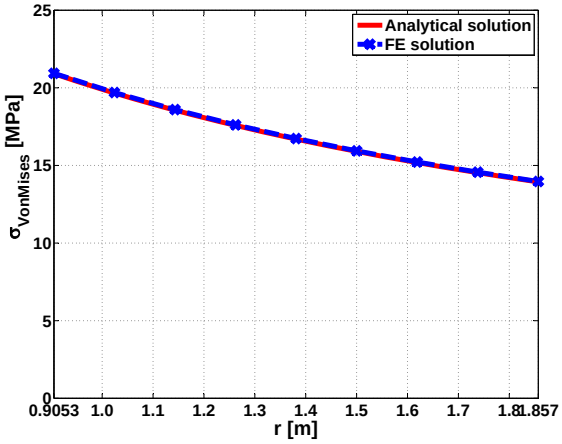

(c) Von Mises stress

Figure 2.9: Comparisons between the analytical solution and the finite element solution

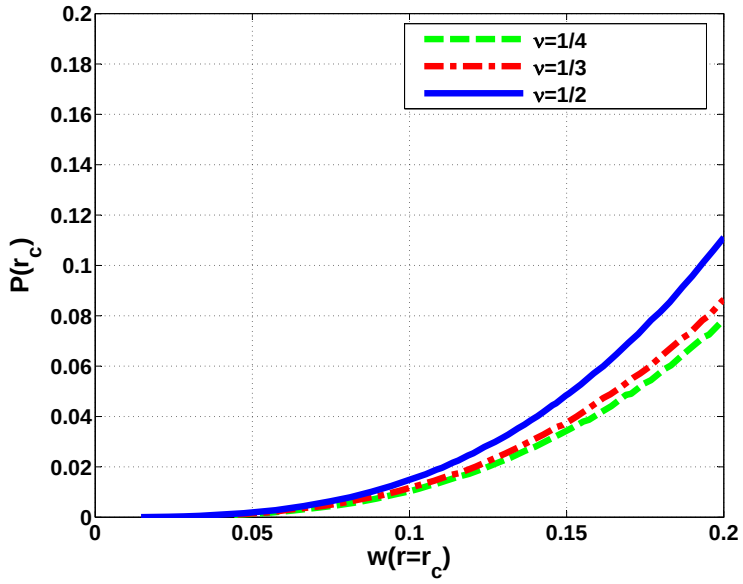

Figure 2.10: Vertical force P, applied with frictionless indenter at the inner boundary, versus vertical displacement at inner loaded boundary $w(r_c)$ for different Poisson's ratios with $u(r_c) + r_c = r_i$

for membrane displacements are derived for all possible Poisson's ratios, especially for Poisson's ration larger than a third, which is not found from previous literatures. Analytical solutions are provided with particular emphasis on solutions for various values of the constant a_2. Solutions show that a_2 is an important constant related to the membrane radial strain. Bifurcation of solutions occurs for some cases in which $a_2 < 0$. Also, the small slope assumption of the Föppl theory corresponds to a certain range of the constant a_2. Under certain boundary conditions ($u(r_i) = u(r_a) = w(r_a) = 0$), for Poisson's ratio equal to $\frac{1}{3}$, zero membrane radial displacement is found. Under these boundary conditions, positive a_2 corresponds to positive radial displacement and negative a_2 to negative radial displacement.

Both friction and frictionless indentor conditions are studied. By applying various vertical displacements at the inner radius, the center load needed is calculated for both cases for materials with different Poisson's ratio. As expected, in the frictionless

case, the center load needed is smaller than that in the friction case.

Furthermore, the comparisons are made to Schwerin's [96] studies and Tuan's [112] ponding problem, respectively. Finite element analysis is employed to simulate Tuan's ponding problem for a comparison of membrane displacements and Von Mises stress. Excellent agreements are achieved for these comparisons, which again validates the accuracy of the derived analytical solutions.

Based on the available closed-form solutions, membrane instability analysis is able to be conducted. For a negative a_2, two membrane deformation statuses are found, both resulting in compressive radial stress. From Fig. 2.7, the membrane deformation is different between the two. Detailed studied are suggested to seek the reasons for the existence of both statuses corresponding to the same a_2.

CHAPTER 3

Pit Corrosion Effects on Ductile Fracture Initiation

Corrosion is a degradation of materials that results from interactions with their environments [102]. Metal corrosion is an electrochemical process that is inevitable in a marine environment unless the metal is well protected by methods like coating or sacrificial anodes. Coating involves paint or some other non-conducting coating on the metal surface to prevent the electrolytes from reaching the metal surface. Using a sacrificial anode commonly involves attaching a metal more anodic than the metal to be protected, forcing the structural metal to be cathodic and thus to be spared from corrosion [102]. These methods are both common and generally effective. However, in complex environmental conditions, for example when offshore structures are subjected to waves, currents, tides, storms, winds or even ice, the above methods may not be effective. Under these conditions, the time duration of these forms of corrosion protection is quite limited. Understanding corrosion effects on structural failure is important to enable the application of loading controls and the prediction of failure when traditional corrosion protections are ineffective.

Classified according to different initiation mechanisms, corrosion in metals takes various forms: "uniform, pit, crevice, impact, cavity bubble and galvanic couple corrosion" [114]. The most common are uniform and pit corrosion. Uniform corrosion

is caused by "complete metal surface exposure in corrosive media, and occurs at about the same rate" [114] in all parts. Pit corrosion, on the other hand, is a highly localized phenomenon. It occurs when the local breakdown starts on thin (nanometer scale) oxide layers on the metal surfaces. Once the passive layers are impacted by the attack initiated on an open surface [100], oxide layers form on the metal surface, which reduces the rate of corrosion of the metal. When those layers are broken, the resulting accelerated dissolution of the underlying metal form the pit corrosion surface.

When uniform corrosion occurs, the structural strength calculation can be estimated relatively easily by reducing the plate thickness or weight loss per unit area from the original values. Several empirical formulae are available to obtain the ultimate strength of plates under general corrosion (see for example [29, 84] and references contained therein). However, the decrease in strength resulting from localized defects, such as pit corrosion, is more complicated than that which results from general corrosion, and relatively less research has been published on this topic.

Nakai and Yamamoto analyzed the effect of pit corrosion occurring to hold frames of bulk carriers on tensile strength [75], collapse strength [72], lateral-distortional buckling strength [71, 72], local buckling [71, 72], shear strength of web plates [74] and web crippling [73]. In Nakai and Yamamoto's framework, numerical simulation (finite element analyses) and experimental tests were conducted simultaneously. The finite element analysis results were validated by experimental test results. They conducted extensive experimental tests of pitted specimens taken from real ships and produced by drilling artificial holes based on real pit corrosion dimensions. They found that "specimens with regularly located artificial pits could simulate the actual corroded plate deformation where the pit diameter varies and the pits are randomly

distributed" [75]. Nakai and Yamamoto tested corroded plates of different pit diameters and distributions. They pointed out that "overall tensile strength decreases gradually while total elongation decreases drastically with increase in pit depth" [75]; and "tensile strengths of specimens with pit corrosion" [75] were reduced more than those specimens subjected to average thickness reduction (uniform corrosion).

Similar conclusions were drawn by Sumi [107]. He used a CAD-CAM machining system to replicate plates with pit corrosion. Specimens were pulled to fracture. He found out that "considerably larger" elongation reduction occurs than that of tensile strength for the pitted specimens. He also investigated the elongation reduction dependency on plate width to thickness ratio. As he suggested, wider specimens are used for further research to minimize the width ratio. Results shown by all these researchers imply that pitted plates fail because of strain localization which is enhanced by the presence of the pitted areas.

Paik et al. [82, 83] performed a series of experimental and numerical studies on a pit-corroded steel plates under both axial compression and edge shear loads. They found that "the ultimate strength under shear is governed by the degree of average pit corrosion intensity" [83], which is defined as the ratio of pitted surface area to the total surface area in [75]. The ultimate strength under compression, on the other hand, is "governed by the smallest cross sectional area" [82] of the plate, where pit corrosion is. They introduced a simplified formula for ultimate strength reduction factor with various pit corrosion intensities, by employing the minimum cross sectional area. Furthermore, they successfully established the relationship between ultimate shear strength and average thickness loss by converting pit depth into uniform corrosion depth for engineering applications. However, they did not consider the effects of different pit locations and pit dimensions.

Dunbar et al. [30] applied the finite element method to study the effect of local corrosion applied to stiffened panels which are typically found in ship structures. The analyses focused on local corrosion loss and corrosion location affecting the structure stability. They found that lower corrosion loss has little effect on the ultimate collapse load of stiffened plates (plates with attached stiffeners to enhance the strength), while higher levels of loss caused local buckling. For the same volume of material loss, the global collapse and the ultimate strengths were influenced by different corrosion locations. As the corrosion location became closer to the center of the panel span, those strengths decreased. Their analysis results also showed that initial residual stress in a corroded area affected the local buckling and plate post-ultimate response.

Amlashi and Moan [6] presented an overview of recent studies and existing guidelines for strength assessment of pit-corroded stiffened plates. They conducted a series of finite element analyses with different degrees of pit corrosion intensity, different pit depths and different locations of the densest pitted zone for the study of the strength reduction of pitted stiffened plates under biaxial compression loading. They found that the ultimate strength of pitted stiffened plates is "governed not only by the degree of pit corrosion intensity but also by the smallest cross sectional area and the location of the densest pitted zone" [6].

OK et al. [81] performed over 200 finite element analyses of unstiffened plates under uniaxial in-plane compression with different locations and sizes of pit corrosion. They showed the pit corrosion length, breadth, depth and its transverse location, especially width and depth, degrade the ultimate strength level. The strength is weakened the most when "corrosion spreading transversely on both parallel edges" [81] as pointed by OK et al. In addition, they used the artificial neural network method to

derive a formula to predict ultimate strength reduction resulting from pit corrosion.

All the above studies provide valuable analysis methods and present useful insights regarding overall strength reduction prediction for corroded plates. Some of them have practical applications in industry. However, research investigating effects of pit corrosion on structure strength has not moved beyond a focus on showing deteriorative effects to the formulation of the guidelines to quantify the strength reduction due to corrosion pitting. Moreover, the predictions of either maximum load or the ultimate strength were derived simply from the geometry change of corroded plates. Such results and predictions are valuable; but to make them useful for application, work needs to be done on mechanical behavior of corroded plates. Specifically, we need to quantify the relations between local strain or stress threshold and the corresponding global average strain and stress levels. This will enable the control and the prediction of ductile fracture through the knowledge of only the global loading conditions, without local detailed analyses. My work is thus directed towards revealing the pit corrosion effects on global strain and stress change by employing a specific failure criterion that includes local strain and stress information under different loading conditions. Pit dimension, pit intensity and other relevant parameters are also considered for the prediction.

Finite element (FE) analysis is applied to fulfill these objectives. FE analyses are often heavily relied on for modern marine structures' fitness-for-service analyses. FE analysis is also a useful tool in fracture simulation. As Li and Karr [59] stated, it is common practice to "either remove elements or to allow elements separate when a critical stress or strain state is reached". For example, Simonsen and Törnqvist removed elements at the crack tip to simulate fracture propagation which occurs in ship grounding or collision in FE analysis [103].

As indicated by Nakai and Yamamoto, pit-corroded plates are more inclined to fail due to strain localization than stress concentration. One failure criterion in the pit-corroded plate study is critical strain level. The critical strain level is affected by the pit geometry, material properties and loading conditions. As marine structures are often modeled at larger scales than would permit modeling of fine-scale pit geometry, model size effect on the critical strain needs to be developed. Additionally, if failure analyses allows the critical strain level determination at a larger model scale instead of a fine scale of corrosion pits, it will facilitate the future failure decision made in the global sense rather than going into the local pitted area. Therefore, it is important to determine the critical strain to failure relationship between local and global. It is also important to determine the size effect on critical strain to failure. This chapter addresses these two issues by using a simplified localization model (as discussed in Section 3.1), and results are compared to nonlinear finite element analyses (as discussed in Section 3.2). Furthermore, under biaxial loading conditions, by applying different failure criteria, the relationship between local and global stress and strain levels of pit-corroded plates are revealed in Section 3.3. The pit intensity effect on the relationship is also discussed in this Section.

3.1 Imperfect Plates under Uniaxial Tension

A one-dimensional imperfect plate model under uniaxial loading condition is first presented. This is an idealized model developed to reveal fundamental physical and geometrical features of the necking localization [35, 60, 58, 59] and used here to study how strain localization is affected by pit corrosion. When necking occurs, plastic flow dominates in the localized zone resulting in the strain localization. Fracture is thus initiated by these large plastic deformation for pitted plates. Although the imperfect plate model discretizes the strain distribution and cannot reflect the complex geom-

etry of pit corrosion, it does provide the quantitative analytical solutions of overall strain-to-failure. These results are compared to those from a nonlinear finite element analysis, which is introduced in Section 3.2. The ductile fracture initiation modeling is a key issue in applying analytical and numerical analyses and comparing these two methods. As a result, the background of ductile fracture initiation modeling is first introduced.

3.1.1 Ductile Fracture Modeling

Structural steels, like many engineering materials, obey Hooke's law reasonably well up to an elastic limit stress, or yielding stress. Nonlinear portions of the stress-strain curve are attributed to plastic flow in the specimen for strains beyond yielding. Also, beyond the yielding state, most steels at room temperature exhibit strain hardening, in which increasing stress is required for increasing strains. At a larger strain level, considerable changes in geometry of the cross section cannot be neglected; this hardening behavior gives rise to the increase of the true stress (force divided by the current cross sectional area) gradually above the nominal stress (force divided by the original area). Eventually the decrease in cross sectional area causes the load to reduce.

The above described ductility can be observed in uniaxial tensile tests, in which necking is triggered. As discovered by Considère [23], necking precedes ductile fracture and eventually leads to ductile fracture. On the other hand, to explain the ductile fracture from the material science point of view at the microscale, McClintock [65] found that "ductile fracture result from the growth of initially existing microvoids and further nucleation and coalescence of the voids and flaws accompanied by plastic flow of the matrix material" [59]. One widely accepted micro model was postulated by Gurson [37]. Gurson developed the yielding criterion for porous

material by using hydrostatic stress. This yielding criterion reveals fundamentals of plastic deformation for compressible porous materials [37].

As a common observation in uniaxial tension, fundamental descriptions of necking have been captured in an idealized three-piece model: homogeneous part-inhomogeneous part-homogeneous part. Ghosh [35] corrected the error in Hart's analysis[41], who first developed this model. Ghosh applied the model to a strain rate sensitivity study. This model was used more recently by Li et al. [60]. They used this model to study the strain localization when necking occurs and predict the strain bifurcation dependency on material imperfections. She also studied the meshing size effect on fracture. This meshing size is on the order of the characteristic size of microvoids (about $1mm$ or smaller). Additional details and summaries of findings can also be found in Li [58] and Li et. al [59, 60].

We apply the three-piece model, building upon the work material above to study the ductile fracture initiation due to pit corrosion. The results are further compared to the finite element analysis of a pitted plate representing, for example, sections of a large ship hull plating. The focus of the comparison is to reveal pit corrosion effects on ductile fracture initiation by establishing "global" and "local" strain relationships under uniaxial tension. These analyses are also summarized in Yu et al. [122]. The focus here is on treating corrosion imperfections as a source of changes in geometry and material properties in the three-piece model's imperfection zone. The three-piece model results for analyzing corrosion defects work well and in much the same fashion as when applied to material defects at smaller scales. Length scales addressed here are thus about one order of magnitude larger than those used previously for microscale material defect analyses. The details of the model are first presented in Section 3.1.2 for completeness in theory introduction as well as for comparison of finite element

analyses results in Section 3.2.

3.1.2 Governing Equations of Static Equilibrium

As shown in Fig. 3.1, the model is discritized by the inhomogeneous part dominant by a center corrosion pit and the outer homogeneous parts. Stress redistribution and shear lag effects are neglected in the idealized one dimensional model. These effects are, however, addressed in the finite element analyses in Section 3.2. Most of the nomenclature used here is that used by Li [58].

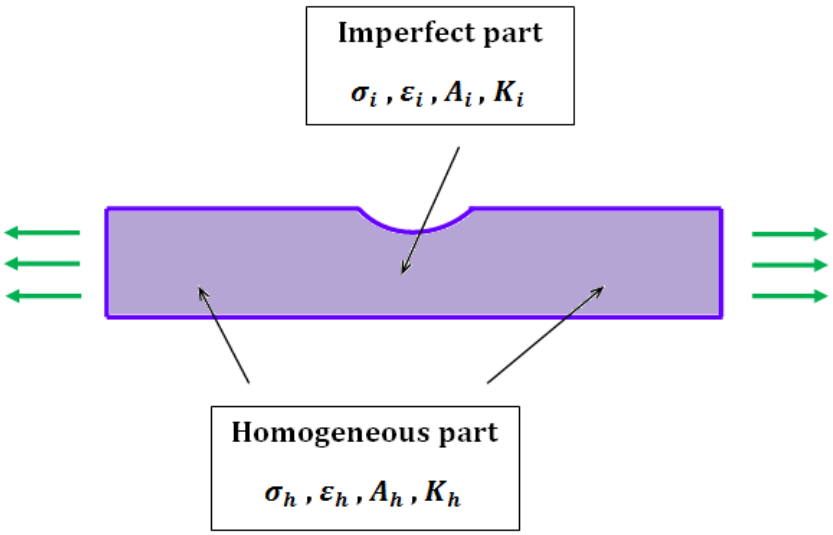

Figure 3.1: Configuration of the three-piece model

The stress-strain relations in the homogeneous and inhomogeneous regions are assumed to follow the power law plastic constitutive law with exponent n.

$$\sigma_h = K_h \varepsilon_h^{\mathrm{n}} \tag{3.1}$$

$$\sigma_i = K_i \varepsilon_i^{\mathrm{n}} \tag{3.2}$$

Here σ_h and σ_i are denoted the true stresses in the homogeneous and inhomogeneous region, respectively, and ε_h and ε_i are the true (logarithmic) strains for the homogeneous and inhomogeneous (pitted) zones, respectively. K_h and K_i are denoted to

quantify the difference of material properties due to the presence of the corrosion. We define a parameter r to represent area reduction and material variation caused by the corrosion pit

$$r = 1 - \frac{A_{i0}}{A_{h0}} \frac{K_i}{K_h} \tag{3.3}$$

In Eq. 3.3, A_{h0} and A_{i0} are the initial cross sectional areas of the homogeneous and inhomogeneous (pitted) zones, respectively. The subscript "0" represents the initial unloaded unstrained state. In a similar fashion, we also denote A_h and A_i as the current cross sectional areas of the homogeneous and inhomogeneous (pitted) zone, respectively.

With the introduction of the logarithmic strain increment $\mathrm{d}\varepsilon$ as the change of an element length, dL, divided by the current length, L [62], we have

$$\mathrm{d}\varepsilon_h = \frac{\mathrm{d}L_h}{L_h} \tag{3.4}$$

$$\mathrm{d}\varepsilon_i = \frac{\mathrm{d}L_i}{L_i} \tag{3.5}$$

The incompressibility requirement yields:

$$A_h \mathrm{d}L_h + L_h \mathrm{d}A_h = 0 \tag{3.6}$$

$$A_i \mathrm{d}L_i + L_i \mathrm{d}A_i = 0 \tag{3.7}$$

From the axial force equilibrium, it is well known that

$$\sigma_h A_h = \sigma_i A_i \tag{3.8}$$

Strains within the homogeneous and inhomogeneous zones are thus able to be related by substituting Eq. 3.1 to 3.7 into Eq. 3.8

$$\varepsilon_h^n e^{-\varepsilon_h} = (1 - r)\varepsilon_i^n e^{-\varepsilon_i} \tag{3.9}$$

This equation is nearly the same as that derived in previous work [58] with the imperfection parameter r being a function of changes in both area and material constants. Li [58] showed that by using the Lamber W function, in the form of $W(z)e^{W}(z) = z$, Eq. 3.9 can be solved. The solution of the strain in the inhomogeneous zone is thus

$$\varepsilon_i = -nW\{-\frac{\varepsilon_h}{n}e^{-\frac{\varepsilon_h}{n}}\frac{1}{(1-r)^{\frac{1}{n}}}\} \tag{3.10}$$

Although, Eq. 3.10 is of the same form as that in Li's work [58], the physical meaning represented by these two equations are different. The imperfection ratio in [58] is based on the assumption that the imperfection due to the existence of microvoids or microflaws does not change the material properties. The imperfection ratio considered here includes the material property variance due to corrosion pitting.

Many similarities regarding the models' response will be shared as discussed in the following. For a special case, when $\varepsilon_i^* = n$, the maximum stress occurs for $r = 0$, as discussed by Malvern [62] and Li [58]. Normalized strain relations are plotted in Fig. 3.2 for different imperfection ratios. For $r = 0$, as the model is stretched, both strains in the homogeneous and inhomogeneous part increase until when the strain in the inhomogeneous part reaches n. Then the strain in the homogeneous part decreases, which is related to unloading. However, the strain in the inhomogeneous part is still increasing, which is corresponding to strain localization in the pitted area. For larger imperfection ratios, the strain in the inhomogeneous part is getting more sensitive to the strain change in the homogeneous part.

If we assume $\varepsilon_i^* = n$ when fracture is first initiated by necking, from Eq. 3.10, the strain to failure in the homogeneous portion using the Lambert W function can be found:

$$\varepsilon_h^* = -nW[-\frac{(1-r)^{\frac{1}{n}}}{e}] \tag{3.11}$$

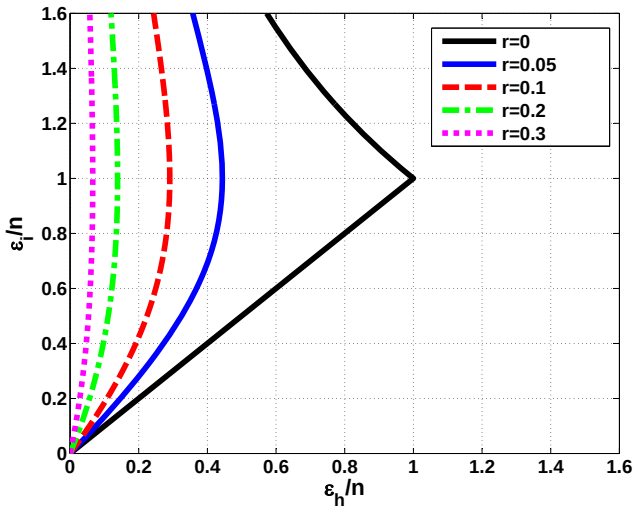

Figure 3.2: Relationship between normalized strains in the homogeneous and inhomogeneous parts of different imperfection ratio r

Equation 3.11 implies that the critical strain to failure (i.e. the onset of fracture initiation) for the homogeneous zone of the material requires only the exponent, n, and the imperfection factor, r. Results for $n = 0.20$ and for $n = 0.12$ for varying imperfection factors, r, are shown in Figure 3.3. When effects of area reduction and material variation due to pit corrosion is getting larger (larger values of r), the critical fracture strain in the homogeneous zone is much lower than that in the inhomogeneous zone ($\varepsilon_i^* = n$).

3.1.3 Strain to Failure: Three-Piece Model

By obtaining the relationship between ε_h and ε_i, Li [58] further developed the overall strain ε of the model by introducing a length parameter $x = \frac{L_{i0}}{L_0}$. x represents "the length ratio of the inhomogeneous part to the original total model" [58].

$$e^{\varepsilon} = (1 - x)e^{\varepsilon_h} + xe^{\varepsilon_i} \tag{3.12}$$

where ε_h and ε_i represent strains affected by pit corrosion.

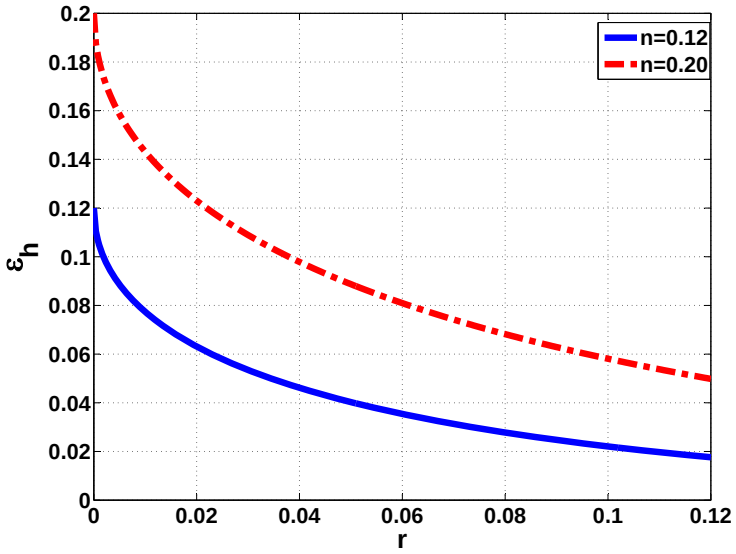

Figure 3.3: Effects of imperfection ratio, r, on the fracture strains, ε_h^*, for power law plastic material with $n = 0.12$ and $n = 0.20$

Based on Eq. 3.12, Li [58] further derived the effective strain to failure in the form

$$\varepsilon_f = ln(Ax + B) \tag{3.13}$$

where

$$A = (e^{\varepsilon_i{}^*} - e^{\varepsilon_h{}^*}) \tag{3.14}$$

$$B = e^{\varepsilon_h{}^*} \tag{3.15}$$

Because they are based on pure geometrical relations, Equations 3.12 and 3.13 are valid for any three-piece model with two distinct strain levels; they are independent of the constitutive equations of the material.

We now take a Taylor series expansion of Eq. 3.13,

$$\varepsilon_f = A_1 + B_1 x + C_1 x^2 \tag{3.16}$$

By expansion about $x = 1$,

$$A_1 = ln(A + B) - \frac{A}{A + B} - \frac{A^2}{2(A + B)^2} \tag{3.17}$$

$$B_1 = \frac{A}{A+B} + \frac{A^2}{(A+B)^2} \tag{3.18}$$

$$C_1 = -\frac{A^2}{2(A+B)^2} \tag{3.19}$$

For the particular case with $n = 0.2$, $r = 0.015$, the failure strain in the inhomogeneous zone is assumed to be $\varepsilon_i^* = 0.25$. This value is used for the comparison to the finite element analysis results later on. By applying Eq. 3.10, $\varepsilon_h^* = 0.123$. The polynomial expansion, Eq. 3.16, takes the form

$$\varepsilon_f = 0.123 + 0.134x - 0.007x^2 \tag{3.20}$$

Neglecting higher order terms,

$$\varepsilon_f = 0.123 + 0.134x \tag{3.21}$$

The first term of the equation approximates, to third digit accuracy, the limiting value ε_h^*, which is obtained for $x = 0$, i.e. $\frac{L_0}{L_{i0}} = \infty$.

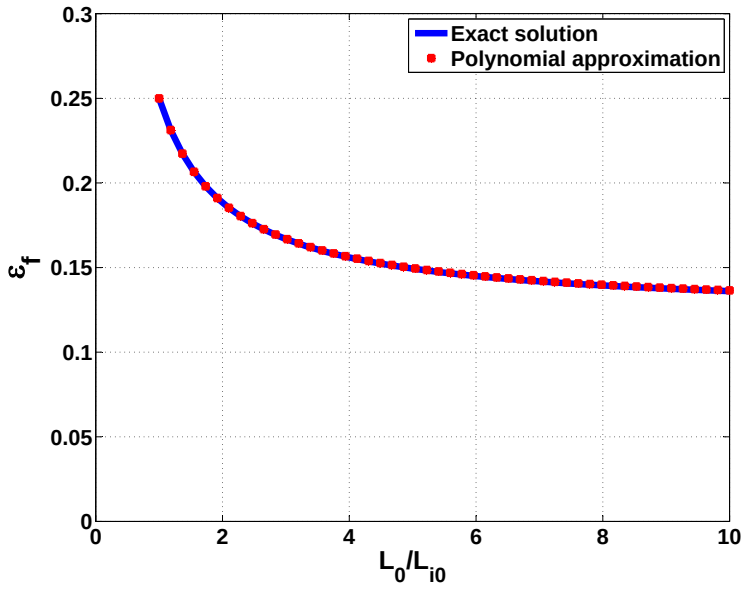

Figure 3.4: Effects of imperfection size on the fracture strains for $n = 0.20$, $r = 0.015$ and $\varepsilon_i^* = 0.25$ representative of A36 steel Taylor series expansion about $x = 1$

Figure 3.4 shows the exact solution and polynomial approximation for the element size (i.e. the element size on the order of the model size) effect on the strain to failure for this case by using Eq. 3.13 and 3.20. The exact and approximate solutions to Eq. 3.12 are indistinguishable at the scale of the figure. For larger ratios of overall length to imperfection length, the overall average strain to failure occurs at ε_h^* as mentioned above. The solution approaches the value of ε_i^* at $x = 1$.

3.1.4 Summary of One-dimensional Model

An important issue arising from the use of the $1D$ idealized model has traditionally been the establishment of L_{i0}. This length, in theory the length of the inhomogeneous zone, is also associated with the length of the necking area. In fact, there is no generally accepted means for determining L_{i0}, unless there is an obvious dominant area of cross section reduction in a sample. This uncertainty is due to, at least in part, the fact that the inhomogeneous zone length cannot be considered independently from L_0, the length scale of the elements in consideration. For example, fracture analyses in microscale are concerned with the growth of pores and voids. The necking of material between microvoids must be considered. Thus at the microscale, impurities and even granular structure of the material must be accounted for. This level of detail, with very high levels of strain to failure, is of course impractical for many engineering applications for marine structure analysis.

Often, however, engineering analyses of, say, ship plate, or ship structural components are concerned with the initiation of fracture employing plane stress elements of sizes on the order of over 10 to 100 or $200mm$ or more. The strain-to-failure condition is very sensitive to the model length. The length dependency can be analyzed by fixing the inhomogeneous zone length while changing the overall element size similar to Li's size effect study in smaller scale [58]. In the present study, we associate L_{i0}

with the diameter of the corrosion pit because the dominant pit feature significantly influences the local stress and strain distributions. Considerable discussion of these issues at various scales can also be found in Ghosh [35], Kanvinde and Deierlein [48], Li [58] and Li and Karr [59].

We address the length dependency of strain to failure using finite element analyses of a corrosion pitted plate in further detail, and compare results with the idealized $1D$ model, in the following section.

3.2 Finite Element Analyses of an Idealized Pit Corroded Model

Many problems of structures and materials can be studied by finite element analysis. Here, we first assume that pitted area is smaller than the FE model size. The benefit of the study in this section is to allow the analysis in the model size level; rather than going into the finer scale.

At the element scale, imperfections such as corrosion pits may eventually dominate. In this section, the way in which the size of the imperfection and the mesh size influence the fracture strain is studied by a methodology similar to analyses of the previous section. The approach is however somewhat different: we model the geometry of a plate with a representative central corrosion pit. Fracture is initiated when a critical effective strain is first reached at the center of the pit. We study the effects of varying the overall size of the finite element model while keeping the geometry of the corrosion pit unchanged. The average, overall strain is shown to depend on the overall length, behavior much like that described in Section 3.1. The idea is to thereby establish mesh size effects for strain failure for elements on the order of the overall model length defined here. In this fashion, one can avoid the necessity of including local pit geometry in the structural analyses at the larger scale (i.e. with elements on the order of, say, $100mm$ or more).

3.2.1 Modeling

The ABAQUS [3] computer package is applied to simulate the response of a corroded plate. The initial length L_0 of the model varies from $50mm$ to $350mm$; width is W_0, $50mm$, and the thickness t_0, $20mm$. A single pit is centered in the plate. Its shape is a semi-oblate spheroid, with the initial diameter D_0 of pit area $20mm$, depth h_0 $3mm$. The reason for selecting this initial diameter and depth stems from some representative field measurements of ship plate corrosion pits [75]. Because of the symmetry in both length and width directions, only a quarter of the structure is modeled in ABAQUS, see Fig. 3.5. Therefore, the quarter model length L_m varies from $25mm$ to $175mm$. The model material is $A36$ steel. The power law definition $\sigma = K\varepsilon^n$ is applied for plastic deformation constitutive relations, with $n = 0.2$ and $K = 870MPa$. The yielding stress is $\sigma_Y = 250MPa$; the Young's modulus is $E = 200GPa$ and the Poisson's ratio is $\nu = 0.33$. The element size of $0.25mm$ is applied in the center of the pitted area after performing meshing sensitivity study. Figure 3.5 also shows the typical meshing geometry of the model.

Symmetry boundary conditions are defined at two surfaces as shown in Fig. 3.5(b). To prevent the rigid body motion along the thickness direction, a constraint is applied at the bottom edge, which is also shown in Fig. 3.5(b). A linear varying (with time) displacement is applied on the free surface to stretch the plate, with a peak end displacement for the quarter-model of $25mm$. Figure 3.6 show the Von Mises stress and effective plastic strain distribution over the plate at different time steps. The maximum end displacement corresponds to step time equal to 1.00. Over time, necking starts to occur in the region associated with the location of the pit. Localized strain concentration in the pit area increases dramatically compared to the non-pit area. In fact, this behavior is very similar to the deformation characteristics described

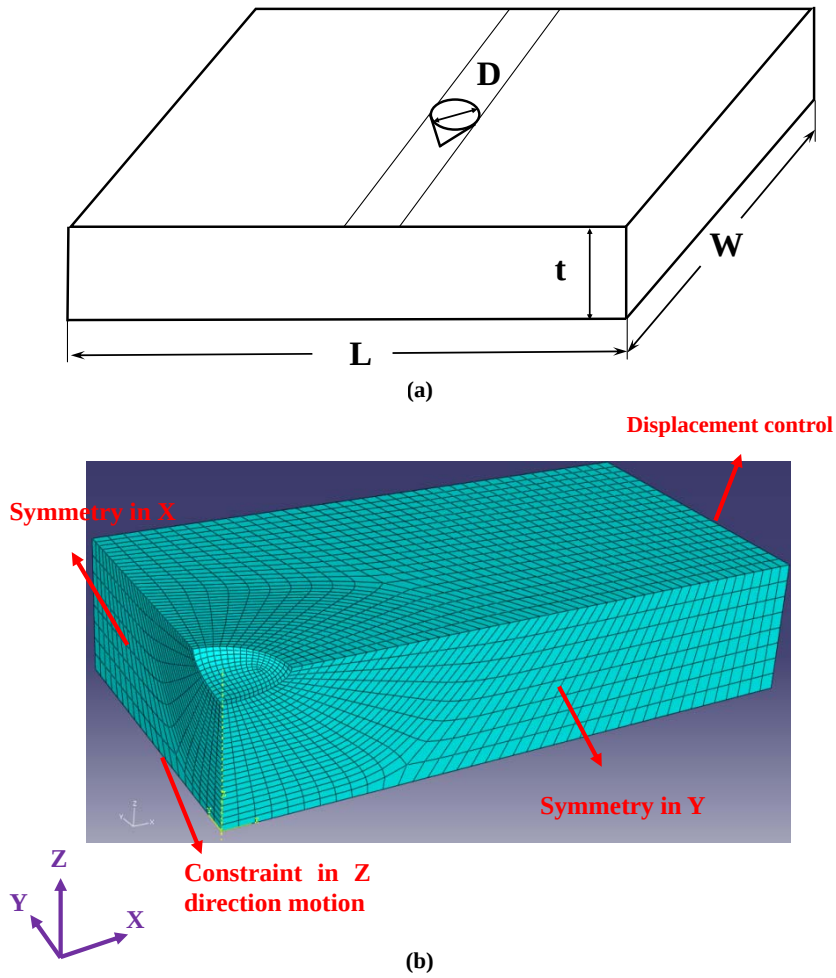

Figure 3.5: Finite element model (ABAQUS, V6.7-1)

by the $1D$ idealized model, which consists of two discrete regimes rather than the highly detailed finite element description.

3.2.2 Results and Discussion

The growth of local effective strain with the increasing of plate overall average effective strain with L_m of $125mm$ is shown in Fig. 3.7. The plate overall average effective plastic strain is approximately defined as the plate length variation over the current plate length. The local effective strain is defined as the plastic effective strain magnitude at the center of the pit. The definition of the plastic effective strain magnitude is shown in Eq. 3.22.

$$\bar{\varepsilon^p} = \int \sqrt{\frac{2}{3} d\varepsilon_{ij}^p d\varepsilon_{ij}^p} \tag{3.22}$$

For overall average effective axial strains less than 0.18, the local effective plastic strain at the pit increases in proportion to increasing average strain. However, beyond a level of 0.18 for the overall average strain, the local effective strain at the pit increases very rapidly with a highly disproportionate increase in local strain relative to the overall average strain. Also shown in the figure are results for a plate without a pit, with the name imperfect model; in this model a very small imperfection ($0.5mm$) in thickness along one transverse edge is defined in the center of the plate to trigger localization in the same area. This imperfect model is shown in Fig. 3.8. Local strain at two points are labelled as top point and bottom point. The local strains (the lower two curves in the Fig. 3.7) show some nonlinear increase, but compared to that in the pit region (the upper curve), these values are much lower. The local strain caused by the presence of the pit is nearly twice that of an uncorroded plate when the far field strain is about 0.22. This demonstrates the fact that the regions of a corrosion pit is much more susceptible to ductile fracture than uncorroded plates.

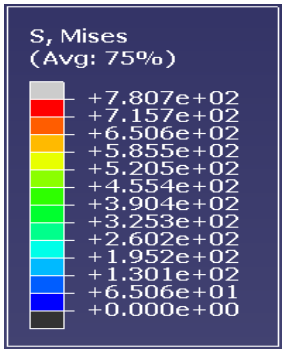

Von Mises Stress

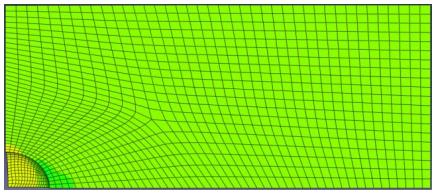

(a) Step time=0.24

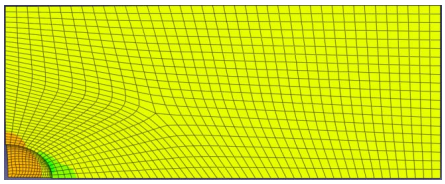

(b) Step time=0.48

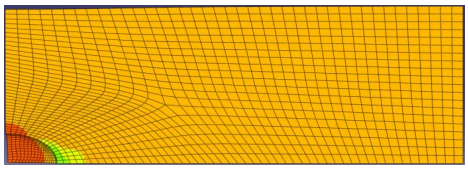

(c) Step time=0.76

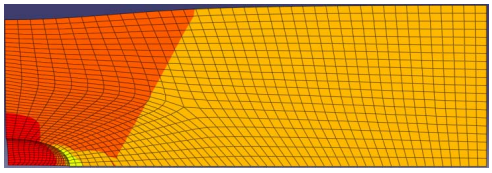

(d) Step time=1.00

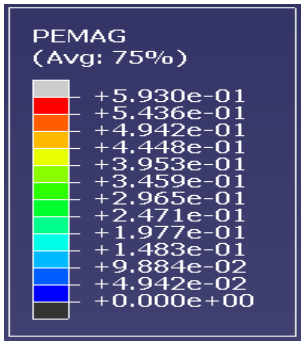

Effective Plastic Strain

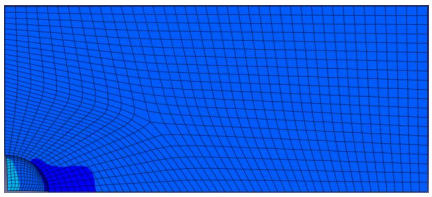

(a) Step time=0.24

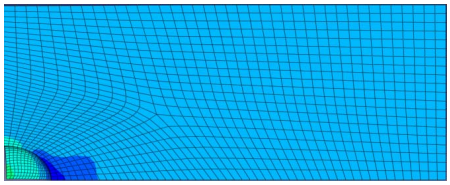

(b) Step time=0.48

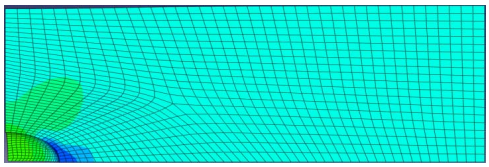

(c) Step time=0.76

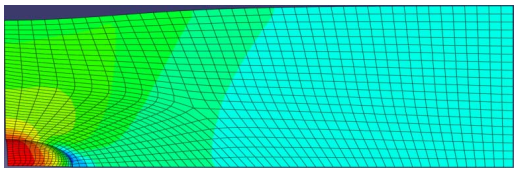

(d) Step time=1.00

Figure 3.6: Von Mises stress ($[MPa]$) and effective plastic strain distribution over the plate surface with length $100mm$ at different time steps

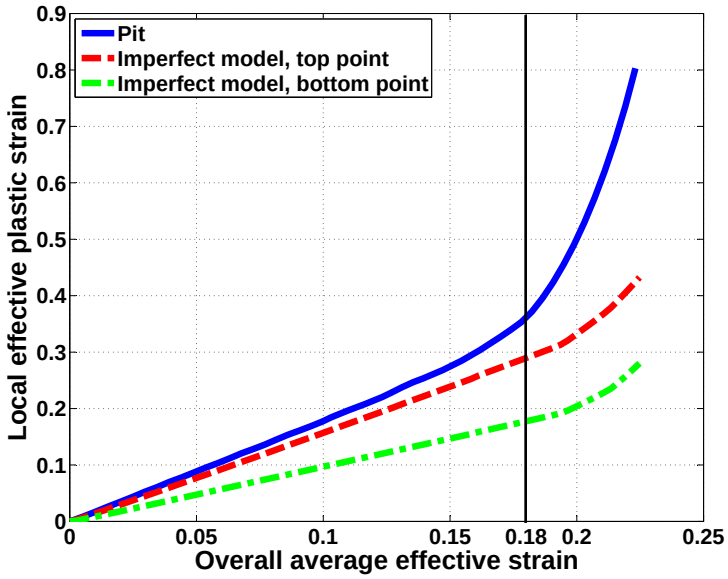

Figure 3.7: Local effective plastic strain versus overall average effective strain for two models, both of length $L_m = 125mm$

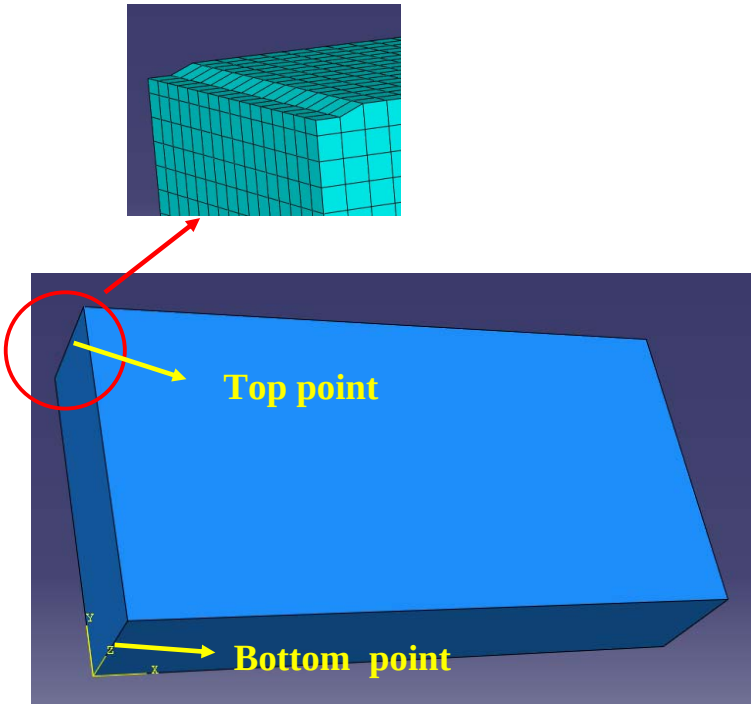

Figure 3.8: Imperfect model for a comparison to pit corroded model; model length $L_m = 125mm$

By collecting simulation results for the corroded models for various lengths, we plot the effective plastic strain at the center of the pit versus the model length as seen in Fig. 3.9. With an increase of model length, especially when it exceeds $100mm$, a nonlinear relation develops between the model length and effective plastic strain in the pitted area. This regime emerges as the strain state approaches that for a model developing a "homogeneous" area akin to ε_h^*, and a second region in the pit area akin to ε_i^* of the $1D$ model.

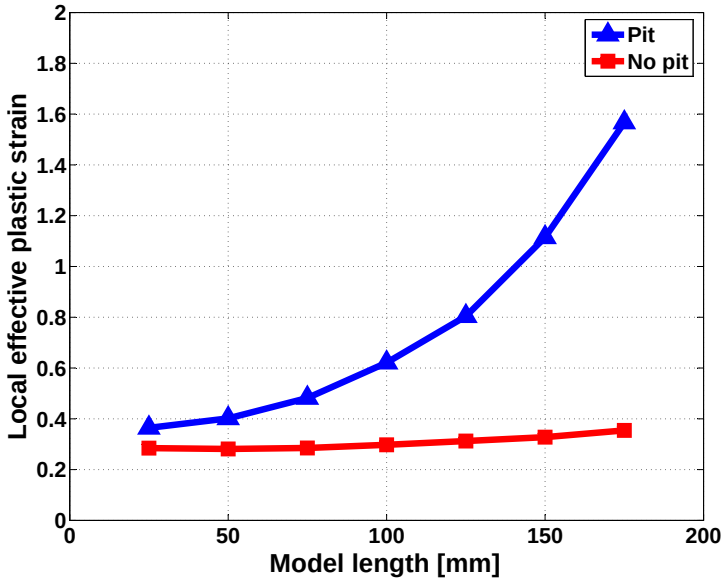

Figure 3.9: Effective plastic strain at the center of pit and at the center of necking area respectively versus model length of plate, when overall average effective strain is 0.22

Also in Fig. 3.9 present the results of the plate with imperfection as shown in Fig. 3.8. The corroded plate results are compared with those of the non-corroded plate under the same applied displacement. The corrosion induces a much higher strain localization than normal plate necking. Thus, corrosion of plates can be seen to cause, in this case, considerably higher local strains in the area of the pit and thus high susceptibility to ductile fracture. This is fully consistent with previous

conclusions [75].

Figure 3.10 shows the overall average effective strain versus model length of the corroded plate, when the localized plastic strain at the center of the pit area reaches 0.25 and 0.30, respectively. Results are compared to the results of the previous section for a critical strain of $\varepsilon_i^* = 0.25$. Note also the similarity in form of Fig. 3.10 and Fig. 3.4, which further confirm the application of $1D$ model to the study of pit-corroded plate. Clearly the $1D$ model offers a meaningful qualitative and quantitative description of the influence of element size on strain to failure predictions. In both instances, when the pit dimension is about the same order of the plate length a higher overall average strain is required to reach a given local strain. This strain approaches the value of the local critical strain when the overall length is the same as the imperfection length (pit diameter). However, in the $3D$ finite element model, the strain variation from pitted area to the far field is continuous. Whereas the, strain distribution is discrete in the three-piece, $1D$ model. Additionally, complex pit geometry is able to be modeled in finite element analysis. So the $3D$ finite element model is more detailed and robust than the $1D$ model.

3.3 Pit-Corroded Plates with Various Pit Intensities under Biaxial Loading

In the previous $1D$ and $3D$ model studies, both models are based on the application of global axial deformation with transverse displacement unconstrained. Another consideration, particularly more important for biaxial loading, would be to refine the strain to failure criteria [13]. This is often considered when stress states vary significantly from the uniaxial state. Additionally, although the idealized center pitted model is able to reveal the fundamental strain localization mechanisms, questions will arise regarding corroded plates of various pit intensities, as previous

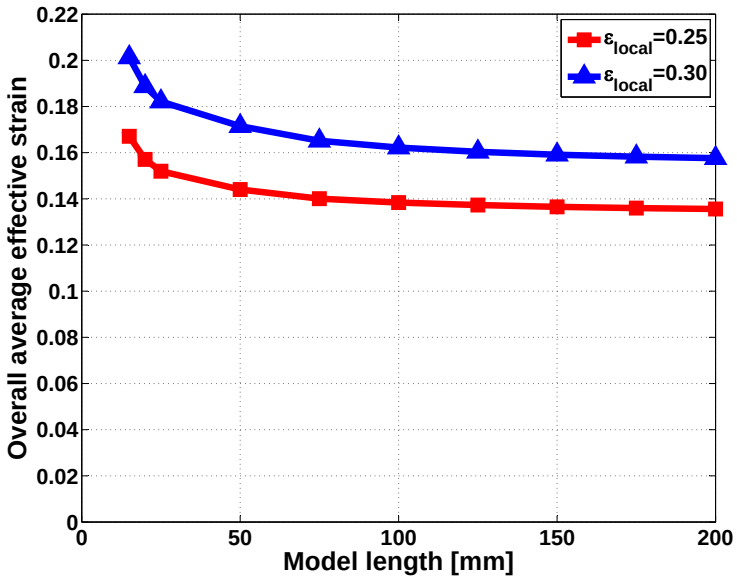

Figure 3.10: Overall average effective strain versus model length, when localized effective plastic strain reached 0.25 and 0.30

research concluded that pit intensity is an important pit geometry parameter affecting corroded plate strength and deformation (the ratio of pitted surface area to the total surface area in [75]). However, pit intensity is still only one way to describe pit distribution. The limitation in pit intensity is that pit depth is not described, which is also an important geometrical parameter. The pit depth effect will be included in the reliability study of pit-corroded plate in Chapter 5.

As a logical and important extension, the modeling approaches in Section 3.2 is extended to pit-corroded plates with various pit intensities and distributions and under more complicated constraint conditions. Furthermore, two failure criteria are applied to reveal the strain level at the far field varied by the corrosion pits.

The ABAQUS [3] package is again applied to simulate the response of corroded plating. The initial length of the model L_0 is $220mm$, width W_0 $100mm$, and thickness t_0 $20mm$. Individual pit geometry and material properties are the same as

described in Section 3.2.1. Four different pit intensities are modeled: 4 pits (two distributions), 12 pits and 21 pits, as shown in Figure 3.11. Numbers in the figure are the pit intensities. The following calculations are limited to the condition that the pit depth is $3mm$ even though pit intensity varies. Pitted areas are intensively meshed, with the minimum element size $1.6mm$ while the average element size is $2.5mm$ in the area away from pits. For loading conditions, instead of applying a load, linearly varying (with time) displacements are applied on two perpendicular free surfaces to stretch or compress the plate, with a peak end displacement for the model of $u = 33mm$ along the transverse direction. Along the plate width, the peak end displacement is $u' = \gamma u$, with $\gamma = 0$, ± 0.25, ± 0.50, ± 0.75, and ± 1.00. The other two free surfaces are subject to simply supported constraints.

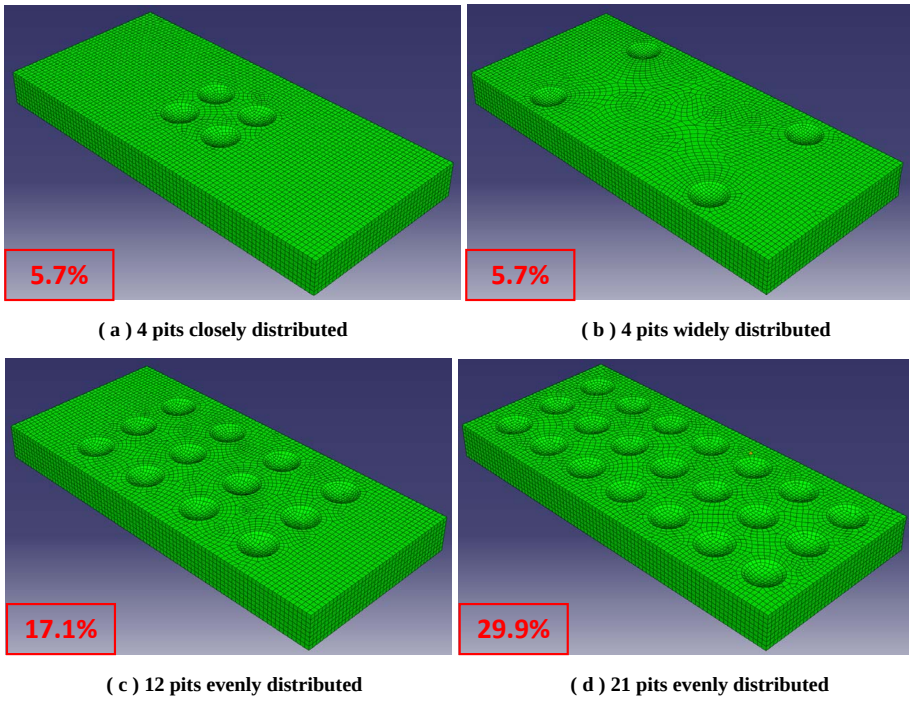

Figure 3.11: Finite element models

The Von Mises stress and effective plastic strain distributions are obtained over the plate at different time steps. The maximum end displacement corresponds to

step time $t = 1.00$. Under biaxial tension, when pits are closely distributed, they effectively behave as one defect, the Von Mises stress and the effective strain distributions show three distinct regions, as presented in Fig. 3.12. In fact this behavior is very similar to the deformation characteristics described by the $1D$ idealized necking model which consisted of three discrete regimes. When pits are widely distributed, pits in the same cross section deforms similar, as distinct regions occur as shown in Fig. 3.13.

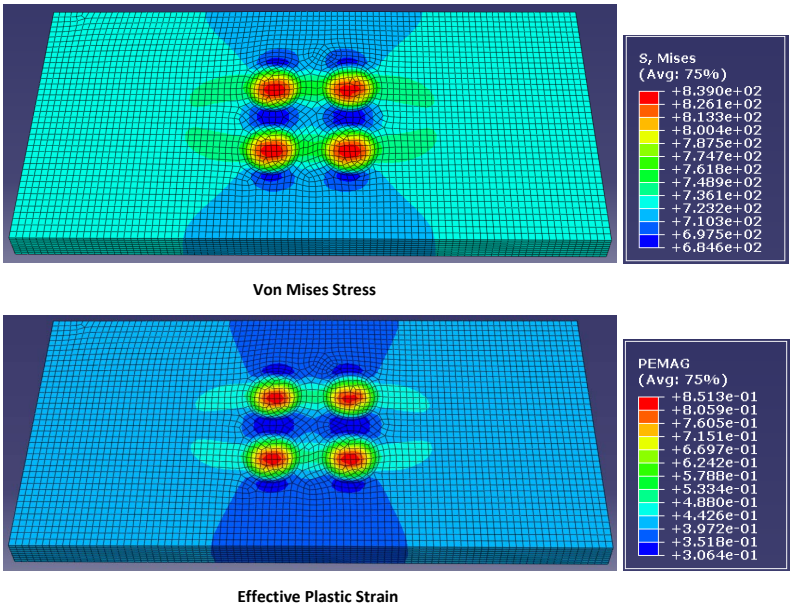

Figure 3.12: Von Mises stress ($[MPa]$) and effective plastic strain distribution in the plate with 4 pits closely distributed, $\gamma = 1.0$

In the tension-compression case, for $\gamma = -1.0$, the pit area sustains high localized strain as shown in Fig. 3.14. For 4 closely distributed pits, pits behave together as one origin of defect. It is more likely that the plate wrinkles at the center as extreme high strain localization arises in this area. However, for widely distributed ones, pits induce high strain localization around the edges of the plate. The plate is more susceptible to wrinkle along transverse edges. This is mainly due to the pit distribution; and the plate edge constraint is another reason. For 12- and 21-

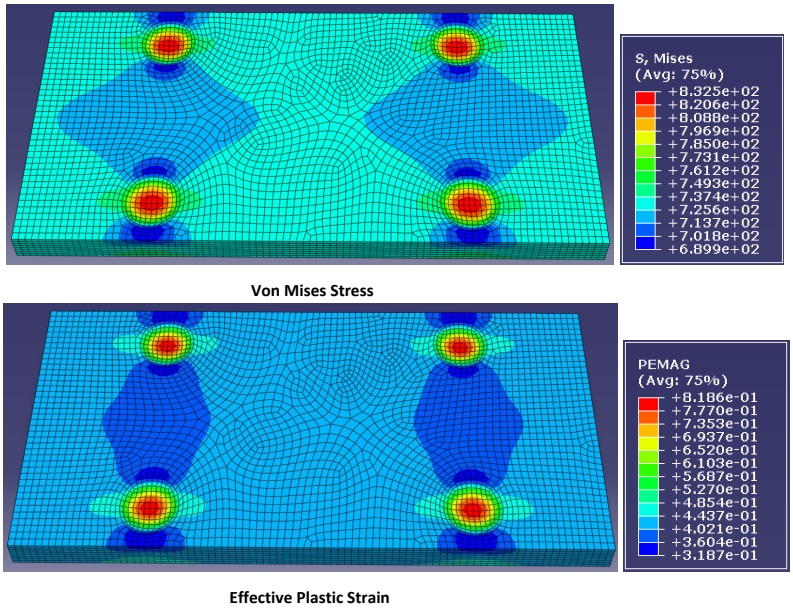

Figure 3.13: Von Mises stress ($[MPa]$) and effective plastic strain distribution in the plate with 4 pits widely distributed, $\gamma = 1.0$

pit plates, relatively lower strains concentrate around center pits compared to that around center pits in the 4 closely-spaced-pit model.

The strain distribution shows a uniform trend for those two models. The strain localization is released as the increasing of pit intensity. Under these tension-compression loading conditions, it is obvious that the strain localization due to pits is very sensitive to pit intensity and pit distribution. In actual ship structures, corrosion pits are distributed randomly, and since the strain localization due to pits is very sensitive to pit distribution and intensity, the random array of pits is recommended for the consideration of these structural deformation analyses.

By collecting stress and strain data from all these finite element analyses, two failure criteria are used to reveal how corrosion pits change the far field plate deformation. Here, the far field quantities is corresponding to those in the homogeneous zone in $1D$ model. As effective plastic strain is uniformly distributed in the area away from corrosion pits, the uniform strain value taken from one representative node in

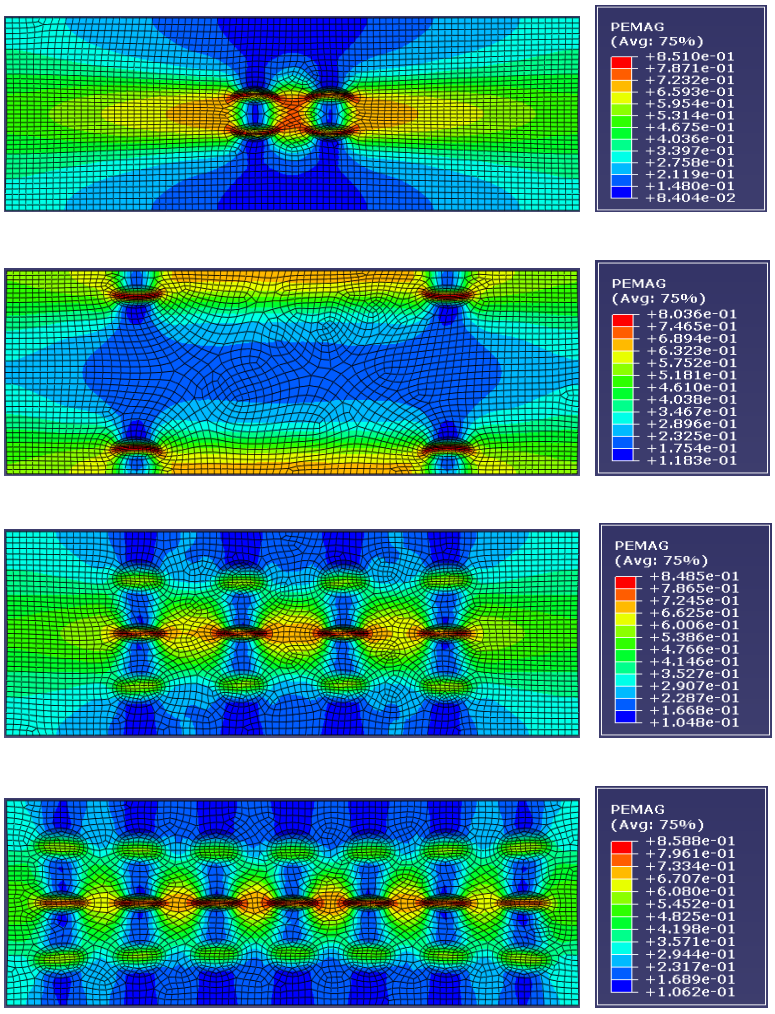

Figure 3.14: Effective plastic strain distribution in plates, $\gamma = -1.0$

this area is regarded as the far field effective plastic strain. The two failure criteria are local effective plastic strain and local maximum shear stress, which are studied and discussed by Wierzbicki et al. [118]. They conducted 15 sets of experiments for a power-law hardening material under plane stress and compared 7 fracture criteria to experimental results. They recommended the maximum shear stress criterion as this criterion closely follows the trend of all tests except the round bar tensile tests, which is also computationally effective.

Regarding the first failure criterion, Fig. 3.15 presents the effective plastic strain at the far field when the local maximum effective plastic strain reaches 0.2. Generally speaking, far field strain values at fracture do not vary greatly among 5 cases. Pit-corroded plates are of lower far field strain levels under tension-tension than under tension-compression. This suggests the future study of pitted plate under biaxial compression. Under biaxial tension, the far field strain is about 0.095 on average, which means that corrosion pits behave as a strain amplifier increasing stain from far field to near field. The far field strain at fracture is not affected by biaxial tension ratio, pit intensity and pit distribution. This conclusion may benefit engineering in the similar study. However, under tension-compression, the far field strain levels at fracture vary mainly with γ.

Regarding to the second failure criterion, Fig. 3.16 presents the effective plastic strain at the far field when the local maximum shear stress reaches $670MPa$. This value is picked to ensure that such amount of maximum shear stress happens in all loading conditions for all models. The far field effective plastic strain is plotted versus different loading conditions as shown in Fig. 3.16. In general, one center pitted plate sustains a lower far field strain level when fracture is initiated locally. Surprisingly, 21-pit plate also yields a lower far field strain level than that of 4- and 12-pit plates.

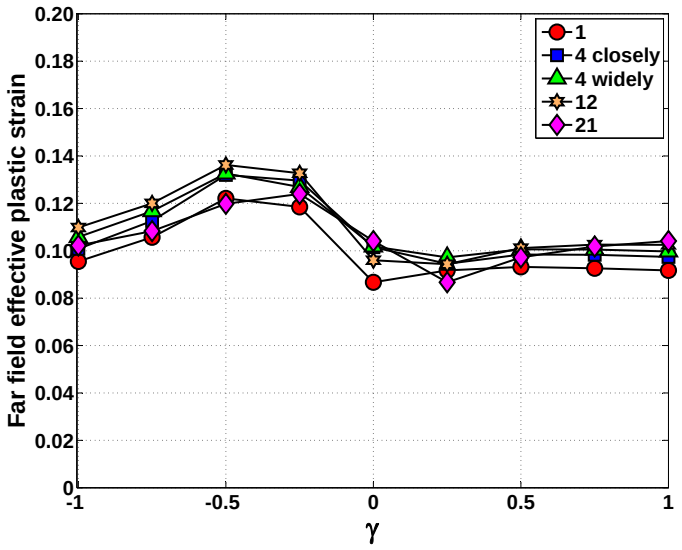

Figure 3.15: Effective plastic strain at far field versus γ when local effective plastic strain reaches 0.2

We postulate that this is because the 21 pitted plate represents a more uniformly corroded plate. With less strain localization of each pit, the total strain level is lowered. This conclusion is consistent to what Nakai and Yamamoto found in the experiments [75]. Comparing the strain level between 1 pit and 4 closely distributed models, the latter induce a higher value of far field effective strain. This means that for the same pit distribution, higher pit intensity induces higher strain localization. Comparing between 4 closely and 4 widely models, the far field strain is lower for the 4 widely distributed pitted plate under tension-compression and higher for it under tension-tension. This shows that the pit distribution is also a factor affecting the plate deformation.

3.4 Conclusion

We have developed a theoretical model for predicting rupture strain for power law plastic material with corrosion pit imperfections: a $3D$ model based on the finite element method. The results are compared to those of a $1D$ model based on a single

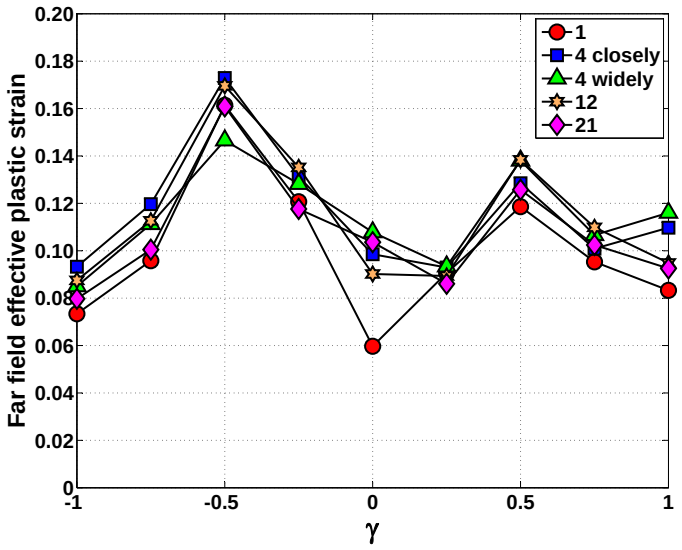

Figure 3.16: Effective plastic strain at far field versus γ when local shear stress reaches $670MPa$

localization zone. Similar trends of the overall average strain dependency on model length confirm the application of $1D$ model on the analysis of pit-corroded plate ductile fracture initiation. The $3D$ model is more capable of accurately capturing effects of general geometric imperfections including arbitrary corrosion pit shapes. Both models provide quantitative relationships for size effects relating overall length to strain-to-failure. This is valuable for the element size decision in the pit-corroded plate modeling. Both models also indicate a strong reduction in fracture elongation in the presence of imperfections caused by corrosion pits.

The pit corroded plate fracture initiation study is also extended to plates under different biaxial loading conditions, with different pit intensities and pit distributions. Under two fracture failure criteria, far field effective plastic strain level is calculated according to various loading conditions.

- Using the local maximum effective strain criterion, the far field fracture strain is not strongly dependent on pit intensity and distribution. Under biaxial tension

conditions, corroded plates are less susceptible to fracture; a constant strain amplification factor is found regardless of loading ratio under biaxial loading conditions.

- Using the local maximum shear stress criterion, higher strain localization is revealed again in the pit corroded plate than in the uniformly corroded plate. Pit distribution is also a factor influencing corroded plate deformation.

- Pit distribution influences plate deformation differently under biaxial tension and under tension-compression for a given failure criterion. Therefore, to confirm this point, plates under other loading conditions, such as biaxial compression or even bending, are suggested for study in the future.

- As the stress distribution at the far field is not uniform, difficulties occur to quantify the far field or global fracture stress levels under displacement control. How pit geometries and loading conditions affect the stress distribution is a recommended topic for future study.

The above studies address important pit corrosion degrading effects on plate deformation under different loading conditions. Due to the definition of pit intensity, the above conclusions are limited to the pit depth of $3mm$. The pit depth effect will be elaborated in the reliability of pit-corroded plate in Chapter 5.

In order to develop a methodology including pit geometry, intensity and loading condition, a detailed database is needed, which may take years and tremendous effort. Experimental tests and finite element methods are powerful tools to assist the study. However, to quantify the time effect in corrosion in either method requires further study.

CHAPTER 4

Bending Capacity of Corroded Pipelines

Oil and gas pipeline/flowline structural integrity assessment under high temperature is of great importance in industry. The integrity analysis can become significantly complex when pipes simultaneously sustain pressure, axial loading and bending, and corrosion. The proximity of an oil field to the sea, for example, may create soil conditions that are conducive to corrosion. Thermal expansion and the resulting bending moments generated form the basis of a limit state that is affected by corrosion. Assessment for pipelines subjected to corrosion has been extensively studied, but studies have been generally focused on the containment capacity limit state. In this chapter, detailed three dimensional finite element analyses are performed for the study of bending capacity of corroded pipelines focused on geometries typical for high pressure ($> 10ksi$). The results are validated by experimental test results to reveal key points in modeling this problem as well as the secondary effects observed in the tests.

Research and analyses on corrosion reported in the literature mainly focus on the burst limit state for pipes. Simplified methods to account for the loss of pressure containment capacity in operation have been developed with success. The ASME/B31G standard [8] is the most widely accepted method for pressure containment assess-

ment. However, it is generally applicable for evaluating corroded pipes under mostly internal pressure. On one hand, since these procedures have been successfully applied in the industry for many years for burst containment, the method has been validated. On the other hand, the application of such existing procedures for the pressure containment limit state to the bending capacity limit state can possibly "give nonconservative results" [94].

To date, few studies have been performed on corroded pipeline bending capacity. Full size experimental work was done by Roy et al. [94], Katsumasa et al. [68] and Shinji et al. [2]. Roy et al. performed both experiments and finite element analyses to investigate failure mechanisms of corroded pipes under combined loading of internal pressure, bending moment and axial force, with the emphasis on pressure. He addressed three primary failure mechanisms: "rupture (pressure containment), bending collapse and axial collapse". Bending collapse (strength) is also regarded as a failure mode in my analyses of corroded pipe under bending moment. Katsumasa et al. [68] and Shinji [2] et al. conducted combined loading and monotonic bending tests, respectively, to determine the pipe structure's collapse moment capacity. Even though they focused on monotonic bending tests, the test pipes had very large D/t (diameter/thickness) ratios. These dimensions ($D/t \approx 100$), although common for gas transformation, are not common for high pressure pipes used in the oil and gas industry ($D/t \approx 20$).

Based on test data and finite element analysis results, some empirical formulas are available to account for moment capacity reduction due to corrosion. A net-section collapse criterion [8, 38] has been employed to analyze the failure of a locally thinned pipe under bending but in some cases it is overly conservative. Zheng et al. [125] modified the criterion by using the corroded thickness rather than the initial

pipe thickness. The modified criterion gave a better prediction than the net-section collapse criterion did for relatively long defects only. Kim et al. [53, 101] proposed the reference stress-based approach to estimate the failure strength of a pipe with local wall thinning. The local failure strength was expressed as a function of global limit loads. Results showed that overall and defect geometries as well as material properties do not affect the failure strength in this method. However, this method is "based on a thin shell approximation, and thus no distinction is made between internal and external cracks" [52]. Additionally, the formulas are derived on the basis of "fracture mechanics for cracks in tension" [52]. Our analyses focus on the corrosion on external surfaces. The corroded area in our analysis is subjected to compression because corrosion in compression yields a lower bending moment capacity, compared to tension.

Reviews show that experimental work incorporated with finite element analyses is still required for the study of pipe deformation and failure. In this chapter, I report experimental testing program results and validate finite element analysis results. Secondary effects in the experimental testing are also discussed. The experimental testing program was funded by Chevron Energy Technology Company, Houston during my summer internship in the Anchor, Mooring and Riser Team. I gratefully highly acknowledge Chevron for their generous financial support for this experimental work and for authorizing me to include test results in this thesis.

4.1 Finite Element Analysis

The critical scenario assumed in the analyses is that the pipe is hot and depressurized, so that only the bending moment is considered. Corrosion is represented as a local thin area (LTA), located at the bottom, axial center of the pipe subject to bending to yield a conservative analysis. The LTA is in compression as it yields a

lower bending moment capacity than that in tension. Consequently, large plastic deformation, the local buckling and ovalization are induced in LTA area. However, the failure mode I am interested in is the bending capacity of the corroded pipe, which is quantified by the maximum bending moment a pipe is able to sustain. ABAQUS [3] is applied for modeling and simulating the quasi-static response of corroded pipelines under bending moment.

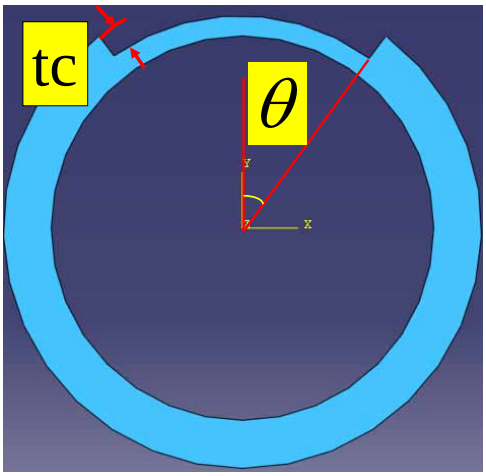

Figure 4.1: θ definition

As shown in Fig. 4.1, θ is defined as one half of total circumferential span of thickness reduction and t_c is the corrosion depth. As long as the products "$\theta * t_c$" are chosen to envelop the actual corrosion dimensions, the analyses are presumed conservative. Two models with 15° and 60° for θ are studied. These two models are assumed to be made of $X-60$ steel. The stress-strain relationship is commonly assumed to follow the Ramberg-Osgood relationship

$$\varepsilon = \frac{\sigma}{E} + \alpha \frac{\sigma_0}{E} (\frac{\sigma}{\sigma_0})^n \tag{4.1}$$

with Young's modulus $E = 207GPa$, yielding stress $\sigma_0 = 414.8MPa$, $\alpha = 1.03$, $n = 0.19$, ultimate stress $619.4MPa$ and Poisson's ratio 0.3. The LTA depth is 50%

of that of the pipe ($t_c = 5.2mm$).

Table 4.1: Principal Dimensions of 15° and 60° Models in the Finite Element Analyses

θ	15°	60°
Solid section outer diameter, OD$[mm]$	657.3	
Solid section thickness, $[mm]$	10.4	
Solid section length, $L_{AB}[mm]$	10.4	
LTA shape	oval	rectangular
LTA thickness, $[mm]$	10.4	
LTA axial length, $[mm]$	228.7	224.4
Shell section meridian diameter, $[mm]$	208.7	
Shell section length, $L_{BC}[mm]$	657.3	

Details of the models dimensions are shown in Table 4.1. In the table, lengths L_{AB} and L_{BC} are as shown in Fig. 4.2. As seen in Fig. 4.2, the section close to the LTA (from Point A to Point B) is modeled by solid elements and those far away from the LTA (from Point B to Point C) are modeled by shell elements. The shell-to-solid coupling is defined at the intersection.

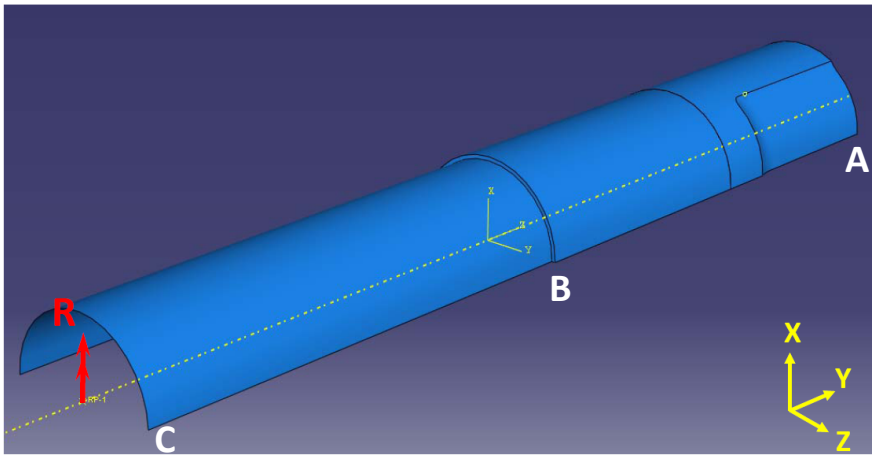

Figure 4.2: Finite element model

In the preliminary study step, symmetry permits the analyses of only a quarter pipe. Symmetry boundary conditions are enforced at the center cross section, A and

along the bottom of the upper half, A to C of Fig. 4.2. Rotational displacement is applied at point R to create a bending moment. This is a highly nonlinear problem. The nonlinearity exists from both large geometrical deformations and stress-strain relations with plasticity. The shapes of the LTA, however, are different for the two models. For the 15° model, the LTA is an oval with an elliptically shaped bottom; for the 60° model, it is of rectangular shape, with a flat bottom as shown in Fig. 4.3. For the 15° model, the elliptical bottom surface is automatically merged into the pipe outer surface by applying the "cut sweep" modeling function available in ABAQUS CAE. While, for the 60° model, the flat bottom surface and pipe outer surface are two independent surfaces. To connect them together, smooth round corners and rigid corners are applied. Correspondingly, the LTA is modeled separately for round and sharp corners, presented as rigid and smooth edges in Fig. 4.4, respectively.

Figure 4.4 also shows the bending moment capacity at the center of the LTA versus applied rotational displacement at point R (Fig. 4.2)for the 60° model. For these two different LTA types of modeling, the maximum bending moments are identical. Even though the rectangular shape with round corners modeling is a more accurate LTA representation, for a quick engineering calculation, the modeling with rectangular area and sharp corners gives a good estimation, with only 4.5% difference in the predicted post-buckling bending moment.

Significant numbers of simulations are done on different element types and meshing methods for the meshing sensitivity analyses to achieve bending moment convergence. As I am interested in deformation and moment sustained in the LTA, the further away from the center of LTA the part is, the coarser the meshing is. Figure 4.5 shows the typical meshing geometry of the two models. Both quadratic tetrahedron and brick elements are applied for meshing. Tetrahedron elements are

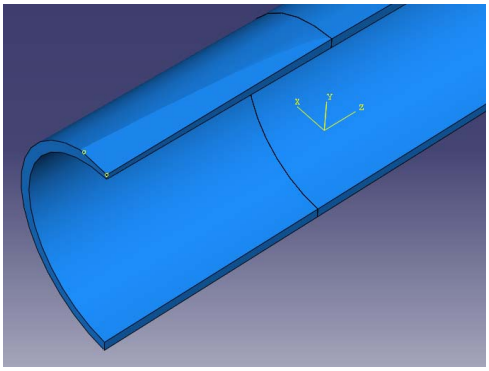

(a) LTA in oval shape

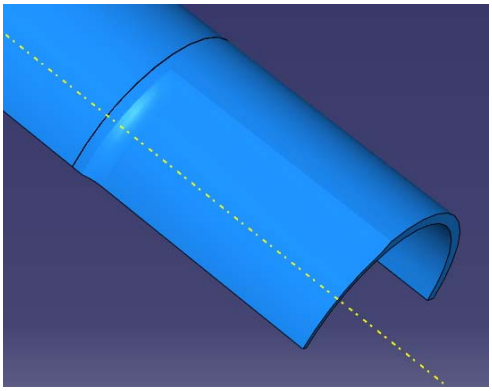

(b) LTA in rectangular shape

Figure 4.3: Two finite element models: (a) 15° model and (b) 60° degree model

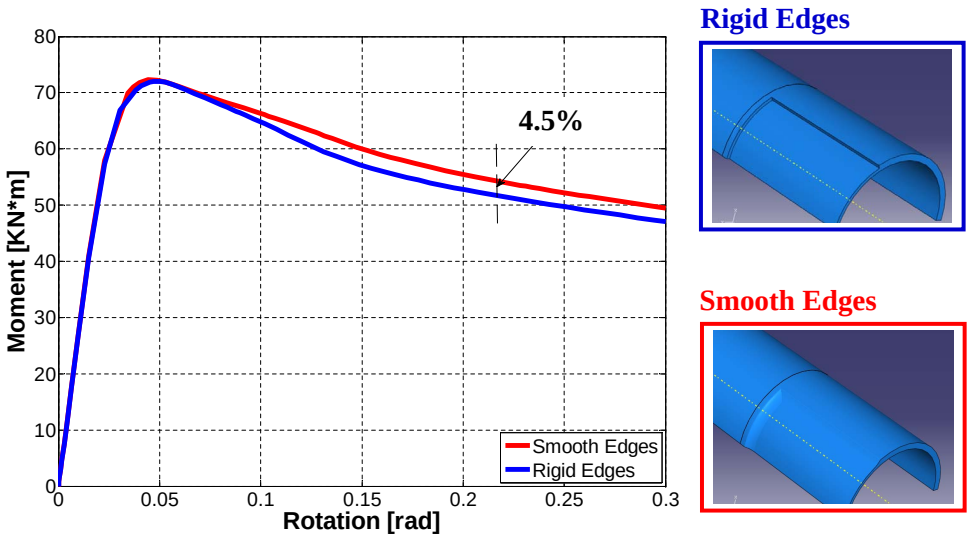

Figure 4.4: Moment-rotation results for the 60° model with different LTA geometry

preferred when complex geometry does not allow the application of brick elements, as for $\theta = 15°$ model.

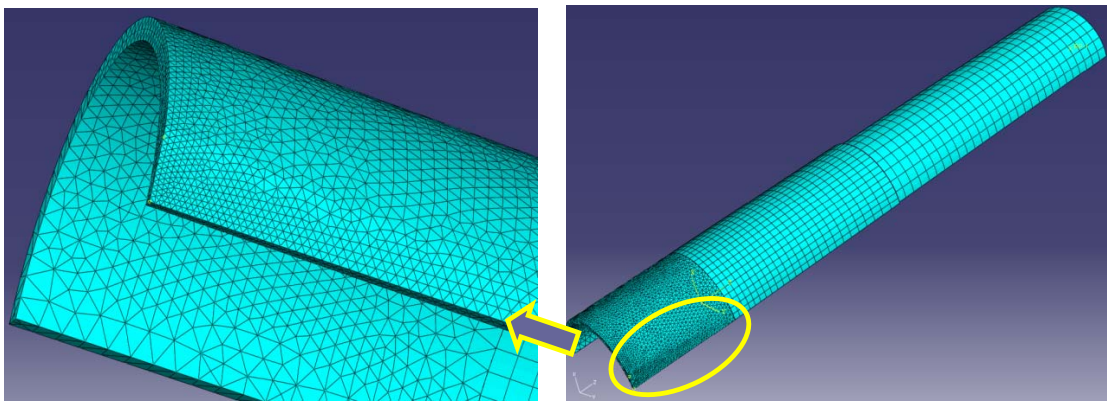

(a) 10-node quadratic tetrahedron element (C3D10M) meshing for 15° model

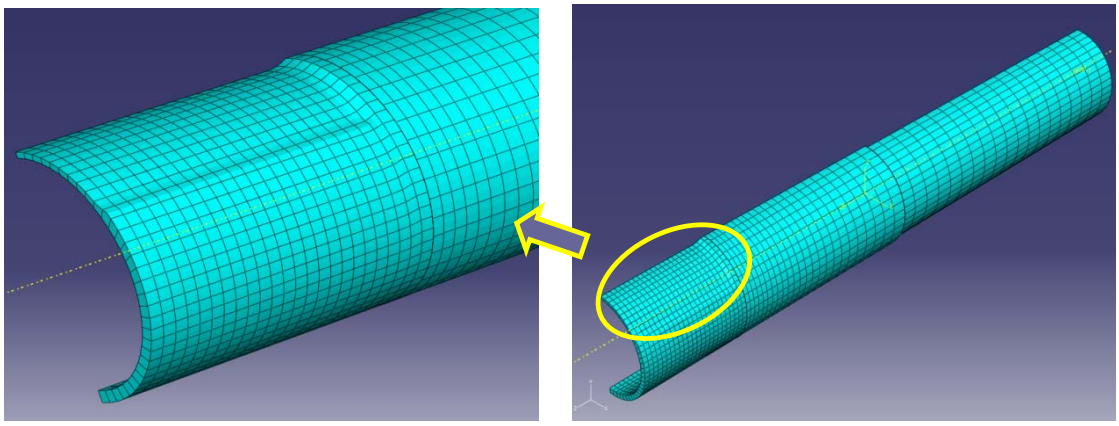

(b) 20-node quadratic brick element (C3D20R) meshing for 60° model

Figure 4.5: Element types for meshing: (a) quadratic tetrahedron element for the 15° model meshing and (b) quadratic brick element for the 60° model meshing

Figure 4.6 presents that moment sustained at the cross section of the center of the LTA (section A in Fig. 4.2) versus the rotation (applied at point R in Fig. 4.2) by applying different types of elements. The rotation is applied so that the LTA is in compression. The number in the parentheses in the legend represents the number of element layers through the thickness of the LTA. It is noticeable that in terms of the moment convergence, both tetrahedron and brick elements are adaptable within a certain range of element size. Moment values converged well for both types. The

light blue line in the figures corresponds to bending capacity of a virgin pipe. A large LTA decreases the buckling moment much more significantly than a small LTA does. This is a phenomenon also found in the experimental tests.

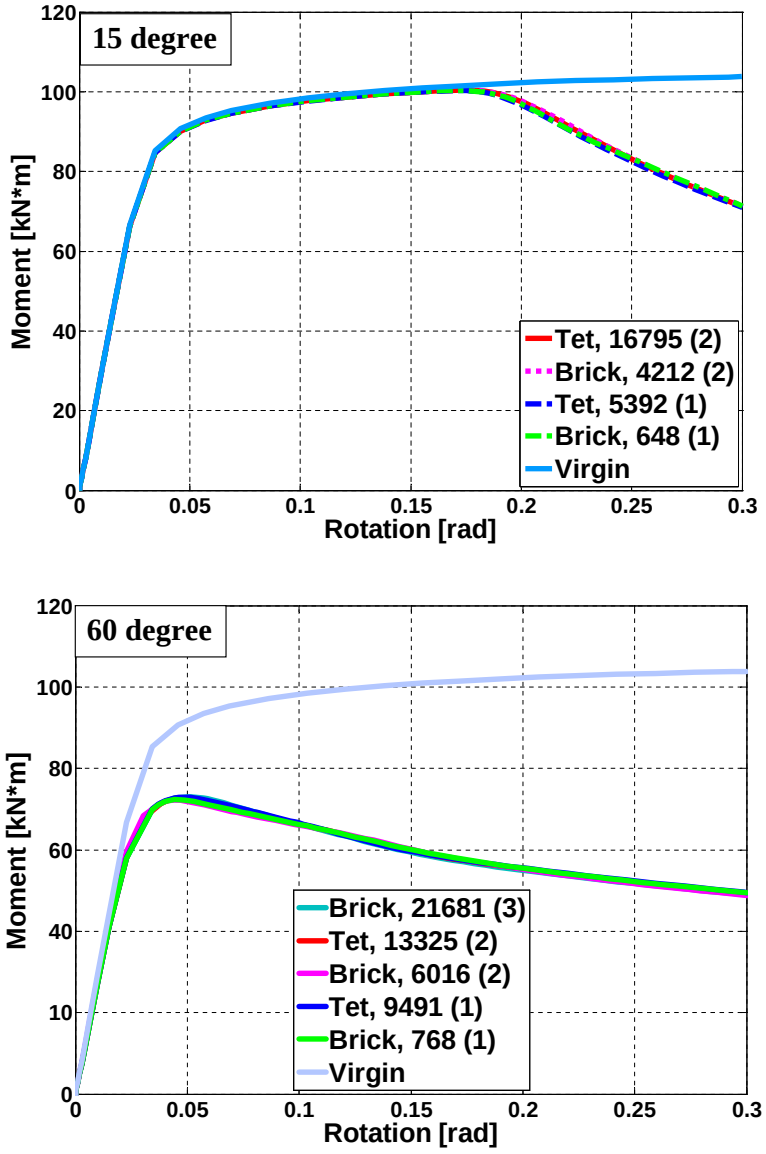

Figure 4.6: Meshing sensitivity analyses by element types

Comparisons are also made between linear and quadratic meshing. As shown in Fig. 4.7, both linear fully and reduced meshing are used on the 60° model. Here, "fully" means to use the number of Gaussian integration points necessary and fully

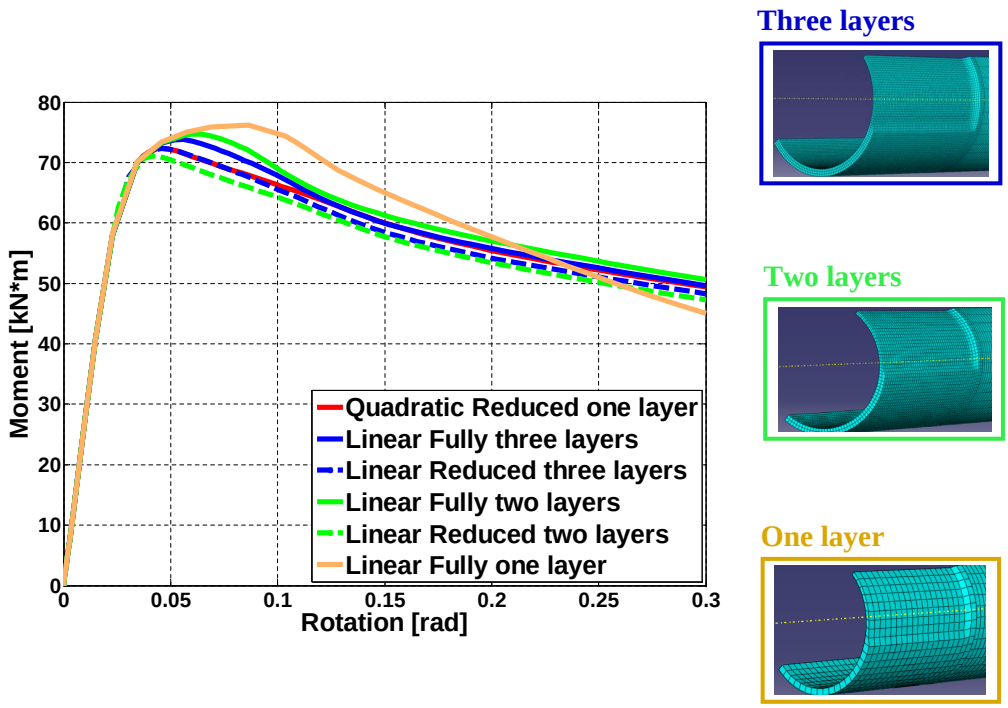

Figure 4.7: Meshing sensitivity analyses by linear meshing and quadratic meshing in the 60° case

integrate the entire element for the element stiffness matrix calculation; and "reduced" means to reduce the integration at a representative point within the element, such as the centroid, for the element stiffness matrix calculation. Apparently, reduced meshing is more efficient on computational time but also prevents excessive stiff behavior due to locking. Results are compared to those using the quadratic reduced meshing from Fig. 4.6. Only results of highly refined linear meshing are comparable to those of quadratic meshing. Although sometimes linear meshing gives a quick answer, it is not recommended for this analysis. Based on the above meshing analyses, further considering the meshing convenience, computational accuracy and cost, 20-node quadratic brick element was chosen for the rest of the analyses, whenever the geometry necessitates the application of brick elements.

4.2 Experimental Testing

This section focuses on the experimental testing program introduction and discussion. The testing program and the finite element analysis validation are discussed in detail in Section 4.2.1. During the FE validation, test induced tension, the end cap effect and internal pressure effect occurring in the test were discovered. Section 4.2.2 to 4.2.4 will discuss these effect on test results, respectively.

4.2.1 Testing Program Introduction and Finite Element Analysis Validation

In total, 10 specimens were tested for achieving plastic collapse of center corroded sections by applying the four-point bending method. The tests were conducted in the laboratory of *Stress Engineering Services Inc.*, Houston, Texas. Figure 4.8(a) presents the actual setup; corresponding to the setup, Fig. 4.8(b) also shows the highlighted configuration. As shown in Fig. 4.8(b), the bottom I-beam provides the foundation. Two cylinders in yellow are pistons loaded from the pressure reservoirs. Two blue braces constrain the motion of the specimen. Six red dots represent six strain gages attached on the specimen. Three green arrows show the positions where the displacement transducers are placed. As shown in Table 4.2, the global geometry and material grade are identical for all specimens. For the material properties, the Young's modulus is $E = 207GPa$ and the Poisson's ratio is $\nu = 0.3$. The engineering stress-strain curve is obtained from a tensile test as seen in Fig. 4.9. This curve is converted to a true-stress-plastic-strain curve for use in ABAQUS. Pipe bending specimens are 20 feet in length so that the end effect won't influence the local corroded area and the bending moment is constant in that area. This provided nonlinear geometric effects are neglected(see Section 4.2.3). The local corroded area is axially centered on the specimen. When a bending moment is applied, this area is always in compression.

(a)

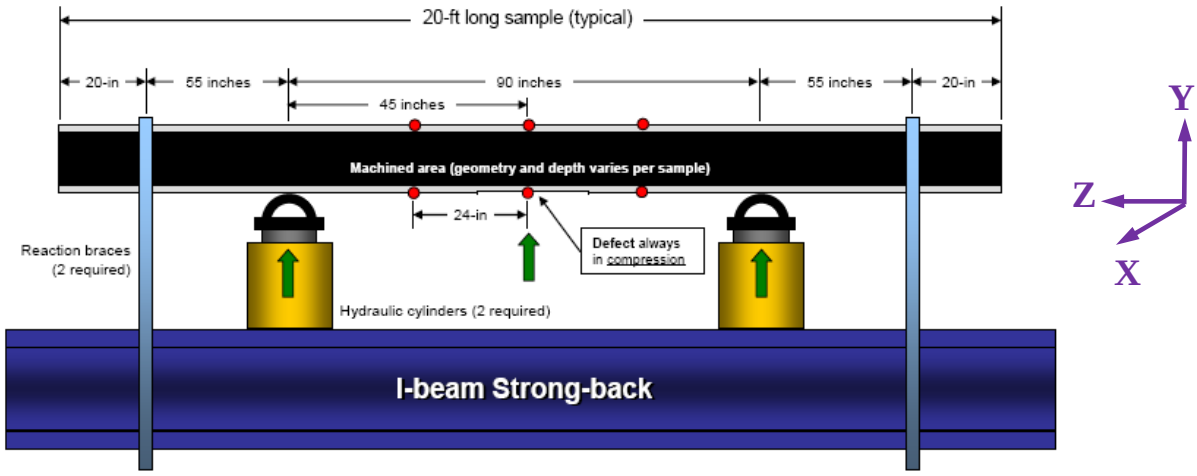

(b)

Figure 4.8: Experimental test program setup

Table 4.2: Geometry of specimens

Outer Diameter, OD	$8.625''(219.1mm)$
Thickness, t	$0.5''(12.7mm)$
Axial Length, L	20 feet $(6096mm)$
Grade	$X-52$

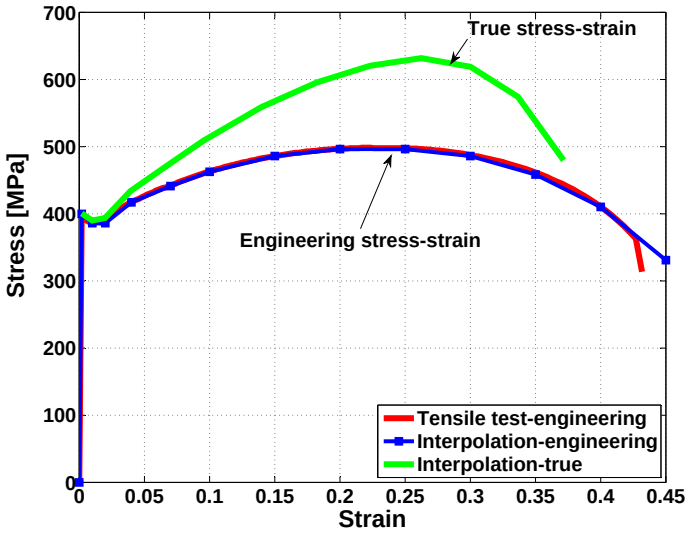

Figure 4.9: Stress strain curve from tensile test

Table 4.3: Details of specimens

Testing group	Specimen No.	LTA area (θ)	LTA depth (t_c)	Loading
1	1	15°	$\frac{1}{2}t$	bending moment
	2	30°		
	3	60°		
	4	90°		
2	5	30°	$\frac{1}{4}t$	bending moment
	6		$\frac{3}{4}t$	
3	7	virgin		bending moment
4	8	30°	$\frac{1}{2}t$	bending moment and internal pressure
5	9	45°	pit corrosion $d_c = \frac{1}{4}t$	bending moment
	10		pit corrosion $d_c = \frac{3}{4}t$	

To represent different physical and mechanical phenomena, 10 specimens are divided into 5 testing groups, as shown in Table 4.3. For specimen 8, the applied internal pressure is $24.94MPa$, which provides 60% of the yielding stress in the hoop direction. To provide internal pressure, water is pumped prior to tests and held constant during tests. Besides these rectangular flat-bottomed LTAs, some simulated pitting defects were also tested, as for specimen 9 and 10. Both LTA and the simulated pitting defects are machined to the specified level as shown in Fig. 4.10. The data acquisition system records internal pressure, displacement, load, and strain.

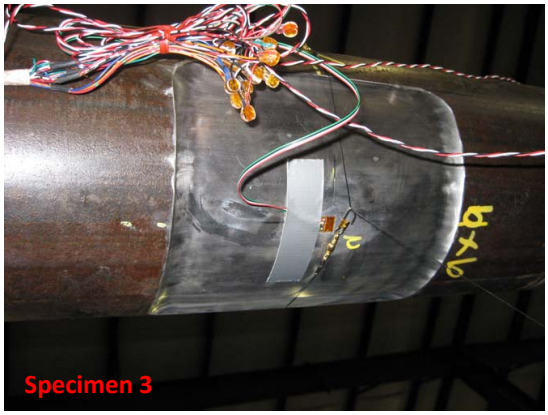

(a) Specimen 3

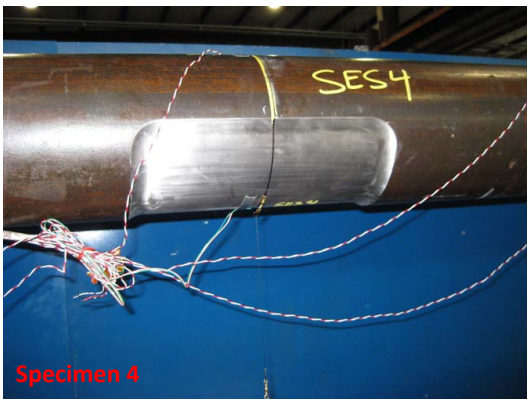

(b) Specimen 4

(c) Specimen 6

(d) Specimen 9 and 10

Figure 4.10: Defect of specimens

Representative specimens after tests are shown in Fig. 4.11. Specimens with small LTA span or small LTA depth, for example specimen 1 and 5, did not buckle. How-

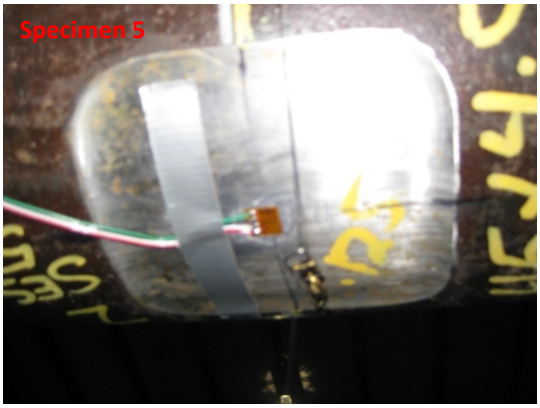

(a) Specimen 5

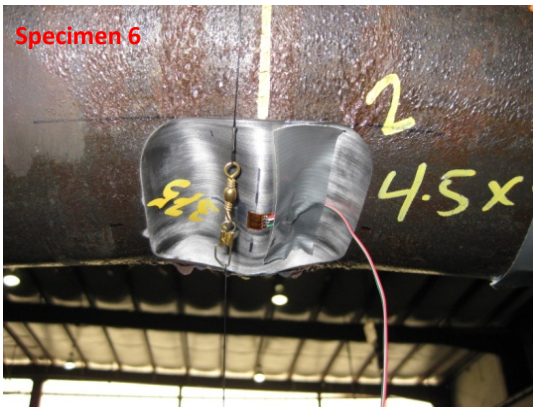

(b) Specimen 6

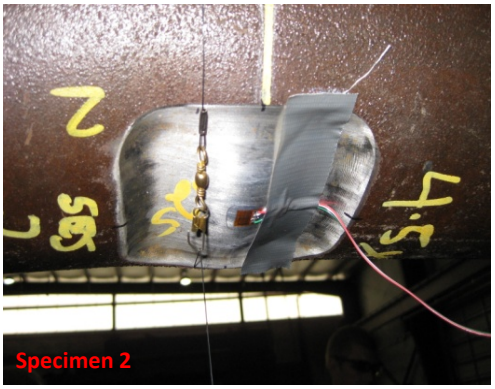

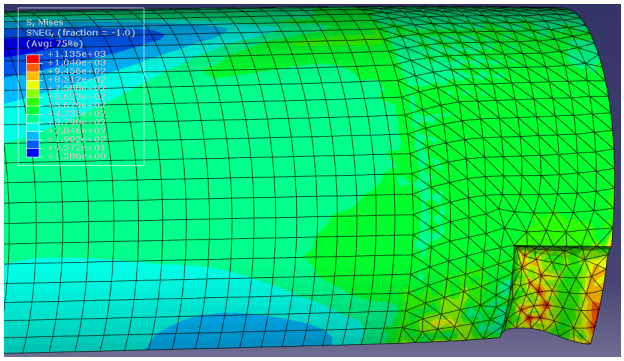

(c) Specimen 2

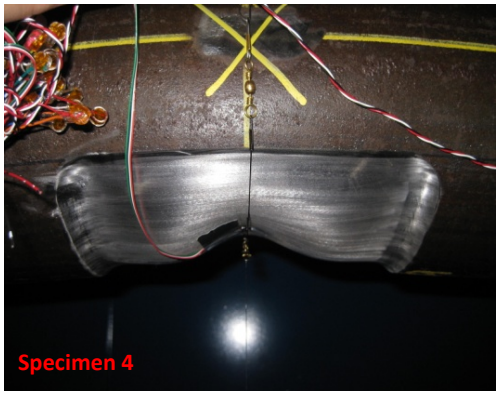

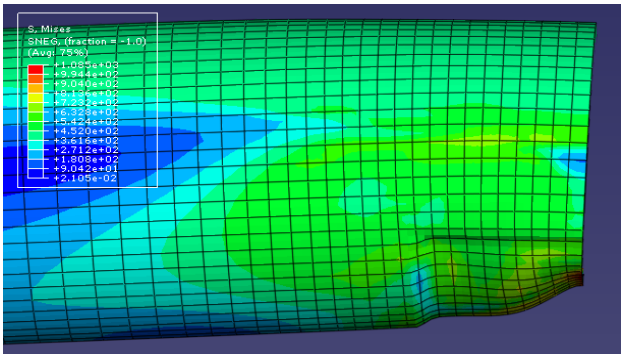

(d) Specimen 4

Figure 4.11: Specimens after tests

ever, with large LTA, buckling was very obvious as for specimen 3 and 4. Meanwhile, finite element analyses were performed based on the previous meshing sensitivity analyses. For specimen 2 and 4, the buckling shape of finite element model is consistent with what was found in the experiment tests as shown in the Fig 4.11(c) and (d).

In FE analyses, detailed specimen geometry and material properties was discussed earlier in this section. Meshing methods has been elaborated in Section 4.1. For boundary condition, they are defined as follows:

- At the center of the cross section which contacts the brace, displacements in X and Y directions are constrained. Coordinations are referred to Fig. 4.8(b). These conditions are corresponding to the constraint effects of the braces.

- At the center of the cross section which contacts the piston, rotation (about X axis) or displacement (along Y direction) are applied to bend the specimen. As constant bending moment as well as curvature are expected in the specimen portion between two pistons, specimen rotation can be calculated by knowing displacement measurements at three positions as shown by three green arrows in Fig. 4.8(b).

- Symmetry boundary conditions are applied at the center of a specimen so that only a half specimen is modeled.

By collecting all available test results, Fig. 4.12(a) shows the bending moment versus the rotation of each specimen. Two test results: 7 and 10, are not presented because of some difficulties encountered early in the testing program. These two tests were performed without putting saddles between pistons and specimen. The direct contact between pistons and specimen lead to the generation of local buckling at the

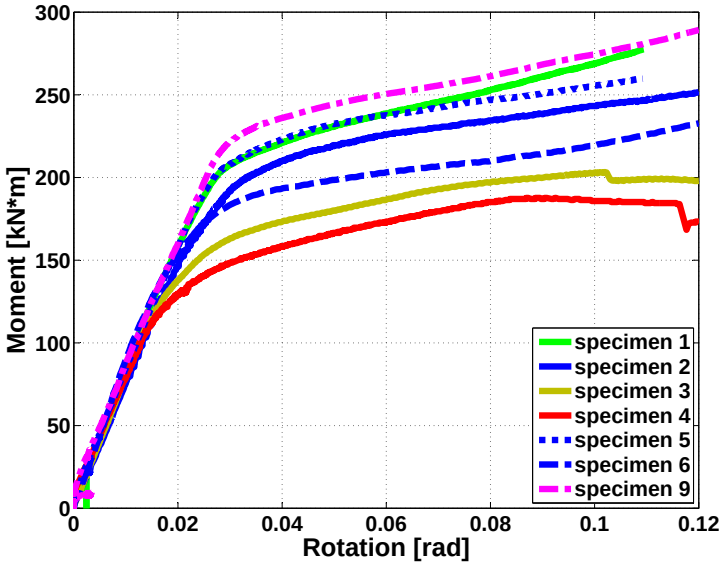

(a) Experimental testing results

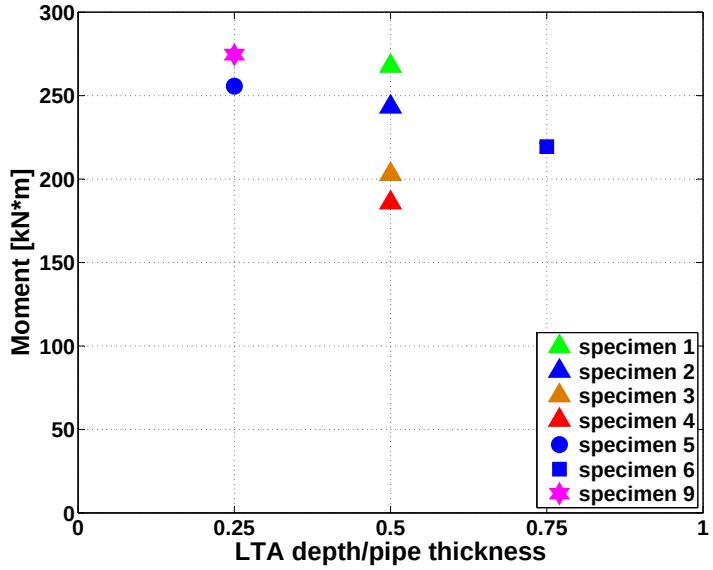

(b) Experimental testing results for rotation of 0.1 radian

Figure 4.12: Experimental test results

piston-specimen contact rather than the buckling at the LTA. As a result, data from those tests cannot reflect the integral failure of the specimen due to corrosion. So, these results are not included in Fig. 4.12. Specimen 8 is also not included as it is of the same LTA geometry of specimen 2 but under different loading conditions. In Fig. 4.12(a), the bending capacity decreases from test specimen 1 to 4. Specimen 1 to 4 are of the same LTA depth but the LTA area increases from 1 to 4. By comparing specimens among 5, 2 and 6, the bending moment decreases with the increase of the LTA depth for these three specimens, which have the same LTA area. At rotation equal 0.1 radian, the corrosion effect on pipes bending moment is shown in Fig. 4.12(b). The conclusion is obvious that larger LTA area and deeper LTA depth lower the bending capacity of corroded pipelines.

Figure 4.13 shows the comparison between experimental test and finite element analysis of 8 specimens (excluding specimen 7 and 10). Figures characterize the maximum moment capacity of all 8 test results. Note that axial tension forces are included in all FE results as discussed in Section 4.2.2. The axial tension is applied linearly by time step in ABAQUS. Additionally, due to safety concerns during testing, I was not able to approach specimens, nor were video apparatus available. The following failure mode discussion is based on my observations after each test.

For specimen 1, $2\theta = 30^\circ$ and LTA depth $t_c = \frac{1}{2}t$, as the LTA depth and area are small, it does not fail. But the specimen does go to the plastic deformation corresponding to the slope change of the curve. For specimen 2, $2\theta = 60^\circ$ and $t_c = \frac{1}{2}t$, both local buckling and ovalization occurs in the LTA area. Lüder band deformations in the form of 45° shear bands is very obvious close to the LTA area. But the specimen still shows sufficient ductility. For specimen 3 and 4, the LTA area is large and $t_c = \frac{1}{2}t$; local buckling and ovalization occur. Comparing Fig. 4.11(c)

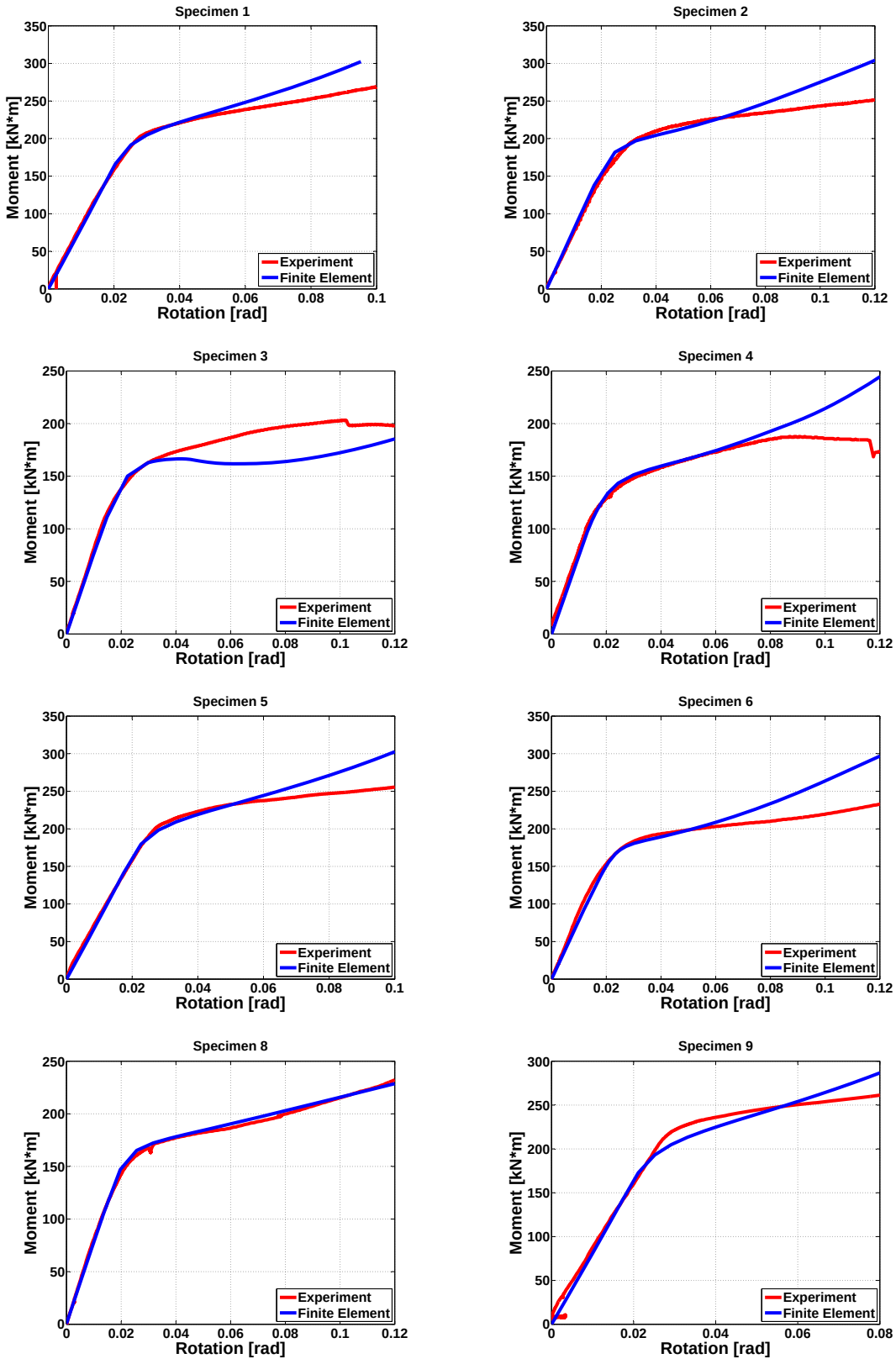

Figure 4.13: Experimental test and finite element analysis results comparison

and (d), the center of LTA is pointing outward for specimen 2, while it is wrinkling inward for specimen 4. I am able to conclude that pipelines with smaller LTA is more likely to fail by cross section ovalization; and those with large LTA are more likely to fail by local buckling. Specimen 5 and 6 are of the same LTA area but different LTA thickness. Specimen 5 ovalizes but does not buckle; specimen 6 buckles and ovalizes, and the LTA deforms similarly to that of specimen 2. Comparing bending moment capacity of specimen 2, 5 and 6, corrosion depth lowers the bending capacity as expected. For specimen 8, it will be compared to specimen 2 and discussed in detail in Section 4.2.4. For specimen 9, it does not fail as the overall material loss because of pit corrosion is quite small.

For one representative specimen, specimen 4, I plot the Von Mises stress at the center of LTA versus the rotation and compare it to the bending moment curve, as shown in Fig. 4.14. The elastic deformation is presented clearly in stress till line A; so is in the moment-rotation curve. Starting from where line A lies, the plastic deformation begins. The bending moment of the specimen is growing nonlinearly with the increase of the rotation. However, the stress increases more slowly. This is mainly due to the Lüder band deformation that occurs to about 2% strain shown in Fig. 4.9. Material in the LTA is straining harder, during which Lüder band is forming. Meanwhile, the cross section starts to ovalize, which decreases the section modulus. Between line B and C, the bending moment almost keeps constant while the Von Mises stress increases dramatically. This resulted from the onset of buckling in the LTA, which induces very high axial compression. Further bending the specimen beyond the line C, the sustained bending moment drops, indicating the bending collapse of the specimen. Note that beyond line C, the stress is larger than the maximum true stress in the stress-strain curve (Fig 4.9), which is yet unresolved.

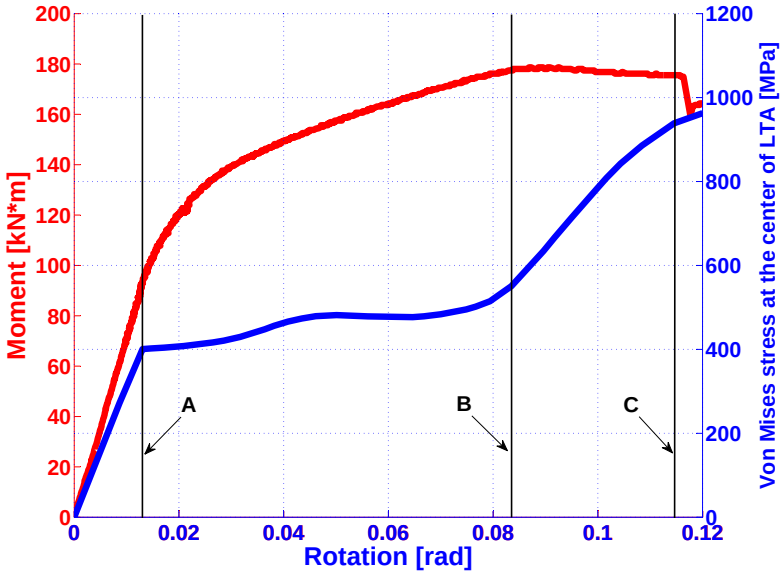

Figure 4.14: Moment and the corresponding Von Mises stress at center of LTA versus rotation for specimen 4

From elastic deformation until the maximum bending moment shown in the figure, overall good match is achieved between test results and FE results. Therefore, the finite element analysis results are validated by experiment test results. However, for most of tests an obvious peak moment is not seen as expected from a pure bending test. This is mainly due to the secondary effect found in the testing program, which are discussed in Section 4.2.2. The study of secondary effects enable me to capture most of the test results. The comparisons are improved between test results and FE results after this study.

4.2.2 Secondary Effects-Axial Tension

Relative to the middle, horizontal plane of the pipe, unsymmetrical strain states were found from test data for almost all tests. As an example, for specimen 4, shown in the Fig. 4.15, the strain history of strain gages $1, 3, 4$ and 6 are presented. Symmetrical strain distribution is found between strain gage 1 and 3, 4 and 6 but

anti-symmetrical strain is not found between strain gage 1 and 4, or 3 and 6. The maximum tensile strain, represented by strain gages 4 and 6 is 0.2%; in contrast, the maximum compressive strain, by strain gages 1 and 3 is 0.164%. The strain gage history indicates that the amount of stretching on the upper portion of the specimen is much larger than the amount of contraction of the lower portion.

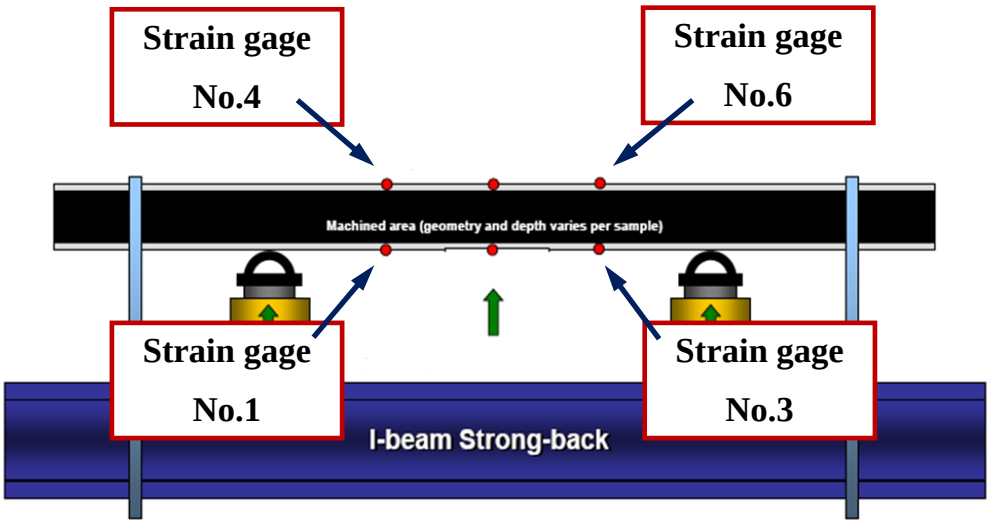

(a) Strain gage No.

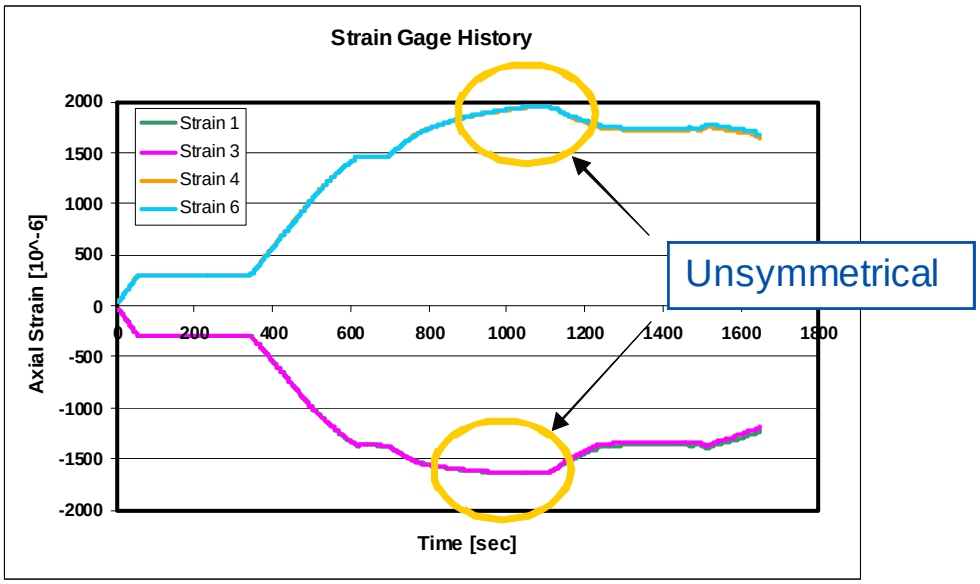

(b) Strain gage history

Figure 4.15: Strain gages

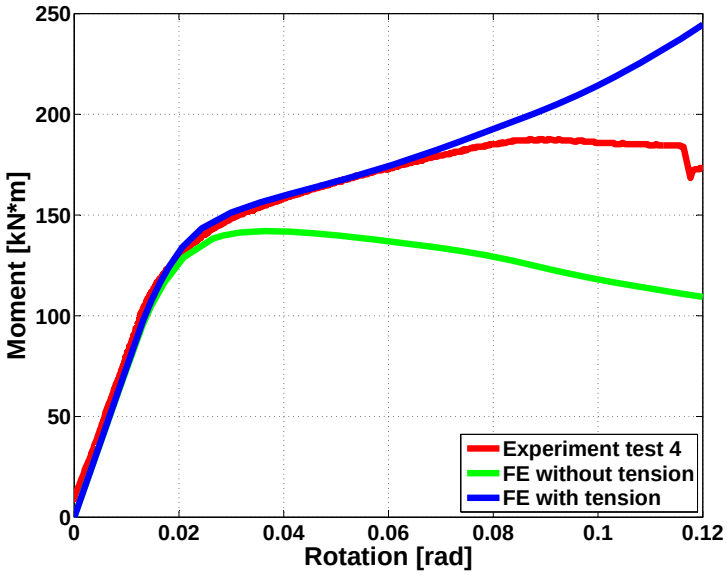

Figure 4.16: Added axial tension in the finite element analysis of specimen 4

Averaging the axial strain history of strain gages $1, 3, 4$ and 6, I find that a certain amount of tension is induced in the specimen. The maximum tensile strain value is about 0.2%, which represents the elastic deformation or just the onset of plastic deformation. So, Eq. 4.2 is used to approximately evaluate the axial tension induced by the non-zero average strain.

$$T = AE\bar{\varepsilon} \tag{4.2}$$

where A is the cross sectional area of the specimen; E is the Young's modulus and $\bar{\varepsilon}$ is the average strain of strain gage $1, 3, 4$ and 6 when maximum strain values were obtained, which is 0.023%. Therefore, for this specimen, a roughly estimated (upper bound) axial tension is $388KN$, which is linearly applied in FE modeling. This axial tension should be equivalent to the extra stretching of the specimen.

In the FE analysis, this tension is applied at the origin of the cross section, whose outer surface is contacting the hydraulic cylinder. As shown in Fig. 4.16, comparisons were made first between test result and finite element analysis without

including tension for specimen 4. There is a significant drop of moment capacity in the finite element analysis results without including axial tension. Such discrepancy is evidently reduced by adding the axial tension in the finite element analysis. The FE results which includes the axial tension agrees with the experiment test results much better than ones excluding the tension. The axial tension should be applied to all tests to catch the moment capacity in experimental test. Again, the moment-rotation curve under pure bending should have had a peak. In this experiment test, it is because of the generated axial tension that pure bending was not achieved so that for some test specimens, no peak moment is obtained.

This amount of axial tension is induced by specimen stretching, the friction between saddles and the specimen, the friction between braces and the specimen and the rotation of pistons as found during the tests. To accurately include these factors for a better representation of the experimental test, a full model is further created in the finite element analysis. The full model includes the specimen, the brace to constrain the specimen axial motion and the saddle to provide a distributed lifting force as shown in Fig. 4.17(a).

The saddle is modeled as a half piece of cylinder, with the outer diameter $273.1mm$, the thickness $12.7mm$ and the axial length $266.7mm$. As shown in Fig. 4.17(b), point Q centered on the outer surface couples to the saddle so that rigid body motion and rotation of the whole saddle is attached to this point [3]. A displacement in the Y direction equal to $131mm$ provided from the hydraulic cylinder is also applied at point Q to simulate a distributed lifting force. This corresponds to the maximum displacement of the hydraulic cylinder in the test. Contact is defined between the saddle inner surface and the pipe outer surface as shown in Fig. 4.17(c) through a "surface-to-surface contact definition" [3], in which the tangential friction ratio is

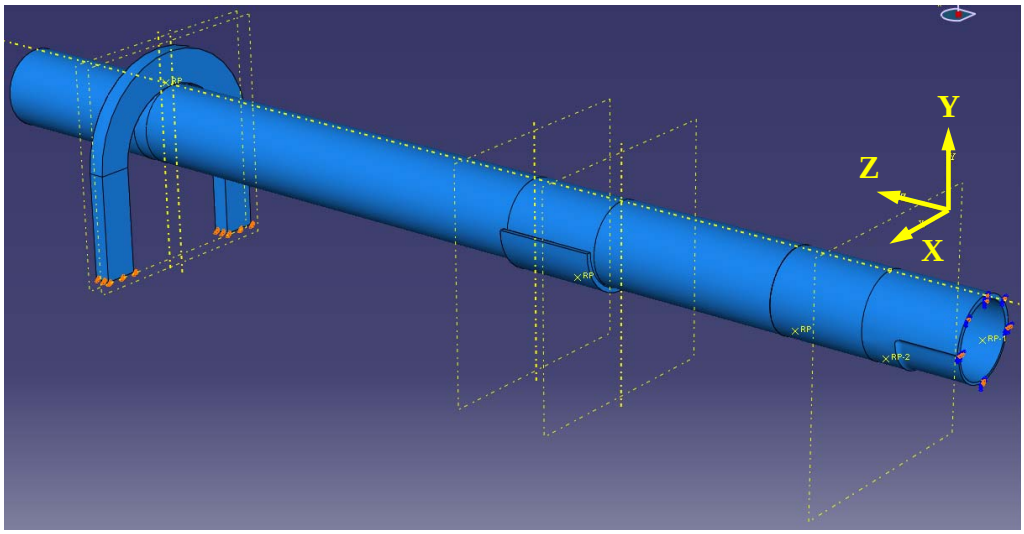

(a) Full model

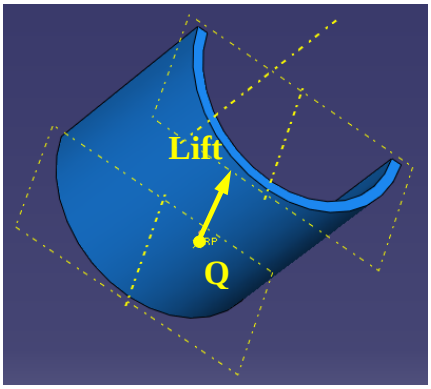

(b) Lifting force on saddle

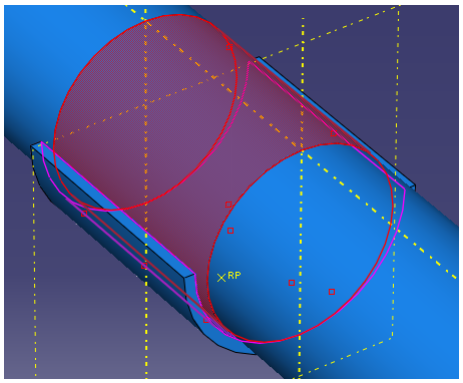

(c) Contact at saddle

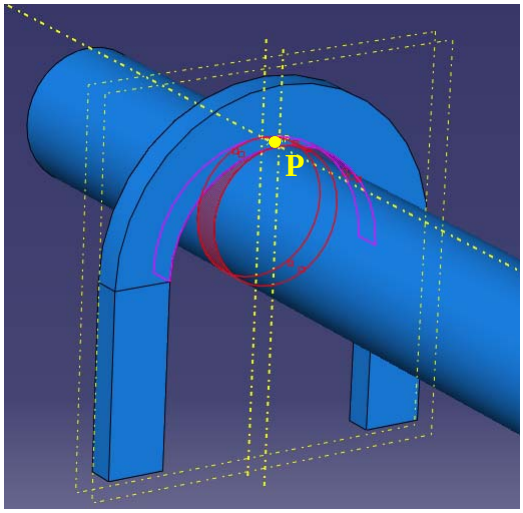

(d) Contact at brace

Figure 4.17: Full model in the finite element analysis of specimen 4

defined 0.3.

The brace is 579.4mm in height, 45.7mm in length along pipe axial direction, 368.3mm in diameter of the inner arc surface and 558.8mm of the outer arc surface. Contact with the same property as saddle is also defined between the brace inner surface and the pipe outer surface as shown in Fig. 4.17(d). Displacements in X, Y and Z directions are constrained at the bottom of the brace. The net axial tension generated in the simulation of the full model is about 41.3KN. This value is the real axial tension induced in the FE analysis. Compared to the elastic estimation (388KN), this value is quite different. However, without modeling the contact between the specimen and the brace, and between the specimen and the saddle, the previously estimated axial tension (see Eq.4.2) is able to quantify all factors. Thus, by adding the estimated value in the FE analysis, good matching to the test result is achieved. Again, the success in modeling the actual experimental setup proves the induced axial tension as a secondary but important effect found in the tests.

4.2.3 End Cap Effect

Roy et al. [94] discussed the end cap effect in the finite element simulation for pipe bending under combined loading conditions. They concluded that the end cap effect is vital for the model under combined axial loading (compression) and internal pressure. A similar conclusion is also drawn in the study of test 8, in which the specimen is under the combined internal pressure and bending moment. During this test, an internal pressure of 24.94MPa was applied prior to testing by pumping in water. This internal pressure was held constant ($\pm$0.35MPa) during the test. The end cap was initially not modeled in the FE simulation. Instead, an equivalent force as a result of internal pressure was applied to the cross section at the end of the specimen. The FE bending moment capacity result is lower than the experimental

results as shown in Fig. 4.18.

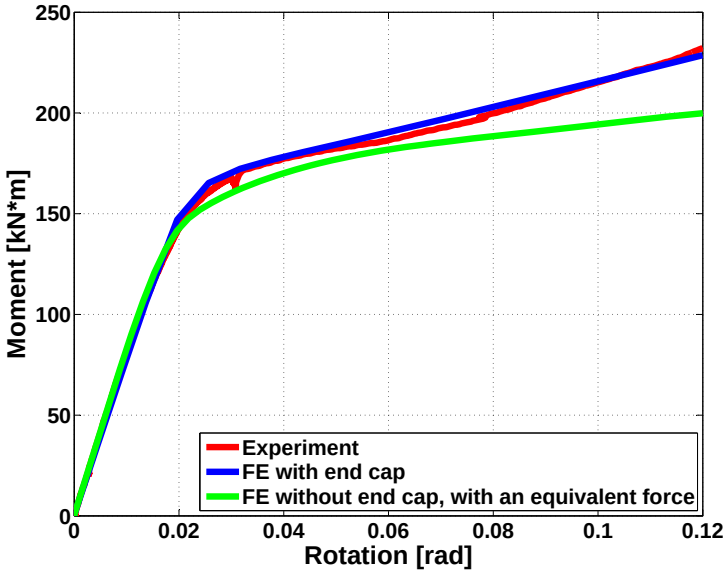

Figure 4.18: End cap effect of test 8

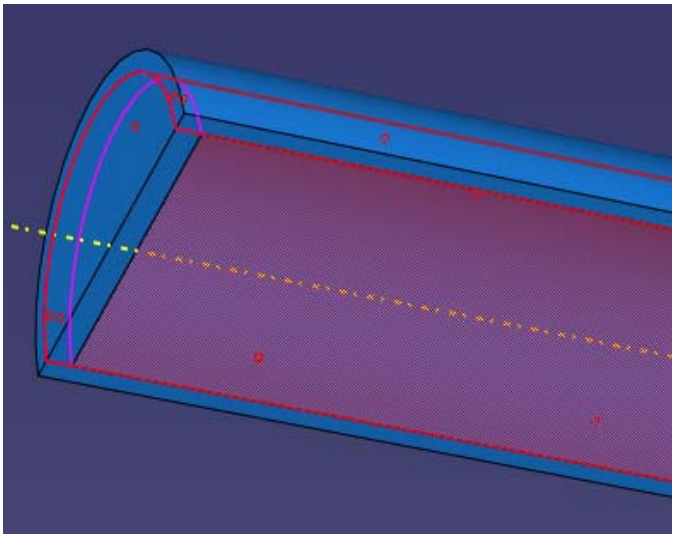

Figure 4.19: Tie constraint between the end cap and the pipe

Therefore, an end cap is modeled, with the diameter 193.675mm and the thickness 15mm. A surface-based tie constraint is applied between the end cap and the pipe as shown in Fig. 4.19. In the figure, the surface in red is the pipe inner surface and

that in pink is the surface of the end cap. This tie constraint can be used to "make the translational and rotational motion as well as all other active degrees of freedom equal for the pair of surfaces defined in constraint" [3]. Including both the end cap and the previous discussed axial tension, the comparison between the test bending moment capacity and the FE result is improved, as shown in Fig. 4.18. This result indicates that even though the end cap is placed far away from the center LTA, it still constraints the pipe's bending somewhat. Therefore, proper end cap modeling is recommended for similar problems in the future.

4.2.4 Internal Pressure Effect

Specimens 2 and 8 are of the same geometry but under different load conditions. Specimen 2 is only under bending moment while specimen 8 under combined internal pressure and bending moment. The initial estimation was made for a lower bending moment capacity of specimen 2. As for large D/t specimens where the compressive buckling initiates elastically, internal pressure has the potential of increasing the moment capacity. Additionally, in the work of Kim and Park [51] on the failure study of carbon steel pipe with wall thinning, they conducted experimental tests on pipes with wall thinning under bending moment and internal pressure. They reported that internal pressure increases the load and deformation capacities of such pipes. However, our experimental test challenged our initial guess by showing a lower bending moment for specimen 8 than for specimen 2.

Results for both specimens are presented in Fig. 4.20. The results indicate that the more critical scenario is for a pipeline under the combined internal pressure and bending moment. This is because when pipes deform plastically, the internal pressure increases the hoop stress; meanwhile, the applied bending moment increases the axial stress. Both stresses lead to a higher Von Mises stress at the center LTA.

Therefore, a lower bending moment is sustained in a pipe under combined loading. As a conclusion, the most critical scenario in the pipes of $D/t = 17.25$ and of Grade $X - 52$ steel is that the pipe sustains internal pressure under high temperature.

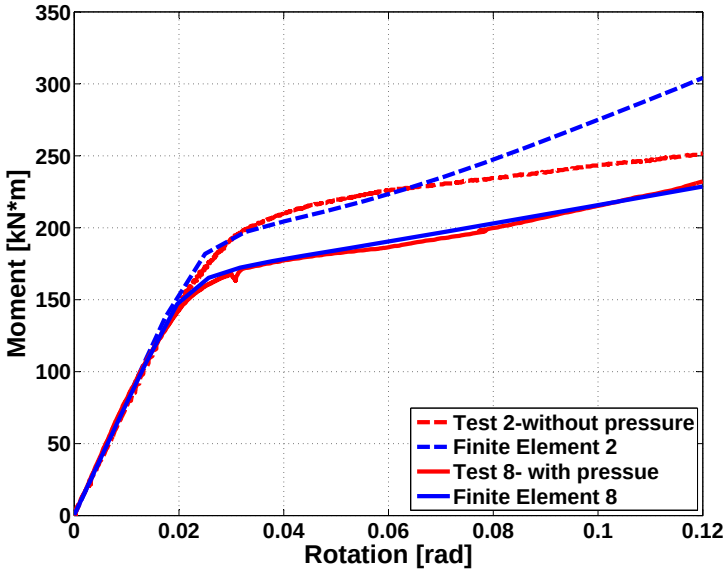

Figure 4.20: Internal pressure effect

4.3 Conclusion

Major conclusions from this work are summarized as follows:

- Corrosion reduces pipes bending capacity.
- Finite element studies show that for the accurate computation of bending capacity of corroded pipelines:
  - quadratic elements, brick or tetrahedral are recommended,
  - accurate modeling of the edge smoothness of the LTA was not important, and
  - some examples of adequate refinement are given in the chapter.

- Properly executed, the finite element approach recommended accurately predicts the maximum moment capacity of a corroded cross section, and the buckled shape.

- Significant secondary effects are apparent from the experimental measurements. Due to experimental setup, a gross tensile loading develops in the specimen that increases the test moment. Using a full-scale FEA model with test support constraints included, this tensile force was duplicated. Such test set-ups thus produce both moment ana a (stabilizing) axial force. Moment capacity prediction may thus be unconservative.

- The end cap effect is also contributed to the moment capacity. Comparisons show that the end cap modeling is needed for pipe bending under internal pressure. The best approach is to carefully include both the end cap loading and the gross tensile load that develops due to the test setup.

- For this D/t ratio and strength (i.e. $D/t = 17.25$, Grade $X - 52$ steel), the application of an internal pressure reduced the LTA's bending capacity. For large D/t specimens where the compressive buckling initiates elastically, internal pressure has the potential of increasing the moment capacity. Future work is proposed to investigate the internal pressure effect on corroded pipes of various dimensions and grades.

- Further work is proposed to use the finite element models for the assessment of bending capacity for the generation of simplified closed form formulas similar to $B31G$ [8].

CHAPTER 5

Stress Concentration Factors and Reliability of Pitted Plates

In deterministic failure analyses of corroded plates, the stress or strain relationship between load and defect needs to be established. The analyses are then performed according to certain failure criteria. Seeger and Heuler [98] pointed out that there are mainly three existing methods to determine a stress or strain relationship between load and defect: "analytical study, experimental tests and finite element (FE) analysis".

For a structure, however, the real scenario is that uncertainties are involved in the defect geometries, material properties and loading conditions. Hence, probabilistic analyses are needed to include these uncertainties and to achieve a consistent safety level. In reliability based safety analysis, probabilistic analyses are of primary importance. Reliability assessments are useful and powerful to help make decisions in safety analysis, design study and tests, repair and maintenance strategy developments.

The initial focus of this chapter is on deterministic fracture initiation based on load-defect stress or strain relationships. The attention focuses on a stress concentration factor (SCF) study in such relationships. Then considering the randomness in the structural geometries and loading conditions, different levels of reliability studies are performed on the structure fracture failure which includes the stress and strain

concentration effect due to corrosion.

Stress concentration is a common topic in the field of mechanics, which has been given tremendous attention for decades. Stress concentration is due to localized geometrical imperfections and shape changes. For example, holes, notches, grooves, or their combination are phenomena inducing stress concentration in structures [77]. Stress concentrations can also result from certain material properties variations. Stress concentration study is indispensable for structure design and failure analyses including both structural elastic and plastic deformations. Since the study of stress concentration started from the second half of the $19th$ century [77], a great amount of both theoretical and numerical analyses have been done.

Neuber and Hahn [77] pointed out the importance of an early systematic stress concentration study developed by Lehr [57] in 1934. The study was improved by Neuber, who summarized the common stress concentration calculation and finished the famous book "Kerbspannungslehre" [78]. Neuber was the first person to establish procedures for fundamental stress concentration calculations. Most of the theoretical solutions available in Neuber's book were derived with the assistance of complex stress functions, first developed by Kolosov [55]. As early as 1909, Kolosov used this method to obtain the stress distribution of an infinite sheet with a center elliptic hole under tension. Another significant contribution of this method is reflected in the obtaining of approximate solutions [77].

Results of stress concentration mentioned in the previous paragraph are only valid under the theory of elasticity, i.e. "homogeneous, isotropic material with linear stress-strain relationships" [77]. In plasticity, the stress concentration factor is highly dependent on load amplitude. The factor is far more difficult to obtain, even for the practical important case of a circular hole in an infinite plate under uniaxial tension.

Budiansky et al. [18] for the first time related the plastic stress concentration result to the elastic part. They [17, 18] were able to approximate the plastic stress distribution by employing the deformation theory. They used the Ramberg-Osgood equation for the material constitutive law. Later on, Neuber [76] introduced a "leading function", through which the maximum stress, nominal stress and the elastic SCF are connected for a notched prismatic body under transverse shear. This approach leads to the result that the product of the stress and strain concentration factors equals the square of the elastic stress concentration factor [77]. Neuber further extended the application of this conclusion on a notched body under arbitrary loading conditions for any stress-strain relationship; but effective (Von Mises) stress and effective strain must be used for the stress and strain concentration factor calculation.

These researchers' great contributions made the derivation of some analytical solutions possible. Still, there have been very few analytical solutions available compared to the broad need of such solutions. As mentioned by Panc [85],

> "As the direct determination of the stress state corresponding to the given nominal stress is extremely complicated, it will be necessary for the solution of every special problem to investigate some possible stress states. Therefore the suitable arrangement of the numerical solution is of the highest importance."

The representative method for numerical analysis of SCF is the finite element (FE) method. FE analysis can be used to substantiate the newly derived analytical solutions. Moreover, in many cases, without available analytical solutions of SCF, finite element method is a powerful tool for the elastic-plastic, plastic or even dynamic analyses of stress concentration problems. Previous work, for example Sørbø and Härkegård [1] and Härkegård and Mann [39], has shown that finite element results

agree very well with analytical solutions, especially for shallow mild defects.

The above theoretical solutions will be mainly applied on a limited scale of components with defects in regular shapes. For more practical problems, it is very likely that theoretical stress concentration factors are not available. Under such circumstances, experimental methods show their powerful and indispensable abilities. Photoelasticity is an experimental method extensively used in many types of plane stress concentration problems [77], especially for structures under combined loading conditions and with multiple notches or holes [33, 42, 45, 110].

As mentioned in the previous chapters, among all geometrical or material defects, especially for ships or offshore structures, pit corrosion is inevitable and can be critical. According to statistics of hull structure damage [79, 80], corrosion (including pit corrosion) starts to appear often roughly at about eight years [54], and older ships are susceptible to fracture mainly due to severe corrosion. The reduction of hull cross sectional area due to pit corrosion may cause fractures to occur. The study of stress concentration resulting from pit corrosion becomes significant and indispensable in the design, testing and maintaining of ship and offshore structures. However, compared to the available SCF formula for notches or holes, that for pit corrosion has not been fully developed.

Eubanks [31] in 1954 first derived the analytical solution of a semi-infinite elastic body containing a hemispherical pit under hydrostatic tension parallel to the free surface. Yet, later on, Fujita [34] and Atsumi [9] pointed out that Eubanks overestimated the SCF at the bottom of the pit. Saito et al. [95] and Tsuchida [111] analyzed the similar half-space problem under uniaxial tension and axisymmetric pressure, respectively. Fujita et al. [108] worked on the approximate analytical solution of a thick plate corroded by a hemisphere pit under biaxial loading. Those mentioned

hemispherical pit problems were solved with the help of stress functions. Yet the convenience of using the stress functions were only represented for hemispherical pits under limited loading conditions.

Reliability analysis has been widely used in structure system design, testing and maintenance to estimate the structure failure probability. The analysis is related to the definition of a limit state; for example a limit state can be when load applied on a structure exceed the structure's resistance. The limit state design was developed by the Comité Européen du Béton and the Fédération Internationale de la Précontrainte [56]. Based on a certain failure criteria, limit state design is established by including randomness appearing "in the loads acting on the structure or in the strength of structural materials" [56]. Statistical methods are employed to reveal different uncertainty levels of these random variables in the limit state design. A limit state function is usually used to express critical load-strength (resistance) effects. Through a limit state function, structure integrity is quantified by a reliability safety index corresponding to the probability of failure.

In general, there are two major limit states used in design: the ultimate limit state and the serviceability limit state [19]. In the words of the researcher Burdekin, "the ultimate limit state is when the structure actually fails and the serviceability limit state is when the performance of the structure is impaired to an unacceptable extent" [19]. In different fields of reliability application, the limit state can be defined variously. For example, in the structural analysis of ship hulls and pipelines, four kinds of limit states relate the failure modes: "the ultimate limit state, the serviceability limit state, the fatigue limit state and the accidental limit state" [84].

Based on the classification system of the Joint Committee on Structural Safety [46, 47], there are three methods for structure reliability analysis and design: Level 3,

Level 2 and Level 1. Level 3 directly uses the full probabilistic description (joint probability density function) of all random quantities to determine the exact failure probability for structures. Level 2 avoids using the full probabilistic description. Instead, it applies certain iteration procedures to connect the failure probability to a structure safety index. Level 1 can be regarded more as a design method as the structural reliability level is determined by the use of partial safety factors. The structure safety level is actually the result of the cumulation of partial safety factors for structural strength and load variables [109].

Both analytical and numerical simulation methods are generally applied to the limit state function and to solve for failure probability [12]. Analytical methods include fully probabilistic method, the first-order and the second-order (second-moment) reliability method (FORM and SORM). FORM and SORM are simple to apply and do not require extremely large computational resources and time. However, as a result of certain assumptions, these methods unavoidably give only approximate results. Monte Carlo (MC) simulation method is an alternative tool for the failure probability prediction [12]. It is a simple method for application and relies on repeated random input to compute the corresponding output. Many researchers describe this method as a "black box" as the method itself is actually a class of computational algorithms [120]. The advantage of MC simulation is that it is easy enough to be implemented into a computer program for even very large sample sizes. Therefore, the estimated MC probabilistic descriptions are convergent to exact results. However, it is often not efficient, as the calculation itself requires a very large number of repetitions of the same procedure of simulation.

Reliability analysis has not only been widely developed and used in civil engineering, but also in the naval architecture and marine engineering, often taking

into account corrosion effect considerations. Dunbar et al., Garbatov and Guedes Soares [5, 105, 106] presented time variant formulations to account for the effect of corrosion and fatigue on the reliability of ship hulls. The degrading effect of general corrosion is reflected in the decreased thickness of the plate which in turn decreases the moment of inertia of the ship cross section and thus induces higher stress level for the same applied bending moments. The formulation is able to accurately assess the degrading effects of both crack growth due to fatigue and corrosion on both instantaneous and time-dependent reliability. Parunov and Guedes Soares [86] further considered the reinforcement of initial designed members and calculated ultimate strength failure probability of both initial designed and reinforced ship hulls. Ship hull failure modes for sagging and hogging are considered in the limit state development, respectively. Both sensitivity and parametric studies are performed and the results show that the uncertainty in the ultimate strength is the most important random variable for the reliability calculation [86].

My work targets reliability analysis of a representative pit-corroded plate, whose nominal deformation is amplified by the presence of a center pit. The amplification effect is induced by Neuber's stress/strain concentration factor, which depends on pit geometry. Section 5.1 briefly introduces the Neuber's theory for both elastic and inelastic material response. The analytical solution is calculated for a notched specimen, whose geometry is related to the pitted plate. In Section 5.2, the focus is put on the numerical study of stress concentration factor by applying the finite element (FE) method. The FE method is verified by Neuber's analytical solution and further applied on the stress concentration factor estimation for a pitted plate.

In Section 5.3, different levels of reliability analyses are discussed in detail. The iterative procedure for partial safety factor calculation is introduced. In an example

of dented bottom shell panel in ship grounding, reliability analyses are conducted to calculate the reliability safety index of the panel based on a strain control and partial safety factors of two random variables which describe pit corrosion geometry and the nominal strain level, respectively. The Neuber's stress/strain concentration factor for this pitted bottom plate is incorporated into the reliability study. Recommendations for the use of partial safety factors are provided. These values will be of great interest and of practical use for naval architects.

5.1 Neuber's Theory: Elastic and Inelastic Material Response

For an isotropic homogeneous component, nonuniform distribution of the stress may occur because of the geometry or material changes in the cross section. For a specimen with area A subject to an axial force P, nonuniform stress distribution may lead to a maximum stress, σ_{max}, greater than the average stress, $\sigma_{ave} = \frac{P}{A}$ [16].

As a leading researcher, Neuber first studied notch-induced stress concentration factors in 1946. In Neuber's elastic rule, the stress concentration factor is first defined as

$$S_{cc} = \frac{\sigma_{max}}{\sigma_n} \tag{5.1}$$

where σ_{max} is the maximum stress at the root of a notch or other defect and σ_n is defined as the nominal stress on the cross section at a notch or other defect. By obtaining S_{cc} in the elastic regime, Neuber's inelastic rule can be further applied to predict the maximum effective stress/strain when the plastic deformation is only dominant around the notched area [39]. Effective stress and strain are defined in Eq. 5.2 and 5.3.

$$\sigma_e = \sqrt{\frac{3}{2}\sigma'_{ij}\sigma'_{ij}} \tag{5.2}$$

$$\varepsilon_e = \sqrt{\frac{2}{3}\varepsilon'_{ij}\varepsilon'_{ij}} \tag{5.3}$$

where σ'_{ij} and ε'_{ij} are denoted the deviatoric stress and deviatoric strain respectively [1]. The Neuber's inelastic rule applied in uniaxial tension P is shown in Fig. 5.1 [16]. In Fig. 5.1(a) and (c), curves CD and $C'D'$ stand for the stress and strain distributions, respectively. Exceeding the elastic regime, the maximum effective stress σ_{max} can be determined in terms of stress concentration factor as

$$\sigma_{max} = S_{ce}\sigma_{ne} \tag{5.4}$$

where S_{ce} represents the effective SCF in the inelastic regime to differentiate from S_{cc}, which describes the SCF in the elastic regime.

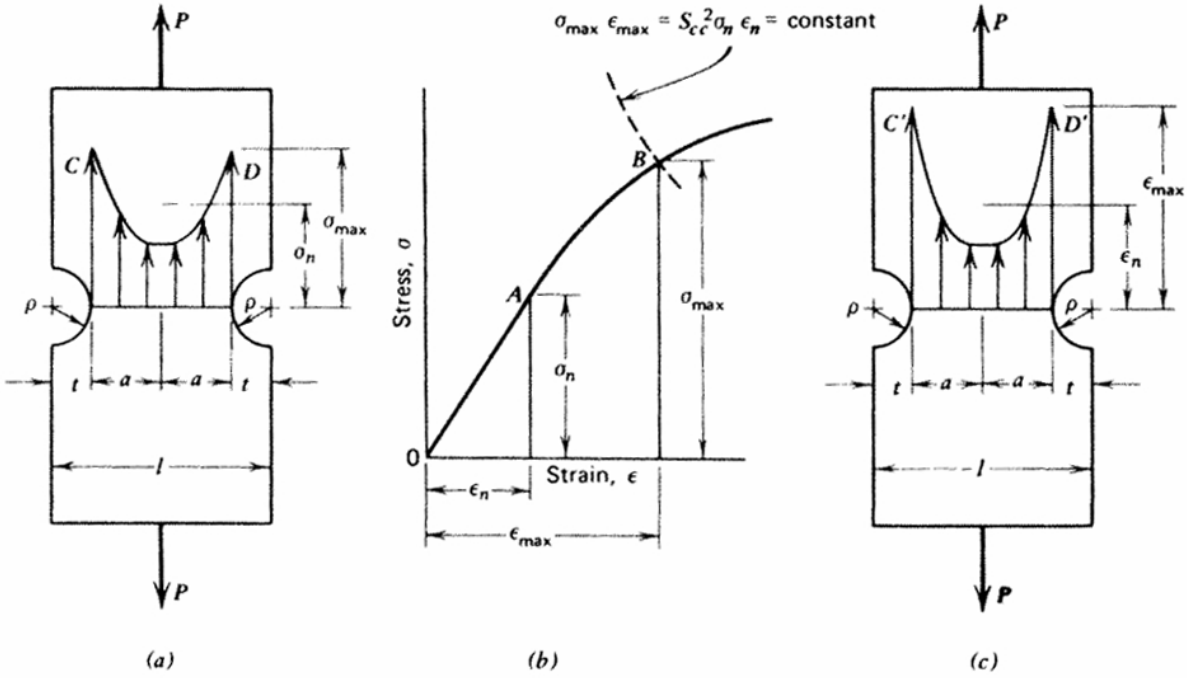

Figure 5.1: Neuber's inelastic stress concentration factor (a) Stress distribution (b) Stress-strain curve (c) Strain distribution, from "Advanced Mechanics of Materials" [16] page 599

Correspondingly, Neuber defined an effective strain concentration factor E_{ce} by the relation

$$E_{ce} = \frac{\varepsilon_{max}}{\varepsilon_{ne}} \tag{5.5}$$

where ε_{max} and ε_{ne} denote maximum effective strain and effective nominal strain, respectively. Note that (ε_{ne}, σ_{ne}) are the coordinates of point A and (ε_{max}, σ_{max}) of point B in Fig. 5.1(b) [16]. Taking the advantage of uniaxial loading, effective stress and strain values are related to axial stress and strain values, respectively. Hence, point A and B both sit on the stress-strain curve. According to Neuber's rule [16], S_{cc}, S_{ce} and E_{ce} are related by,

$$S_{cc}^2 = S_{ce}E_{ce} \tag{5.6}$$

i.e.

$$S_{cc}^2 = \frac{\sigma_{max}}{\sigma_{ne}}\frac{\varepsilon_{max}}{\varepsilon_{ne}} \tag{5.7}$$

These stress concentration factors are, for the most part, conservative estimates [98]. The theory has been widely applied to notches of different geometry on plates and cylinders to date. The beauty of the theory is to relate the stress concentration factor from the elastic range, which is easier to obtain, to the plastic range under arbitrary loading conditions.

In Neuber's book [78], he also introduced formulae of analytical elastic solutions of SCF for both deep and shallow defects under different loading conditions. Thereby, the calculation of SCF of specimens under combined loading conditions is obtained.

As an example, a plate with a notch in the middle under uniaxial loading is studied with $t = 3mm$, $b = 17mm$, $\rho = 18.167mm$ and $h = 100mm$ as shown in Fig. 5.2. Uniform tensile load P is applied at the middle of the far end cross section as shown in Fig. 5.2(a). This load P only stretches the plate elastically. Neuber derived the calculated elastic stress concentration factor S_{cc}

$$S_{cc} = 1 + \frac{(S_{cs}-1)(S_{cd}-1)}{\sqrt{(S_{cs}-1)^2 + (S_{cd}-1)^2}} \tag{5.8}$$

where S_{cs} and S_{cd} represent the elastic SCF for shallow and deep notch, respectively.

In general, the calculated SCF requires the combination of these two SCF's. In Neuber's book [78], he showed the S_{cs} and S_{cd} for notched specimens under different loading conditions. Additionally, Neuber applied loads at a distance of $\frac{b}{2}$ from the plate bottom for both S_{cs} and S_{cd} calculation. Therefore, to use Neuber's formulas on the plate under a load P as shown in Fig. 5.2(a), it is required to translate load P from the distant $\frac{t+b}{2}$ to $\frac{b}{2}$ (as shown in Fig. 5.2(b)). Such translation requires a statically equivalent moment $M = P\frac{t}{2}$ (as shown in Fig. 5.2(c)) added at the same cross section. This linear combination is valid for the elastic study.

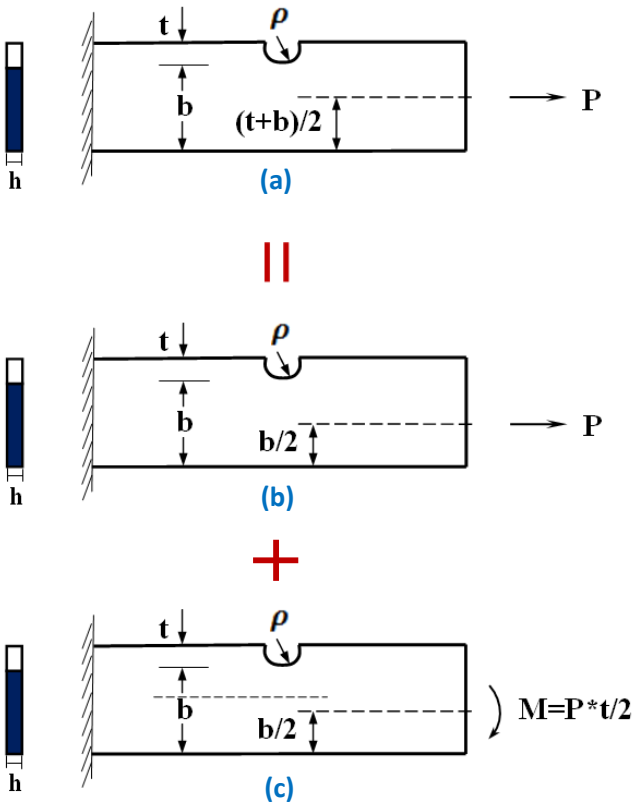

Figure 5.2: Applying Neuber's theory on notched specimen under uniaxial loading

For uniaxial tension as in Fig. 5.2(b), Neuber derived S_{cs} and S_{cd} as

$$S_{cs} = 1 + 2\sqrt{\frac{t}{\rho}} \tag{5.9}$$

$$S_{cd} = \frac{\eta_1 - 2c}{1 - \frac{c}{\sqrt{\frac{b}{\rho}+1}}} \tag{5.10}$$

where

$$\eta_1 = \frac{2(\frac{b}{\rho}+1)\sqrt{\frac{b}{\rho}}}{(\frac{b}{\rho}+1)(arctan\sqrt{\frac{b}{\rho}}) + \sqrt{\frac{b}{\rho}}} \tag{5.11}$$

$$c = \frac{\eta_1 - \sqrt{\frac{b}{\rho}+1}}{\frac{4}{3\eta_2}\sqrt{\frac{b}{\rho}+1} - 1} \tag{5.12}$$

η_2 in c is defined as

$$\eta_2 = \frac{4\frac{b}{\rho}\sqrt{\frac{b}{\rho}}}{3[\sqrt{\frac{b}{\rho}} + (\frac{b}{\rho}-1)(arctan\sqrt{\frac{b}{\rho}})]} \tag{5.13}$$

Note that η_1 represents the SCF of the double externally deep notched specimen under uniaxial tension; and η_2 represents the double externally deep notched specimen under pure bending.

For $t = 3mm$, $b = 17mm$ and $\rho = 18.167mm$, the calculated stress concentration factor for uniaxial tension corresponding to Fig. 5.2(b) is denoted $S_{cc,b}$ and $S_{cc,b} = 1.1387$.

For pure bending as in Fig. 5.2(c), S_{cs} and S_{cd} are

$$S_{cs} = 1 + 2\sqrt{\frac{t}{\rho}} \tag{5.14}$$

$$S_{cd} = \frac{2(\frac{b}{\rho}+1) - \eta_1\sqrt{\frac{b}{\rho}+1}}{\frac{4}{\eta_2}(\frac{b}{\rho}+1) - 3\eta_1} \tag{5.15}$$

where η_1 and η_2 are the same as defined in Eq. 5.11 and 5.13. For Fig. 5.2(c), the calculated stress concentration factor for bending moment is found to be $S_{cc,c} = 1.3073$.

Elastic deformation allows the linear combination of the above S_{cc} for uniaxial tension as shown in Fig. 5.2(b) and that for pure bending as shown in Fig. 5.2(c).

The maximum stress at the notch root for uniaxial tension in Fig. 5.2(b) is

$$\sigma_{max,b} = S_{cc,b} * \frac{P}{bh} \tag{5.16}$$

That for pure bending in Fig. 5.2(c) is

$$\sigma_{max,c} = S_{cc,c} * \frac{6M}{b^2 h} = S_{cc,c} * \frac{6\frac{Pt}{2}}{b^2 h} \tag{5.17}$$

The maximum stress at the notch root in Fig. 5.2(a) is thus

$$\sigma_{max} = \sigma_{max,b} + \sigma_{max,c} \tag{5.18}$$

and by definition, the final calculated stress concentration factor S_{cc} for constant load P applied at the middle of the far end cross section as shown in Fig. 5.2(a) is

$$S_{cc} = \frac{\sigma_{max}}{\frac{P}{bh}} \tag{5.19}$$

For this example, the final calculated stress concentration factor is $S_{cc} = 1.831$.

In the following FE analyses, the same model is studied with uniformly distributed tension applied at the far end cross section. The resulting stress concentration factor in FE analyses is found to be in favorable agreement with Neuber's theory.

5.2 FE Analysis Comparison with Neuber's Theory

As mentioned before, FE method has been widely used for the study of stress/strain concentration of notched bodies in plane stress or plane strain. Härkegård and Mann [39] applied the generalized Neuber's rule in large-scale yielding (LSY) condition formulated by [40] for tensile notched specimens. Härkegård and Mann used FE method to find the notch stress and strain in LSY condition and their results show good agreement with Neuber's rule. Sharpe and Wang [99] modified Neuber's relation and applied it on notch strain prediction. Finite element analysis was preformed for the calculation of elastic SCF calculation. The capacity of the modified

Neuber's relation is validated by comparing the formula predicted results to experimental test results. These studies show the success of using FE method in stress or strain concentration studies based on Neuber's rule. Thereby, in this section, the FE method is used to estimate stress concentration factors due to pit corrosion.

Before employing the FE method, the validation of this method is first carried out. The discussion of validation includes the meshing sensitivity analyses and the comparison to Neuber's theory.

5.2.1 Meshing Sensitivity Analysis

First, we carried out plastic FE analyses in ABAQUS [3] and studied a plane stress specimen, with the length $220mm$, width $100mm$, thickness $20mm$, notch depth $3mm$ and notch axial length $20mm$, as shown in Fig. 5.3. These geometries are consistent to those in the previous pitted plate analyses, except for the change from pit to notch. The model is assumed to be made of $A36$ steel. The power law definition $\sigma = K\varepsilon^n$ is applied for plastic deformation constitutive relations, with $n = 0.2$ and $K = 870MPa$. The yielding stress is $\sigma_Y = 250MPa$; the Young's modulus is $E = 200GPa$ and the Poisson's ratio is $\nu = 0.33$. Surface tractions are applied at both ends. Thus, the specimen is under uniaxial tension, the same as shown in Fig. 5.2(a).

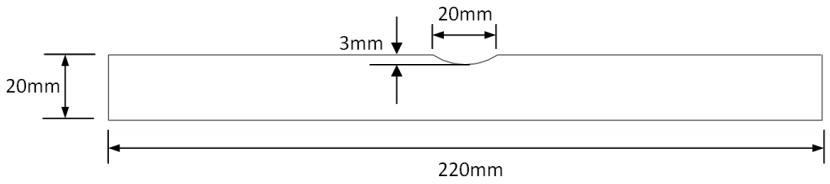

Figure 5.3: FE notch specimen

The initial FE analyses were conducted on a $3D$ model, as shown in Fig. 5.4(a). However, the $3D$ model was challenged by the meshing convergence and the CPU time, when the element size decreases from $0.8mm$ to $0.5mm$. Therefore, the decision

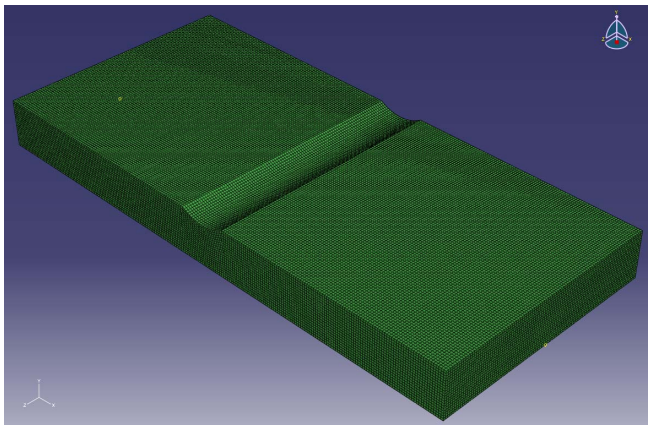

(a) 3D notch meshed model with element size 1mm

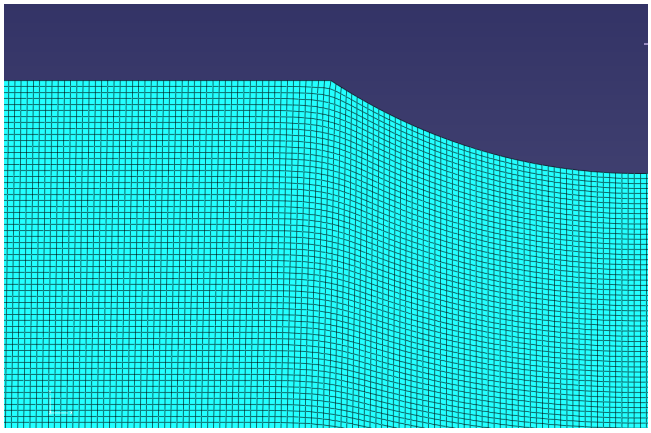

(b) 2D notch meshed model with element size 0.2mm

Figure 5.4: FE notch specimen

was made to switch to $2D$ model for the element size of $0.5mm$, $0.2mm$, $0.1mm$, and $0.05mm$, respectively. Such switch is based on the assumption that the plate can be regarded as a semi-infinite notched plate. Figure 5.5 shows the meshing sensitivity analyses results of both $3D$ and $2D$ models. The calculated stress concentration factor reaches convergence as the element size is smaller than $0.2mm$.

Roy [93] introduced a detailed procedure to "estimate the numerical errors that occur in computational simulation". He defined the discretization error in Eq. 5.20 as the difference between a numerical solution and the exact solution solved in the

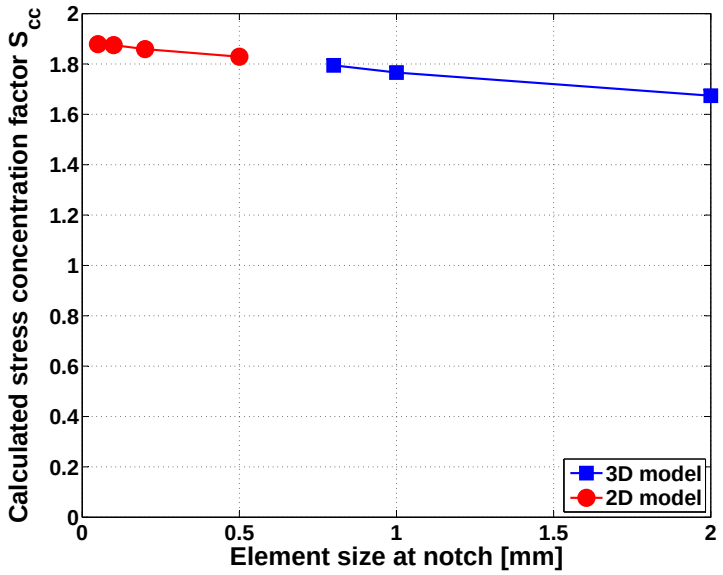

Figure 5.5: Meshing sensitivity analyses of both $3D$ and $2D$ models

continuum field.

$$DE_z = f_z - f_{exact} \tag{5.20}$$

where z refers to the mesh level. He applied the posteriori methods based on Richardson extrapolation to estimate the discretization error only after the numerical solution is computed. We, first, apply Roy's solution verification procedure to test our FE meshing sensitivity analyses results error.

For the meshing sensitivity analyses described above, we found three numerical solutions (calculated stress concentration factors) on different meshing refinement levels: on the element size of $z_1 = 0.05mm$, $z_2 = 0.1mm$ and $z_3 = 0.2mm$. The exact stress concentration factor is estimated by these three numerical solutions according to the posteriori method based on Richardson extrapolation as described by Roy [93]. For this case, a constant grid refinement factor r is obtained as

$$r = \frac{z_3}{z_2} = \frac{z_2}{z_1} = 2 \tag{5.21}$$

Details have been provided by Roy [93]. For this example, by defining r,

$$z_2 = rz_1 \tag{5.22}$$

and

$$z_3 = rz_2 = r^2 z_1 \tag{5.23}$$

The three discretization error equations introduced by Roy [93] for a p^{th}-order accurate solution are

$$f_1 = f_{exact} + g_p {z_1}^p + O({z_1}^{(p+1)}) \tag{5.24}$$

$$f_2 = f_{exact} + g_p (rz_1)^p + O([rz_1]^{(p+1)}) \tag{5.25}$$

$$f_3 = f_{exact} + g_p (r^2 z_1)^p + O([r^2 z_1]^{(p+1)}) \tag{5.26}$$

Neglecting higher order terms and solving these equations for p

$$p = \frac{ln(\frac{f_3 - f_2}{f_2 - f_1})}{ln(r)} \tag{5.27}$$

The estimated exact solution on the accurate order of p is

$$f_{exact} = f_1 + \frac{f_1 - f_2}{r^p - 1} \tag{5.28}$$

Values of f_i's are summarized in Table 5.1 for meshing sensitivity analyses results and the corresponding exact stress concentration factor is 1.879 by applying Eq. 5.28. The difference between this estimated exact stress concentration factor based on Roy's procedure and the analytical solution of Neuber (1.831, as calculated in Section 5.1) is only 2.55%. The good agreement between these two solutions shows the reliability of the results of FE meshing sensitivity analyses. For the specimen of the same geometry, the element size of $0.2mm$ is applied in the FE analyses, as shown in Fig. 5.4(b), because its SCF is close enough to the estimated SCF value.

Table 5.1: Meshing Sensitivity Analyses Results Verification

	h_1	h_2	h_3
Element size $[mm]$	0.05	0.1	0.2
	f_1	f_2	f_3
Stress concentration factor	1.879	1.875	1.859

5.2.2 The Comparison between FE Analyses and Neuber's Theory in Plasticity

As introduced in Section 5.1, Neuber's theory relates the SCF in the elastic range to that in the plastic range. When a specimen deforms plastically, its effective stress concentration factor is below the corresponding elastic SCF, while the effective strain concentration factor exceeds the elastic counterpart. Based on the meshing sensitivity study, the FE analyses results are compared to those predicted by Neuber's theory. Figure 5.6 presents the maximum axial stress at the notch root predicted by Neuber's inelastic formula and that by the FE analyses. In the maximum axial stress calculation, the stress concentration factor $S_{cc} = 1.831$ is used for both analytical and FE calculations. Very good agreement has been achieved, which indicates the accuracy of Neuber's approximation. With these studies and comparisons, FE analyses can be relied on for broader SCF estimation for other defect geometries whose analytical solution is not included in Neuber's book.

5.2.3 Elastic Stress Concentration Factor Calculation for an Semi-oblate Spheroidal Pit-corroded Plate

After intensive literature research, no literature was found regarding the analytical elastic stress concentration factor of the specimen with a shallow semi-oblate spheroidal pit on one side. As FE method has been tested and verified with success in Section 5.2.2, this method is thus employed for the elastic stress concentration factor estimation for a pitted plate.

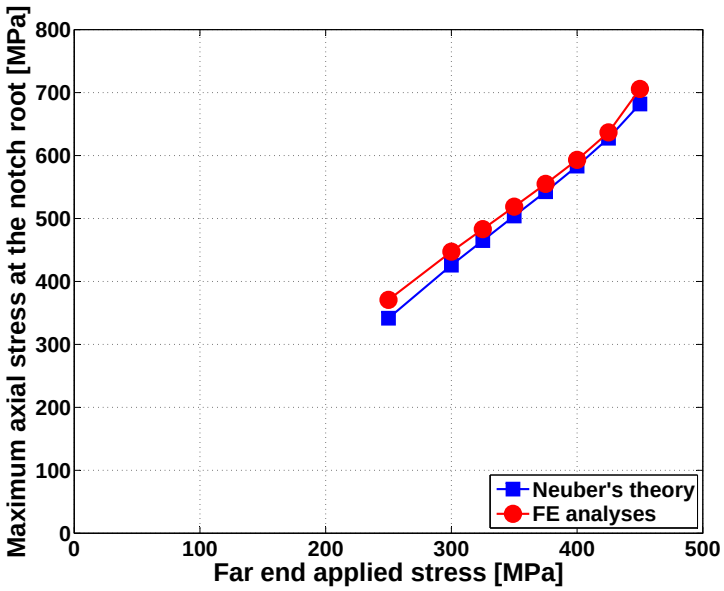

Figure 5.6: Maximum axial stress at the notch root predicted by analytical and FE methods

The geometries and the material properties of the pitted plate are identical to those introduced in Section 5.2.1. The diameter of the pit is $20mm$ and depth is $3mm$. Because of symmetry, only a quarter of the plate is modeled in ABAQUS [3]. A traction is applied at the far end and the elastic stress concentration factor is calculated based on Neuber's definition. Refined meshing is performed at the area close to the center pit. Table 5.2 presents the meshing sensitivity analyses results. Solution verification procedure (Eq 5.28) is then employed and the calculation shows that the estimated SCF based on the meshing sensitivity study for a centered pitting plate is $f_{exact} = 1.550$. The ratio of SCF of the semi-oblate spheroidal pit in the example above to that of a shallow notched plate of the same depth and on-surface radius in the example in Section 5.1 is

$$\zeta = \frac{1.550}{1.879} = 0.825 \tag{5.29}$$

Thus, we find an approximate analytical solution for the elastic stress concentra-

tion factor for a shallow semi-oblate spheroidal pit by assuming their ratio remains constant for arbitrary ratios of $\frac{t}{\rho}$.

$$S_p = \zeta * (1 + 2\sqrt{\frac{t}{\rho}}) \tag{5.30}$$

Table 5.2: Meshing Sensitivity Analyses of pit-corroded Model

Element size $[mm]$	0.2	0.3	0.5
Stress concentration factor	1.542	1.538	1.530

5.3 Reliability analyses

In the following reliability analysis of ship hull damage in grounding, this SCF will be applied to quantify the ship hull strength reduction due to pit corrosion.

5.3.1 Probabilistic Analysis with One Random Variable

In the above analyses and comparisons, the notch geometry is defined as a fixed value. In real cases, however, notch length or depth are random variables. Therefore, a probabilistic analysis is needed for the maximum stress/strain prediction due to such geometrical defects.

Presumably knowing the analytical formula for the stress concentration factor, the probabilistic analysis is able to relate the randomness of the defect geometries to that of the stress concentration factor. We need to obtain the probabilistic properties of the stress concentration factor to know probabilistic properties of the maximum stress/strain, which directly leads to the fracture of structures.

Consistent with the previous denotation, ρ, the notch radius, is defined as a random variable. We assume ρ follows the lognormal distribution. The lognormal distribution is closely tied to normal distribution [4]. If X follows the lognormal distribution, then $log(X)$ follows the normal distribution. The normal distribution

is usually denoted by $N(\mu, \sigma)$; the corresponding two-parameter (2-piece) lognormal distribution is usually denoted by $\wedge(\mu, \sigma)$. μ and σ are mean and standard deviation of normal distributed variable, respectively. The probabilistic density function of X having $\wedge(\mu, \sigma)$ is

$$f(x) = \frac{1}{\sqrt{2\pi}\sigma x} exp\{-\frac{(log(x) - \mu)^2}{2\sigma^2}\} \tag{5.31}$$

The range of X is $0 < X < \infty$.

Furthermore, as introduced in many references, for example [4, 24], a random variable X which can take any value exceeding a fixed value τ, is said to be lognormally distributed with three parameters τ, μ and σ if $Y = log(X - \tau)$ follows $N(\mu, \sigma)$. This three-parameter (3-piece) lognormal distribution is denoted by $\wedge(\tau, \mu, \sigma)$. The parameter τ is called the threshold parameter. In this case, the range of X is $\tau < X < \infty$ [4]. More details of three-piece lognormal distribution can be referred to some fundamental textbooks, for example [4]. The lognormal distribution sometimes is preferable as it automatically avoids negative values of the random variable. Additionally, when exact distribution information is not known as a priori, normal or lognormal distributions can be assumed [12]. These are reasons we assume the radius of curvature at notch root ρ follows the lognormal distribution.

The probability density function (pdf) of ρ is then

$$f_\rho = \frac{1}{\sqrt{2\pi}\sigma\rho} exp\{-\frac{(ln(\rho) - \mu)^2}{2\sigma^2}\} \tag{5.32}$$

The previous section showed that for a shallow notch, Neuber's prediction (Eq.5.9) of elastic SCF is

$$S = 1 + 2\sqrt{\frac{t}{\rho}} \tag{5.33}$$

By knowing this relation between S and ρ, we derived the pdf of S as follows

$$f_s = \frac{1}{\sqrt{2\pi}\sigma(s-1)} exp\{-\frac{ln[4t(s-1)^{-2}] - \mu^2}{2\sigma^2}\} \tag{5.34}$$

The fracture failure probability of a notched structure under a fixed (deterministic) uniaxial loading thus can be determined by Eq. 5.35

$$P_f = P(S * \sigma \geq F) = 1 - P(S < \frac{F}{\sigma}) = 1 - \int_0^{\frac{F}{\sigma}} f_s(t)dt \tag{5.35}$$

where, F denotes the structural fracture strength.

For example, considering the mean value for ρ is assumed $18.167mm$ and the standard deviation is $5mm$. This mean value is consistent to the deterministic calculation in Section 5.1 and 5.2. These probabilistic properties of ρ are defined so that the notch geometry falls into the shallow category. Consistent with Section 5.1, the notch depth of $t = 3mm$ is used (see Fig. 5.2).

Matlab [64] and Minitab [67] packages were also employed to run MC simulations for S. The distribution fitting is performed on the simulated S. The repeated number of sampling ρ in these packages is $N = 100,000$. Results show that among widely applied distributions, generalized extreme value (GEV) and three-piece lognormal distribution fit the simulated S the best as presented in Fig. 5.7(a). The estimated τ for the three-piece lognormal is 0.996. Figure 5.7(b) presents the comparison between distribution fittings and analytical derived pdf of S (Eq. 5.34). In Fig. 5.7(b), both GEV and three-piece lognormal distribution fit the actual pdf with success. Comparing the peak values, three-piece lognormal fits even better. This should not be surprising as the analytical pdf formula of S is in a log form. The exciting outcome of the comparison shows the these methods are capable to predict the undetermined stress concentration factor induced by random structure geometrical defects.

5.3.2 Level 3 Reliability Analysis Based on Fully Probabilistic Method

The nomenclature used here is that used by Mansour [63]. Level 3 reliability study uses the direct integration of the joint probability density function $f_{\overline{X}}$ (pdf)

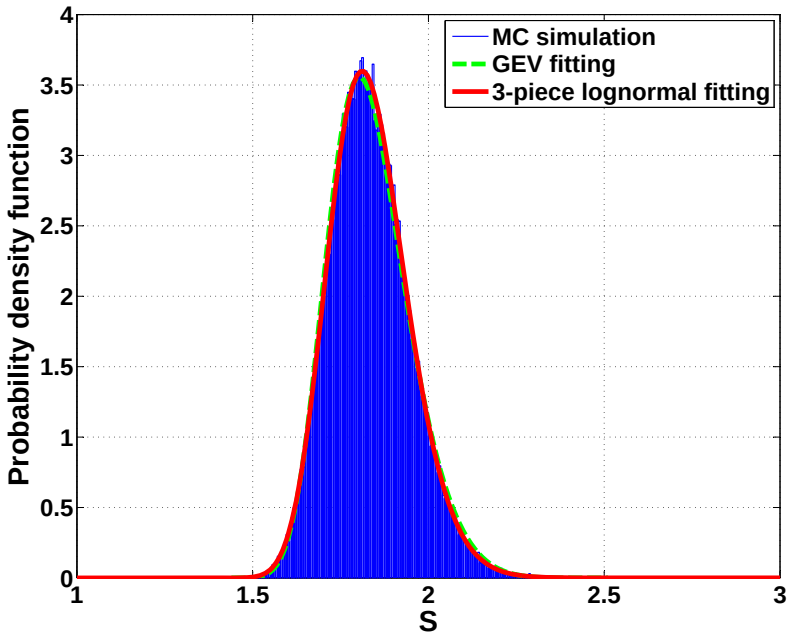

(a) Comparison between MC simulation and distribution fitting

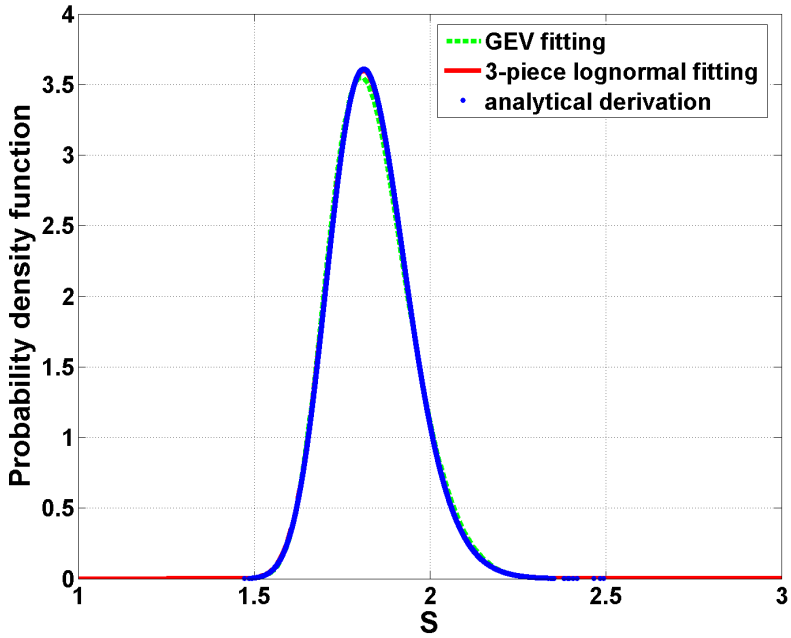

(b) Comparison between analytical derivation and distribution fitting

Figure 5.7: Probability density function comparison between analytical derivation and distribution fitting

of the random variables, x_i, used to define the limit state. As shown in [63], the probability of failure is given by,

$$P_f = \int \cdots \int f_{\overline{X}}(x_1, x_2, \cdots, x_n) dx_1 dx_2 \cdots dx_n \tag{5.36}$$

The limit state function, $g(x_1, x_2, \cdots, x_n)$ defines the failure state of the structure. The unsafe region is

$$g(x_1, x_2, \cdots, x_n) \leqslant 0 \tag{5.37}$$

Note that the limit state function is often a simplified mathematical expression of the actual failure state [12]. The most widely used limit state function for engineering application is in the load resistance format. For a notched plate under uniform tension, the limit state function is,

$$F - (1 + 2\sqrt{\frac{t}{\rho}})\sigma_n = 0 \tag{5.38}$$

where F is denoted the fracture strength and σ_n is the nominal stress at the notch cross section. The nominal stress σ_n is able to be related to the stress applied at the far end by knowing the plate geometry change.

Rewriting Eq. 5.38, we find

$$M = g(\rho, \sigma_n) = \frac{F}{(1 + 2\sqrt{\frac{t}{\rho}})} - \sigma_n = 0 \tag{5.39}$$

Equation 5.39 presents the limit state in a convenient way as the first term is the strength term, where the defect deterioration effect is taken into account by the stress concentration factor term. The second term is the loading term. M is thus simply the difference between the structural capacity and the applied load. When failure occurs, the probability of failure is thus able to be simply described as

$$P_f = P[g \leqslant 0] = P[\frac{F}{(1 + 2\sqrt{\frac{t}{\rho}})} \leqslant \sigma_n] \tag{5.40}$$

In Eq. 5.40, two random variables are ρ as defined in Section 5.3.1 and σ_n. ρ consistently follows lognormal distribution, i.e. $\rho \sim \wedge(\mu_1, \sigma_1)$. For ship hull structures, Parunov and Soares [86] suggested a gaussian distribution as the stochastic model for still water bending moment. The applied uniform tensile stress in my model is considered as a result of such random still water bending moment. As the stress only takes the positive value here, a lognormal distribution is thus assumed for σ_n, i.e. $\sigma_n \sim \wedge(\mu_2, \sigma_2)$. As ρ and σ_n are assumed to be statistically independent, the joint pdf of them equals the product of marginal pdf of each individual variable. Therefore, the above failure probability (Eq. 5.40) is able to be evaluated for the limit state given by Eq. 5.39, as shown in Eq. 5.41.

$$
\begin{aligned}
P_f &= P[g \leqslant 0] \\
&= P[\frac{F}{(1+2\sqrt{\frac{t}{\rho}})} \leqslant \sigma_n] \\
&= 1 - P[\sigma_n < \frac{F}{(1+2\sqrt{\frac{t}{\rho}})}] \\
&= \int_0^{\infty} \int_0^{\frac{F}{(1+2\sqrt{\frac{t}{\rho}})}} f_{\rho,\sigma_n}(\rho, \sigma_n) d\sigma_n d\rho \\
&= \int_0^{\infty} \int_0^{\frac{F}{(1+2\sqrt{\frac{t}{\rho}})}} f_{\rho}(\rho) * f_{\sigma_n}(\sigma_n) d\sigma_n d\rho \\
&= \int_0^{\infty} \frac{1}{\rho\sqrt{2\pi}\sigma_1} exp - \frac{(ln(\rho) - \mu_1)^2}{2{\sigma_1}^2} [\int_0^{\frac{F}{(1+2\sqrt{\frac{t}{\rho}})}} \frac{1}{\sigma_n\sqrt{2\pi}\sigma_2} exp - \frac{(ln(\sigma_n) - \mu_2)^2}{2{\sigma_2}^2} d\sigma_n] d\rho
\end{aligned}
\tag{5.41}
$$

By substituting numbers as listed in Table 5.3 for coefficients in Eq. 5.41, the Level 3 reliability is calculated numerically using Matlab [64]. The failure probability of the notched plate with the strength $250MPa$ under a random nominal stress (mean value $75MPa$ and standard deviation $20MPa$) is 0.0094. Based on the conventional safety factor definition, the safety factor for this problem is $SF = \frac{F}{(1+2\sqrt{\frac{t}{\mu_\rho}}) * \mu_{sigma_n}}$.

Plugging the mean value of ρ, the corresponding SCF is identical to what we found in the deterministic study in Section 5.1: 1.831. The conventional safety factor for this pitted plate is $SF = \frac{250}{1.831*75} = 1.82$. Partial safety factor for individual random variable based on Level 1 reliability analysis will be discussed later.

Table 5.3: Coefficients for the Level 3 Failure Probability calculation

μ_ρ[mm]	σ_ρ[mm]	μ_{σ_n}[MPa]	σ_{σ_n}[MPa]	F[MPa]	t $[mm]$
18.167	5	75	20	250	3

5.3.3 Level 2 Reliability Analysis

Because of the difficulties in obtaining the joint pdf of the variables and in obtaining solutions of the integrals, Level 3 reliability analysis is often not practical. Hence, Level 2 reliability analysis is introduced. Level 2 connects the failure probability to a reliability index, which is called a "safety index". The approximate probability of failure can be directly obtained if this index is determined [63].

The method used in Level 2 as well as the following Level 1 reliability analysis is named "first-order reliability method (FORM)". A brief introduction of this method is presented with the safety index concept. More details of this method can be found in Thoft-Christensen and Baker [109].

5.3.3.1 First-order reliability method (FORM)

The limit state function is defined in Eq. 5.42, which is the same as in the Level 3 reliability analysis in Section 5.3.2. We have, similar to Eq. 5.39, generally:

$$M = g(x_1, x_2, \cdots, x_n) \tag{5.42}$$

Retaining only the first order terms of a Tayler series expansion of the limit state function:

$$M = g(x_1, x_2, \cdots, x_n) \simeq g(x_1^*, x_2^*, \cdots, x_n^*) + \sum_i (x_i - x_i^*)(\frac{\partial g}{\partial x_i})|_{x_i^*} \tag{5.43}$$

where x_i^* is the linearization point and also called a "checking point". The function M is thus approximately evaluated at x_i^*. The point x_i^* is usually the mean value.

The mean and standard deviation of M are approximated by Eq. 5.44 and 5.45 by neglecting higher order terms in Eq. 5.43, which can be referred to [63, 109]

$$\mu_M \simeq g(\overline{x_1}, \overline{x_2}, \cdots, \overline{x_n}) \tag{5.44}$$

$$\sigma_M \simeq \sqrt{\sum_i \sum_j (\frac{\partial g}{\partial x_i})|_{\overline{x_i}} * (\frac{\partial g}{\partial x_j})|_{\overline{x_j}} * \varrho_{x_i,x_j} * \sigma_{x_i} * \sigma_{x_j}} \tag{5.45}$$

where ϱ_{x_i,x_j} is the correlation coefficient of x_i and x_j.

To better understand the safety index in Level 2 reliability analysis, a simple example is first followed as discussed by [63, 109]. The limit function of the example is simply defined as

$$M = S - L \tag{5.46}$$

where S is the strength (resistance) of a structure and L is the applied loading. S and L are assumed to be independent and both follow normal distribution, with the mean μ_S and μ_L and standard deviation σ_S and σ_L, respectively. As this limit state function itself is a first order linear function, no Tayler's expansion is needed. The mean and standard deviation of M is easily to be found,

$$\mu_M = \mu_S - \mu_L \tag{5.47}$$

$$\sigma_M = \sqrt{\sigma_S^2 + \sigma_L^2} \tag{5.48}$$

Because M also follows the normal distribution, the failure probability P_f is

$$P_f = P(M \leq 0) = U_M(0) \tag{5.49}$$

where U_M denotes the cumulative distribution function of M. The standard form of M can be written as $T = \frac{M-\mu_M}{\sigma_M}$ so that T follows the standard normal distribution. Therefore the failure probability is

$$P_f = P(M \leq 0) = U_M(0) = \Phi_T(\frac{-\mu_M}{\sigma_M}) = \Phi_T(-\beta) \tag{5.50}$$

where Φ_T is the cumulative distribution function of standard normal distribution. "β" is defined as the safety index. It is a measure of safety, which is associated to the failure probability. β is defined as the ratio of μ_M to σ_M

$$\beta = \frac{\mu_M}{\sigma_M} \tag{5.51}$$

For the case of normal variables and linear state function, the safety index takes the form of

$$\beta = \frac{\mu_M}{\sigma_M} = \frac{\mu_S - \mu_L}{\sqrt{\sigma_S^2 + \sigma_L^2}} \tag{5.52}$$

In this way, the failure probability is related to β. In another words, β is associated with the safety (or failure) margin under a limit state. In this example, β is in an explicit expression. However, this may be not the case for other problems with complex limit state functions, where iterative computation is needed for β.

Continuing this example, if we normalized S and L as $S' = \frac{S-\mu_S}{\sigma_S}$ and $L' = \frac{L-\mu_L}{\sigma_L}$, the limit state function $M = 0$ can be rewritten in the normalized space as

$$M = \sigma_S S' - \sigma_L L' + \mu_S - \mu_L = 0 \tag{5.53}$$

which is a straight line shown in Fig. 5.8.

This straight line separates the space into two regions: a failure region ($M < 0$) and a safe region ($M > 0$). The shortest distance D from the origin to the line is calculated from the simple geometry.

$$D = \frac{\mu_\beta}{\sigma_\beta} = \frac{\mu_S - \mu_L}{\sqrt{\sigma_S^2 + \sigma_L^2}} \tag{5.54}$$

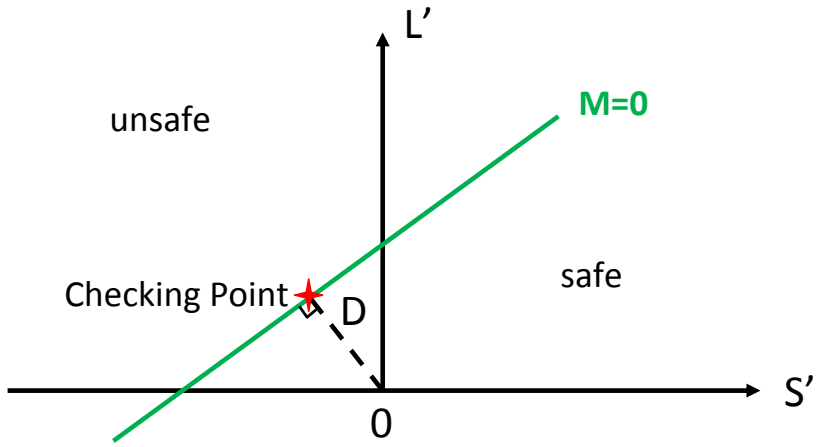

Figure 5.8: Limit state function in the space of normalized variables for a simple example, from [63]

In the figure, the distance is a measure of safety or reliability. Note that this distance D is exactly equal to the safety index β, as shown in Eq. 5.52. So, the fundamental geometrical interpretation of a safety index is the shortest distance from the origin to a surface, which is defined by the limit function equal to zero. Thus, the corresponding checking point x_i^* represents the most likely failure point.

The derivation of how the safety index β is related to the failure probability is described in [63] and is

"based on the following assumptions/limitations:

- The limit state function is linearized at the mean value. Higher order terms are neglected.
- β is dependent on how the limit state function is formulated. For example, if the limit state function is defined as $M = S^2 - L^3$, from Eq. 5.52, β is not the same as that for the example with $M = S - L$. However, limit state definitions follow the same mechanical failure formulation, i.e. $M = strength - loading$.
- All random variables follow normal distribution." [63]

These assumptions are easily violated. For example, for ship hull ultimate collapse reliability analysis, the water wave bending moment follows a Weibull distribution but not normal distribution [63]. The limit state function is a nonlinear equation involving ship hull bending moment capacity, still water bending moment, wave bending moment and influence factors among each other as random variables. The safety index calculation only based on their mean values may be inaccurate as higher order terms are neglected. Thus, the following procedure is introduced to avoid the first two limitations.

5.3.3.2 The Hasofer/Lind Transformation

Hasofer/Lind [43] developed a procedure in which the limit state function is still interpreted as a failure surface and the failure probability is associated with the point on the surface and of the shortest distance to the origin.

As is commonly done, the random variables are normalized using the relations:

$$y_i = \frac{x_i - \mu_i}{\sigma_i} \tag{5.55}$$

where μ_i and σ_i are respectively the mean and the standard deviation of x_i. Further details can be found in Ang and Tang [7]. The limit state function is then transferred from the original space to the normalized space, as defined in Eq. 5.56.

$$G(y_1^*, y_2^*, \cdots, y_n^*) = 0 \tag{5.56}$$

The variables y_i^* define the point closest to the origin in the normalized space.

The safety index β is defined as the shortest distance from the origin to the failure surface in the normalized space. The safety index and the corresponding point coordinates y_i^* are calculated by iteratively solving the following set of equations.

$$G(y_1^*, y_2^*, \cdots, y_n^*) = 0 \tag{5.57}$$

$$y_i^* = -\alpha_i^* \beta \tag{5.58}$$

$$\alpha_i^* = \frac{(\frac{\partial G}{\partial y_i})|_{y_i^*}}{\sqrt{\sum_i (\frac{\partial G}{\partial y_i})^2|_{y_i^*}}} \tag{5.59}$$

where α_i^* is "the direction cosines at the most likely failure point" [63]. Back to the original space, the most likely failure point corresponding to y_i^* is

$$x_i^* = \mu_i + \sigma_i y_i^* = \mu_i - \sigma_i \alpha_i^* \beta \tag{5.60}$$

This procedure yields the same result as the FORM method for a linear limit state function, see page 130 in [63] and page 110 in [66].

5.3.3.3 Non-normal Distribution

If random variables x_i do not follow normal distributions as assumed in equations 5.57 to 5.59. A procedure of distribution transformation is needed.

Rachwitz and Fiesler suggested that "most of the contribution to the probability of failure comes from the tail of the distribution" [90]. The non-normal distribution is approximated as a normal distribution by equating the cumulative (c.d.f) and probability density functions of the actual distribution to the normal distribution at the linearization point x_i^*. Mathematically then,

$$F_x(x^*) = \Phi(\frac{x^* - \mu'}{\sigma'}) \tag{5.61}$$

$$f_x(x^*) = \frac{1}{\sqrt{2\pi}\sigma'} exp[-\frac{(x^* - \mu')^2}{2\sigma'^2}] = \frac{1}{\sigma'} \varphi\{\Phi^{-1}[F_x(x^*)]\} \tag{5.62}$$

where $\Phi(\bullet)$ and $\varphi(\bullet)$ are standard normal cdf and pdf, respectively. Mansour [63] solved equations 5.61 and 5.62 for μ' and σ'.

$$\sigma' = \frac{\varphi\{\Phi^{-1}[F_x(x^*)]\}}{f_x(x^*)} \tag{5.63}$$

$$\mu' = x^* - \Phi^{-1}[F_x(x^*)]\sigma' \tag{5.64}$$

This procedure can become "more inaccurate if the original distributions are increasingly skewed" [10, 11]. This approximation is valid only at the most likely failure points x_i^* for determining the reliability safety index.

5.3.4 Level 1 Reliability Analysis

Level 2 reliability analysis focuses on the development of the safety index. However, in the limit state function, there are more than one random variable. Each has different levels of uncertainties which may affect the safety index or may be affected by the safety index to different degrees. These safety factors are applied to the corresponding random variables, with the name "partial safety factors" [63].

The partial safety factor (psf) is usually applied to the corresponding basic design value. For example, civil engineers need safety factors to apply to the yield strength or to the loads in the design or testing process. These partial safety factors calculation are based on Level 2 reliability analysis. Compared to Level 2, Level 1 reliability analysis is more practical to engineers. Usually reliability engineers take the mean value as the basic design values and thus, the limit state function may be rewritten as

$$g(\Delta_1\mu_1, \Delta_2\mu_2, \cdots, \Delta_n\mu_n) = 0 \tag{5.65}$$

where Δ_i is psf. The most likely failure point is then

$$x_i^* = \Delta_i\mu_i \tag{5.66}$$

Either by definition or by the transformation, original random variables are also normalized by the mean and standard deviation as in the Level 2 reliability analysis. By comparing Eq. 5.66 to equations 5.55 and 5.58, we are able to write

$$x_i^* = \mu_i - \alpha_i^*\beta\sigma_i = \mu_i(1 - \alpha_i^*\beta v_i) \tag{5.67}$$

where v_i is the coefficient of variance of x_i^*. Then from Eq. 5.66 and 5.67

$$\Delta_i = (1 - \alpha_i^* \beta v_i) \tag{5.68}$$

For nonlinear limit state functions, the determination of partial safety factors and the reliability safety index needs an iterative computation by applying equations 5.57, 5.58 and 5.59. The detailed iterative procedure is described by Mansour [63]. The probability of failure is calculated by Eq. 5.69.

$$P_f = \Phi(-\beta) \tag{5.69}$$

The same example as described in Section 5.3.2 is studied here using Level 1 reliability study. The notched plate is $220mm$ in length, $100mm$ in width and $20mm$ in thickness. The radius of the curvature at notch root and the nominal stress on the cross section where the notch is are two random variables. Both of them follow lognormal distributions. Their means and standard deviations are referred to Table 5.3. The limit state function is defined as in Eq. 5.39. The strength of the plate is reduced because of the notch; the nominal stress σ_n is able to be related to the stress applied at the far end by knowing the plate geometry change.

The partial safety factors of ρ and σ_n are denoted as Δ_ρ and Δ_{σ_n}, respectively. First the equivalent normal variables of both ρ and σ_n are found by applying the distribution transformation as described in Section 5.3.3.3. Then the iteration computation is performed on equations 5.57, 5.58 and 5.59 till convergence is achieved between the assumed ρ^* and σ_n^* and the calculated correspondents. Iteration stops when convergence is achieved. The threshold is 0.05 for the convergence of ρ^* and σ_n^*. Results are shown in Table 5.4.

In Table 5.4, β is the reliability safety index. The most likely failure points ρ^* and σ_n^* are calculated by multiplying the psf to the representative mean value. Comparing

Table 5.4: Level 1 reliability calculation results

β	P_f	ρ^* $[mm]$	Δ_ρ	σ_n^* $[MPa]$	Δ_{σ_n}
2.3578	0.0092	15.1	0.83	132.1	1.76

the failure probability to Level 3 full probabilistic calculation, the difference is about 2.1%. The difference mainly lies in the distribution transformation from lognormal to normal distribution. In this example, both safety index and partial safety factors are calculated simultaneously. The reliability safety index is dependent on individual partial safety factor; or in another word, partial safety factor can be viewed as discrete safety index for each random variable. Compared to Level 3 study, the safety factor of each individual variable is calculated. From these partial safety factors, how each random variable effects the structure failure is indicated. It is common sense that the plate is more likely to fail when notch is deep and the applied load is large. Then how deep of the notch and how large of the load are shown by the corresponding partial safety factors. If this example were a real problem, the provided partial safety factors will benefit engineers on design or test, as the product of psf and the mean value gives an estimation of critical design or test variables for a certain overall safety index.

5.4 Reliability Analysis of Double-hull Oil Tanker Bottom Shell Damage in Ship Grounding

The purpose of this example is to present an analysis of how pit corrosion affects a bottom shell's reliability level in large deformation in ship grounding. This example is motivated by oil spill when tankers ground on a relatively flat seabed. Bottom shells can be torn during ship grounding. However, depending on the penetration depth, denting alone or denting plus fracture may be produced [70]. In the example,

only denting is produced; but with the presence of corrosion, the maximum strain at the pit center of the bottom shell may exceed the fracture strain even though the nominal strain at the pit cross section is lower than the fracture strain. In this case, fracture may not be directly caused by grounding, but the amplified strain level due to corrosion may lead to fracture failure. As a result of the randomness of pit geometry and the nominal strain, the reliability of such a dented shell is evaluated based on the Level 1 calculation. Two random variables relating to plate strength and load are defined; and the partial safety factors of of these two variables will be calculated.

The double-hull oil tanker is considered to be a very large crude oil carrier (VLCC). It was considered in the study of bottom structure resistance in grounding by Zhang [124]. The ship and bottom shell dimensions are presented in Table 5.5. Figure 5.9 shows the grounding scenario. In grounding, the bottom shell is indented by seabed rock and is under large deformation. This large deformation may be far beyond the order of shell thickness and is comparable in size to the dimension of the struck panel. As detailed in Chapter 2, in the sufficiently large out-of-plane deformation, it is the membrane stress that dominates the dented bottom shell and compared to which the bending stress is negligible. Different from the problem in Chapter 2, the shell deformation is in the plastic regime and not restricted to the elastic regime. For such large deformation, strain level is very critical for fracture failure. This strain level is reduced when corrosion occurs on the bottom shell as we presented in Chapter 3. The scenario in this example is that a corroded bottom shell panel is under large plastic deformation under uniaxial tension induced by membrane stress in grounding.

To relate the maximum strain and the nominal strain of the bottom shell, Neuber's

Table 5.5: Dimensions of a double-hull oil tanker and its bottom parameters, from "Plate Tearing and Bottom Damage in Ship Grounding" [124]

Name	Data
Ship length, $L_{pp}[m]$	320.0
Breadth, $B[m]$	58.0
Depth, $D[m]$	31.25
Design draught, $T[m]$	22.3
Displacement, $[ton]$	$303,655$
Design speed, $[knot]$	15.0
Inner bottom thickness, $[mm]$	19.5
Inner bottom longitudinal size, $[mm]$	$600 \times 15 + 180 \times 25$
Inner bottom spacing of longitudinales, $[mm]$	915
Outer bottom thickness, $[mm]$	23.5
Outer bottom longitudinal size, $[mm]$	$580 \times 11.5 + 180 \times 25$
Outer bottom spacing of longitudinales, $[mm]$	915
Double bottom height, $[m]$	3.0

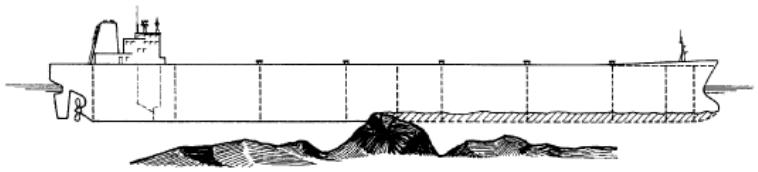

Figure 5.9: Denting in ship grounding, from "Plate tearing and bottom damage in ship grounding" [124]

inelastic formula is employed again,

$$S_{cc}^2 = \frac{\sigma_{max}}{\sigma_{ne}} \frac{\varepsilon_{max}}{\varepsilon_{ne}} \tag{5.70}$$

where σ_{ne} and ε_{ne} represent effective stress and strain on the cross section at the pit corrosion; σ_{max} and ε_{max} are maximum effective stress and strain at the center of the pit corrosion. The power law definition for material is still assumed as $\sigma = K\varepsilon^{n_0}$.

Substituting σ_{max} and σ_{ne} in Eq. 5.70

$$S_{cc}^2 = \frac{(K\varepsilon_{max}^{n_0})}{(K\varepsilon_{ne}^{n_0})}\frac{\varepsilon_{max}}{\varepsilon_{ne}} \tag{5.71}$$

For a shallow pit elastic stress concentration factor, as discussed in Section 5.2.3 it is approximated by that of the shallow notch multiplied by a factor, which is calculated in the FE analysis. Therefore, S_{cc} is assumed, as per Section 5.2.3, in the form of

$$S_p = \zeta * (1 + 2\sqrt{\frac{t}{\rho}}) \tag{5.72}$$

In Eq. 5.72, the radius of the curvature at the pit center and the pit depth affect the stress concentration factor.

In the analysis of corrosion on ship hull plates, it is a common practice to employ a pit geometry parameter to describe the pit geometry. The parameter is defined as a radius to depth ratio, i.e. $\frac{r}{t}$. The radius is the pit radius on the top surface of the plate. By denoting η as the pit geometry parameter and $\eta = \frac{r}{t}$, Eq. 5.72 is rewritten as

$$S_p = \zeta * (1 + 2\sqrt{\frac{2}{1+\eta^2}}) \tag{5.73}$$

Then, the maximum strain at the pit center by substituting the pit stress concentration factor is

$$\varepsilon_{max} = \varepsilon_{ne}[\zeta(1 + 2\sqrt{\frac{2}{1+\eta^2}})]^{\frac{2}{n_0+1}} \tag{5.74}$$

In this example, even though only denting is assumed to occur in the grounding, the maximum strain of dented bottom panel may still exceed the fracture strain as a result of pit corrosion. Therefore, the limit state function of this bottom shell panel is

$$M = \varepsilon_f - \varepsilon_{max} = \varepsilon_f - \varepsilon_{ne}[\zeta(1 + 2\sqrt{\frac{2}{1+\eta^2}})]^{\frac{2}{n_0+1}} \tag{5.75}$$

In Eq. 5.75, the nominal effective strain ε_{ne} and the pit geometry parameter η are random variables and assumed to follow lognormal distributions.

Nakai and Yamamoto [75] did intensive research on the effect of pit corrosion occurring to bulk carriers and oil tanker. They measured the pit corrosion geometry on both types of ships and found that the ratio of radius to depth is between 2 to 5. Based on what they found, the mean value of η is 3.5 and the standard deviated is assumed 1.0. In Section 5.2.3, the pit radius to depth is equal to 3.3, which is close to the mean value of η. Hence, $\zeta = 0.825$ is applied in Eq. 5.75 to approximate the difference between pit and notch induced stress concentration.

For ε_{ne}, no closely related data were found from literature regarding its value. The Naval Surface Warfare Center (NSWC), USA, performed four large-scale grounding tests to simulate grounding of an assembled ship bottom structure on a pinnacle rock at a scale of $1:5$ [104]. One test is on a conventional double-bottom model, which corresponds to an oil tanker of about $30,000$ and $40,000$ DWT. The measured energy absorbed during the test till the model is torn is $3.25MJ$. The absorbed energy is proportional to the deformed volume of the material, which is $0.245m^3$. The average effective strain is able to be calculated by

$$E = \sigma_0 \bar{\varepsilon} R_T \tag{5.76}$$

where E is the measured energy; R_T is the deformed material volume; σ_0 is the flow stress, which is $314MPa$ for the test material; and $\bar{\varepsilon}$ is the average effective strain level. By Eq. 5.76, the average effective plastic strain is 0.042. This effective strain provides an average strain level when fracture occurs in the whole deformed model in ship grounding, which may represent a nominal strain level for plate indentation. Hence, we assume the mean value of the nominal strain for an indented plate is 0.042. The standard deviation of ε_{ne} is 0.01, which represents a moderate variation. The

failure strain is assumed $\varepsilon_f = 0.2$.

The pit geometry parameter η and the nominal strain are assumed statistically independent. Level 1 reliability as described in Section 5.3.4 is conducted. The iterative procedures are applied. Table 5.6 summarizes the reliability safety index of this bottom shell panel, the failure probability, the most likely failure point of the nominal strain and the pit geometry parameter and the corresponding partial safety factors, respectively.

Table 5.6: Level 1 reliability calculation for an oil tanker dented bottom shell in ship grounding

β	P_f	ε_{ne}^*	$\Delta_{\varepsilon_{ne}}$	η^*	Δ_η
2.974	0.0015	0.07	1.64	1.94	0.55

From Table 5.6, the failure probability is very low, equal 0.15%. The corresponding most likely failure point of ε_{ne} is 0.07 and η is 1.94. The partial safety factors are estimated by dividing the above checking points by their mean values, respectively.

The Level 3 reliability is also calculated by employing Eq. 5.41. The probability

of failure is formulated as follows:

$$
\begin{aligned}
P_f &= P\{M \leqslant 0\} \\
&= P\{\varepsilon_f \leqslant \varepsilon_{ne}[\zeta(1+2\sqrt{\frac{2}{1+\eta^2}})]^{\frac{2}{n_0+1}}\} \\
&= 1 - P\{0 \leq \varepsilon_{ne} \leq \frac{\varepsilon_f}{[\zeta(1+2\sqrt{\frac{2}{1+\eta^2}})]^{\frac{2}{n_0+1}}}\} \\
&= 1 - \int_0^{\infty} \int_0^{\frac{\varepsilon_f}{[\zeta(1+2\sqrt{\frac{2}{1+\eta^2}})]^{\frac{2}{n_0+1}}}} f_{\eta,\varepsilon_{ne}}(\eta, \varepsilon_{ne}) d\varepsilon_{ne} d\eta \\
&= 1 - \int_0^{\infty} \int_0^{\frac{\varepsilon_f}{[\zeta(1+2\sqrt{\frac{2}{1+\eta^2}})]^{\frac{2}{n_0+1}}}} f_{\eta}(\eta) * f_{\varepsilon_{ne}}(\varepsilon_{ne}) d\varepsilon_{ne} d\eta \\
&= \int_0^{\infty} \frac{1}{\eta\sqrt{2\pi}\sigma_1} exp - \frac{(ln(\eta)-\mu_1)^2}{2{\sigma_1}^2} [\int_0^{\frac{\varepsilon_f}{[\zeta(1+2\sqrt{\frac{2}{1+\eta^2}})]^{\frac{2}{n_0+1}}}} \frac{1}{\varepsilon_{ne}\sqrt{2\pi}\sigma_2} exp - \frac{(ln(\varepsilon_{ne})-\mu_2)^2}{2{\sigma_2}^2} d\varepsilon_{ne}] d\eta
\end{aligned}
\tag{5.77}
$$

Eq. 5.77 is numerically evaluated by the Matlab [64] application. The calculated failure probability is 0.0015 which is in an excellent agreement with Level 1 reliability calculation.

For the same ship hull bottom shell, under the same nominal strain, but without corrosion, the failure probability is also evaluated by the limit state as shown in Eq. 5.78.

$$M = \varepsilon_f - \varepsilon_{ne} \tag{5.78}$$

The failure probability is simply $P(M \leq 0) = P(\varepsilon_f \leq \varepsilon_{ne})$. Calculation shows that the failure probability is 7.43×10^{-6}, extremely small. So compared to this failure probability of a non-corroded ship hull plate, corrosion does bring in a much higher failure probability and such plates thus needs attention in operation.

Furthermore, the Level 1 reliability study is performed on the same example with the mean value of nominal strain ε_{ne} equal to 0.084, double of the previous mean value. The results are shown in Table 5.7. Under a higher nominal strain, the failure

probability increases dramatically from 0.0015 to 0.1808. The partial safety factor of ε_{ne} is closer to 1, which indicates that this higher mean value of ε_{ne} gets closer to the critical value; meanwhile, the partial safety factor of η increases from 0.55 to 0.77, which means that with a relative shallow pit, the bottom shell will fail with a high probability. However, the failure probability of non-corroded plate under the nominal strain, whose mean value is 0.084, is 1.28×10^{-5}. The failure probability increases but not as rapidly as that of a corroded plate. This is exactly because of the appearance of pit corrosion. These calculations again show the deteriorating effect of pit corrosion on a plate capacity; thus, pit-corroded structure should be given certain attention during its operation.

Table 5.7: Level 1 reliability calculation for an oil tanker dented bottom shell in ship grounding for the mean value of ε_{ne} equal to 0.084

β	P_f	ε^*_{ne}	$\Delta_{\varepsilon_{ne}}$	η^*	Δ_η
0.912	0.1808	0.09	1.05	2.70	0.77

5.5 Conclusion

Neuber's elastic and inelastic stress concentration theory are applied with success on the stress and strain concentration caused by corrosion pits on plates. Finite element method shows its capability and accuracy to calculate the stress concentration factor for pit-corroded plates. A meshing sensitivity study is conducted to show how sensitive this problem to meshing and also is applied to predict the exact solution based on available numerical ones. Agreement is achieved with success between Neuber's analytical solution and the finite element study prediction.

A new method of incorporating the stress and strain concentration factor in the reliability study is developed for pit-corroded plate to further provide the failure

probability under uncertain loading conditions. In this new method, the partial safety factors of both pit geometry and the nominal stress or strain are provided for a prediction of the possible most likely failure points.

CHAPTER 6

Conclusions and Future Work

6.1 Conclusions

The corrosion effects on the ductile fracture, buckling and reliability of membranes, plates and shells have been addressed. The study is divided into four main parts: nonlinear elastic annular membrane problem; pit corrosion effect on ductile fracture initiation induced by strain localized plates; bending capacity study of corroded pipelines and pit corrosion induced stress and stress/strain concentration reliability analyses. For these analyses, analytical derivations finite element analyses and experimental testing programs are conducted. The corresponding failure modes: ductile fracture and buckling are critical for corroded ship hull and offshore structures. The study of these effects highlight the structural failure mechanism variation as a result of pit corrosion. The reliability study of corroded plates merits critical failure prediction in structure design. Detailed conclusions are summarized in the following:

- The nonlinear axisymmetric elastic annular membrane problem is solved for prescribed edge loading. Vertical and horizontal displacements and radial and circumferential stresses of the membrane are determined. Axisymmetric closed-form solutions for membrane displacements are derived for all possible Poisson's ratios, some of which are not found from previous literatures.

- Analytical solutions are provided with particular emphasis on solutions for various values of the constant a_2. Solutions show that a_2 is an important constant proportional to the membrane radial strain. Bifurcation of solutions occurs for some cases in which $a_2 < 0$. Also, the small slope assumption of the Föppl theory corresponds to a certain range of the constant a_2. Under certain boundary conditions ($u(r_i) = u(r_a) = w(r_a) = 0$), for Poisson's ratio equal to $\frac{1}{3}$, zero membrane radial displacement is found. Under these circumstances, positive a_2 corresponds to positive radial displacement and negative a_2 to negative radial displacement.
- Closed-form solutions are derived for both friction and frictionless indentor conditions. By applying various vertical displacements at the inner radius, the center load needed is calculated for both cases for materials with different Poisson's ratio. As expected, in the frictionless case, the center load needed is smaller than that in the friction case.
- Furthermore, the comparisons are made to Schwerin's [96] studies and Tuan's [112] ponding problem, respectively. Finite element analysis is employed to simulate Tuan's ponding problem for a comparison of membrane vertical displacement and Von Mises stress. Excellent agreements are achieved for both comparisons, which again validates the accuracy of the derived analytical solutions.

- In the study of ductile fracture initiation on pit-corroded plates, we have developed models for predicting rupture strain for power law plastic material with corrosion pit imperfections: a $3D$ model based on the finite element method. The results are compared to those of a $1D$ model based on a single localization zone. Similar trends of the overall average strain dependency on model length

confirm the application of $1D$ model on the analysis of pit-corroded plate ductile fracture initiation. Both models provide quantitative relationships for size effects relating overall length to strain-to-failure. This is valuable for the element size decision in the pit-corroded plate modeling. Both models also indicate a strong reduction in fracture elongation in the presence of imperfections caused by corrosion pits. The pit corroded plate fracture initiation study is also extended to plates under different biaxial loading conditions, with different pit intensities and pit distributions. Under two fracture failure criteria, far field effective plastic strain level is calculated according to various loading conditions.

- The $3D$ model is more capable of accurately capturing effects of general geometric imperfections including arbitrary corrosion pit shapes.
- Using the local maximum effective strain criterion, the far field fracture strain is not strongly dependent on pit intensity and distribution. Under biaxial tension conditions, corroded plates are less susceptible to fracture; a nearly constant strain amplification factor is found regardless of loading ratio under biaxial loading condition.
- Using the local maximum shear stress criterion, higher strain localization is revealed again in the pit corroded plate than in the uniform corroded plate. Pit distribution is also a factor influencing corroded plate deformation.
- Pit distribution influences plate deformation differently under biaxial tension and under tension-compression for a given failure criterion. Therefore, to confirm this point, plates under other loading conditions, such as biaxial compression or even bending, are suggested to study in the future.
- As the stress distribution at the far field is not uniform, difficulties occur

to quantify the far field or global fracture stress levels under the displacement control. How pit geometries and loading conditions affect the stress distribution is recommended in the future study.

- In the study of bending capacity of corroded pipelines, an experimental testing program is preformed to test the corrosion effect on pipeline's bending capacity. Test results verify the finite element analysis results. Key issues in modeling and analyzing this test program in FE is discussed in great detail.
  - Corrosion reduces the pipes bending capacity.
  - Finite element studies show that for the accurate computation of bending capacity of corroded pipelines: quadratic brick or tetrahedral elements are recommended; accurate modeling of the edge smoothness of the LTA was not important; and some examples of adequate refinement are given in the thesis. Properly executed, the finite element approach recommended accurately predicts the maximum moment capacity of a corroded cross section, and the buckled shape.
  - Significant secondary effects are apparent from the experimental measurements. Due to experimental setup, a gross tensile loading develops in the specimen that affects the bending moment. Using a full-scale FEA model, this tensile force was analyzed. Such test set-ups thus produce both moment and a (stabilizing) axial force. Moment capacity prediction may thus be unconservative. The end cap also contributed to the moment capacity reported from the test. The best approach is to carefully include both the end cap loading and the gross tensile load that develops due to the test setup.

- For this D/t ratio and strength (i.e. $D/t = 17.25$, $X - 52$), the application of an internal pressure reduced the LTA's bending capacity. For large D/t specimens where the compressive buckling initiates elastically, internal pressure has the potential of increasing the moment capacity. This effect merits further study.

- Neuber's elastic and inelastic stress concentration theory are applied with success on the stress and strain concentration caused by corrosion pits on plates. Finite element analysis shows its capability and accuracy to calculate the stress concentration factor for pit-corroded plates. A meshing sensitivity study is conducted to show how sensitive this problem to meshing and also is applied to predict the exact solution based on available numerical ones. Agreement is achieved with success between Neuber's analytical solution and the finite element study prediction.

  A new method of incorporating the stress and strain concentration factor in the reliability study is developed for pit-corroded plates to further provide the failure probability under uncertain loading conditions. In this new method, the partial safety factors of both pit geometry and the nominal stress or strain are provided for a prediction of the possible most likely failure points.

6.2 Future Work

Some effects of pit corrosion on representative structures mechanical failures have been analyzed. Nevertheless, more challenges and opportunities are presenting themselves on this topic so that my research can be extended in the following directions:

Based on the available axisymmetrical elastic membrane closed-form solutions, membrane instability analysis can be conducted. For a negative a_2 two membrane

deformation status are found, both resulting in compressive radial stress. From Fig. 2.7, the membrane deformation is different between the two. Detailed studied are suggested to seek the reasons for the existence of both status corresponding to the same a_2.

In the ductile fracture initiation of pit-corroded plate, studies address importance of applying other combined loading conditions on the pit-corroded plate. Meanwhile, they also show the complex and less-systematic qualities of these studies. In order to develop a methodology including pit geometry, intensity and loading condition, a detailed database may be needed, which may take years and tremendous effort. Experimental tests and finite element methods are powerful tools to assist the study. However, to quantify the time effect in corrosion in either method requires further study.

In the study of bending capacity of corroded pipelines, further work is proposed to investigate the internal pressure effect on corroded pipes of various dimensions and grades. Also future work is to be done by using the finite element models for the assessment of bending capacity for the generation of simplified closed form formulas for corroded pipelines only under bending, which is similar to $B31G$ for internal pressure.

Base on the study, a time-dependent reliability analysis of the corroded structure failure is promising and capable to including additional random factors. This, however, requires a long-time recorded, real database to quantify random factors, especially the pit geometry variation and pit propagation time-dependency. By including such information, predictions of failure probability and random variables' partial safety factors will merit future structure design. An approximation is made on the pit elastic stress concentration factor. For an accurate stress/strain concentra-

tion prediction, efforts need to put on the analytical solution derivation; or employing finite element method may be an alternative route.

For the exploration of some pit corrosion effects on structure failure study, the modeling of pit corrosion is limited to an idealized representative center pit. This simplification benefits the study in the initial step to reveal the fundamental mechanism while keeping the calculation possible. However, to properly model real scenarios, complex and real corrosion modeling and complex loading conditions need to be considered. To include all these information may result in long, challenging work.

BIBLIOGRAPHY

Bibliography

[1] *Evaluation of Approximate Methods for Elastic-Plastic Analysis of Notched Bodies*, Proceedings of Third International Conference on Localized Damage, Computer Aided Assessment and Control, 1994.

[2] *Plastic Collapse Load for Vessel with External Flaw Simultaneously Subjected to Bending*, Proceedings of PVP2007, 2007.

[3] Version 6.7 ABAQUS/Standard Users Manual. Hibbitt, Karlsson and Sorensen, Pawtucket, RI 12860, Inc.

[4] J. Aitchison and J. A. C. Brown. *The Lognormal Distribution with Special Reference to its Uses in Economics*. Cambridge University Press, 1976.

[5] Unyime O. Akpan, T. S. Koko, B. Ayyub, and T. E. Dunbar. Risk assessment of aging ship hull structures in the presence of corrosion and fatigue. *Marine Structures*, 15:211–231, 2002.

[6] H. K. Amlashi and T. Moan. On the strength assessment of pitted stiffened plates under biaxial compression loading. In *Proceedings of the 24th international conference on offshore mechanics and arctic engineering*, 2005.

[7] A. H-S. Ang and W. H. Tang. *Probability Concepts in Engineering Planning and Design, Vol.2-Decision, Risk and Reliability*. John Wiley and Sons, Inc., 1983.

[8] ASME. Asme b31g, manual for determining the remaining strength of corroded pipelines. Technical report, ASME, 1991.

[9] A. Atsumi and S. Itou. Preprint of jsme, 761-1 1967. 343.

[10] B. M. Ayyub and A. Haldar. Practical structural reliability technique. *Journal of structural engineering*, 110:1707–1724, 1984.

[11] Bilal M. Ayyub and Gregory J. White. Reliability-conditioned partial safety factors. *Journal of structural engineering*, 113:279–294, 1987.

[12] Yong Bai and Ruxin Song. Reliability-based limit-state design and re-qualification of pipelines. In *17th International Conference on Offshore Mechanics and Arctic Engineering*, 1998.

[13] Y. Bao and T. Wierzbicki. On fracture locus in the equivalent strain and stress triaxiality space. *International Journal of Mechanical Sciences*, 46(1):81–98, 2004.

[14] Armin Beck and Hans Grabmuller. Wrinkle-free solutions of circular membrane problems. *Zeitschrift fur Angewandte Mathematik und Physik*, 43:481–504, 1992.

[15] Matthew R. Begley and Thomas J. Mackin. Spherical indentation of freestanding circular thin films in the membrane regime. *Journal of the Mechanics and Physics of Solids*, 52:2005–2023, 2004.

[16] Authur P. Boresi, Richiard J. Schmidt, and Omar M. Sidebottom. *Advanced Mechanics of Materials*. John Wiley ans Sons, Inc., 1993.

[17] B. Budiansky and O. L. Mangasarian. Plastic stress concentration at a circular hole in an infinite sheet subjected to equal biaxial tension. *J. Applied Mechanics*, 1:59–64, 1960.

[18] B. Budiansky and R. J. Vidensek. Analysis of stresses in the plastic range around a circular hole in a plate subjected to uniaxial tension. Technical report, 1955.

[19] F. M. Burdekin. General principles of the use of safety factors in design and assessment. *Engineering Failure Analysis*, 14:420–433, 2007.

[20] Andrew J. Callegari and Edward L. Reiss. Non-linear boundary value problems for the circular membrane. *Arch. Ration. Mech. Anal.*, 31:390–400, 1968.

[21] Andrew J. Callegari, Edward L. Reiss, and Herbert B. Keller. Membrane buckling: A study of solution multiplicity. *Comm. Pure Appl. Math.*, 24:499–516, 1971.

[22] D. Chen and S. Cheng. Non-linear analysis of prestretched circular membrane and a modified iteration technique. *Int. J. Solids Structures*, 33:545–553, 1996.

[23] A. Considere. Memoire sur l'emploi du fer et de l'acier dans les constructions. *Annales des Ponts et Chausses ser*, 6(9):574–775, 1885.

[24] Edwin L. Crow and Kunio Shimizu, editors. *Lognormal Distributions: Theory and Applications*. Marcel Dekker, Inc, New York and Basel, 1988.

[25] G. David and J. D. Humphrey. Redistribution of stress due to a circular hole in a nonlinear anisotropic membrane. *Journal of Biomechanics*, 37:1197–1203, 2004.

[26] R. W. Dickey. The plane circular elastic surface under normal pressure. *Arch. Ration. Mech. Anal.*, 26:219–236, 1967.

[27] R. W. Dickey. The nonlinear circular membrane under a vertical force. *Quarterly of Applied Mathematics*, 41:331–338, 1983.

[28] J. K. Dienes and J. W. Miles. A membrane model for the response of thin plates to ballistic impact. *Journal of the Mechanics and Physics of Solids*, 25:237–256, 1977.

[29] DNV. Buckling strength analysis. Technical report, Det Norske Veritas, 1995.

[30] A. H. Dunbar. A computational investigation of the effects of localized corrosion on plates and stiffened panels. *Marine Structures*, 17:385–402, 2004.

[31] R. A. Eubanks. Stress concentration due to a hemispherical pit at a free surface. *Journal of Applied Mechanics*, 3:57–62, 1954.

[32] A. Foppl. *Vorlesungen Uder Technische Mechanik*. Leipzig Druck Und Verlag, 1907.

[33] M. M. Frocht and D. Landsberg. Factors of stress concentration due to elliptical fillets. *J. Applied Mechanics*, 26:448–450, 1959.

[34] T. et al. Fujita. Scientific and engineering reports of the defense academy. Technical Report 4, 12 1975. 599.

[35] A. Ghosh. Tensile instability and necking in materials with strain hardening and strain-rate hardening. *Acta Metallurgica*, 25:1413–1424, 1977.

[36] H. Grabmuller and E. Novak. Nonlinear boundary value problems for the annular membranes: A note on uniqueness of positive solutions. *Journal of Elasticity*, 17:279–84, 1987.

[37] A. Gurson. Continuum theory of ductile rupture by void nucleation and growth: Part i-yield criteria and flow rules for porous ductile media. *Journal of Engineering materials and Technology*, 99(1):2–15, 1977.

[38] L-H. Han, S-Y. He, Y-P. Wang, and C-D. Liu. Limit moment of local wall thinning in pipe under bending. *Int J Press Vessels Piping*, 76:539–542, 1999.

[39] G. Harkegard and T. Mann. Neuber predictionof elastic-plastic strain concentration in notched tensile specimens under large-scale yielding. *J. Strain Analysis*, 38:79–94, 2003.

[40] G. Harkegard and S. Sorbo. Applicability of neuber's rule to the analysis of stress and strain concentration under creep conditions. *Trans. ASME J. Engineering Material Technology*, 120:224–229, 1998.

[41] E. W. Hart. Theory of the tensile test. *Acta Metallurgica*, 15:351–355, 1967.

[42] Hartmann and Leven. Factors of stress concentration for the bending case of fillets in flat bars and shafts with central enlarged section. *Proc. Soc. Exp. Stress Anal. 9*, 1:53–62, 1951.

[43] A. M. Hasofer and N. C. Lind. Exact and invariant second moment format. *Journal of the Engineering Mechanics Division, ASCE*, 100:111–121, 1974.

[44] H. Hencky. Uber den spannungszustand in kreisrunden platten mit verschwindender biegungssteifigkeit. *Zeitschrift fur Mathematik und Physik*, 63:311–317, 1915.

[45] M. Hetenyi. Stress concentration factors for t-heads. *Journal of Applied Mechanics*, 26:130–132, 1959.

[46] CEB-CECM-CIB-FIP-IABSE-IASS-RILEM Joint Committee on Structural Safety. First order reliability concepts for design codes. CEB Bulletin No.2, July 1976.

[47] CEB-CECM-CIB-FIP-IABSE-IASS-RILEM Joint Committee on Structural Safety. General principles on reliability for structural design. International Association for Bridge and Structural Engineering, 1981.

[48] A. Kanvinde and G. Deierlein. Void growth model and stress modified critical strain model to predict ductile fracture in structural steels. *Journal of Structural Engineering*, Dec.:1907–1918, 2006.

[49] Von Karman. Festigkeitsprobleme in maschinenbau. *Encyklopadie Der Mathematischen Wissenschaften, Teubner*, IV/4:311–385, 1910.

[50] A. Kelkar, W. Elber, and I. S. Raju. Large deflections of circular isotropic membranes subjected to arbitrary axisymmetric loading. *Computers and Structures*, 21:413–421, 1985.

[51] J. W. Kim and C. Y. Park. Effect of length of thinning area on the failure behavior of carbon steel pipe containing a defect of wall thinning. *Nuclear Engineering and Design*, 220:274–284, 2003.

[52] Y. J. Kim, D. J. Shim, K. N., Y. J. Kim, J. S. Kim, and S. S. Hwang. Finite element based plastic limit loads for cylinders with part-through surface cracks under combined loading. *International Journal of Pressure Vessels and Piping*, 80:527540, 2003.

[53] Yun-Jae Kim, Do-Jun Shim, Young-Jin Kim, and Hwan Lim. Reference stress based approach to predict failure strength of pipes with local wall thinning under single loading. *ASME J. Pressure Vessel Technol.*, 126(2):194–201, 2004.

[54] Y. Kobayashi, Y. Tanaka, H. Goto, K. Matsuoka, and Y. Motohashi. Effects of stress concentration factors on corrosion fatigue strength of a steel plate for ship structures. *Key Engineering Materials*, Fracture and Strength of Solids III:1037–1042, 1998.

[55] G. V. Kolosov. *On the Application of Complex Function Theory to a Plane Problem of the Mathematical Theory of Elasticity (In Russian).* Yuriev, 1909.

[56] F. K. Kong and R. H. Evans. *Reinforced and Prestressed Concrete*. Van Nostrand Reinhold (UK) Co. Ltd, 1986.

[57] E. Lehr. *Spannungsverteilung in Konstruktionselementen*. Berlin, 1934.

[58] Y. Li. *Ductile Fracture due to Localization and Void Growth for 3D Randomly Voided Materials*. PhD thesis, University of Michigan, 2007.

[59] Y. Li and Dale G. Karr. Prediction of ductile fracture in tension by bifurcation, localization, and imperfection analyses. *International Journal of Plasticity*, 25:1128–1153, 2009.

[60] Y. Li, Dale G. Karr, and Ge Wang. Mesh size effects in simulating ductile fracture of metals. In *The 10th International Symposium on Practical Designs of Ships and Floating Structures (PRADS), Houston, TX, 815-822*, 2007.

[61] K. Lu. Finite element analysis of membrane wrinkling. *International journal for numerical methods in engineering*, 50:1015 –1038, 2001.

[62] L. Malvern. *Introduction to the Mechanics of a Continuous Medium*. Prentice-Hall, Inc., Englewood Cliffs, New Jersey, 1969.

[63] Alaa E. Mansour. An introduction to structural reliability theory. Technical report, Ship Structure Committee, 1989.

[64] Matlab. The MathWorks, Inc, 2006.

[65] F. McClintock. A criterion for ductile fracture by the growth of holes. *Journal of Applied Mechanics*, 39(2):363–371, 1968.

[66] R. E. Melchers. *Structural Reliability Analysis and Prediction*. Ellis Horwood Limited, 1987.

[67] Minitab. The Minitab, Inc, 2009.

[68] Katsumasa Miyazaki, Satoshi Kammo, Masayuki Ishiwata, Kunio Hasegawa, Soek Hwan Ahn, and Kotoji Ando. Fracture and general yielding for carbon steel pipes with local wall thinning. *Nuclear Engineering and Design*, 200:61–68, 2002.

[69] Daisuke Mori, Guido David, Jay D. Humphrey, and James E. Moores. Stress distribution in a circular membrane with a central fixation. *Journal of Biomechanical Engineering*, 127:549–553, 2005.

[70] C. M. Muscat-Fenech and A. G. Atkins. Denting and fracture of sheet steel by blunt and sharp obstacles in glancing collisions. *Int. J. Impact Engng*, 21:499–519, 1998.

[71] T. Nakai, H. Matsushita, and N. Yamamoto. Effect of pitting corrosion on local strength of hold frames of bulk carriers-lateral-distortional buckling and local face buckling (2nd report). *Marine Structures*, 17:612–641, 2004.

[72] T. Nakai, H. Matsushita, and N. Yamamoto. Pitting corrosion and its influence of local strength of hull structural members. In *Proceedings of the 24th international conference on offshore mechanics and arctic engineering (OMAE2005), OMAE2005-67025*, 2005.

[73] T. Nakai, H. Matsushita, and N. Yamamoto. Effect of pitting corrosion on strength of web plates subjected to patch loading. *Thin-walled structures*, 44:10–19, 2006.

[74] T. Nakai, H. Matsushita, and N. Yamamoto. Effect of pitting corrosion on ultimate strength of web plates subjected to shear loading. *Key Engineering Materials*, 340-341:489–494, 2007.

[75] T. Nakai, H. Matsushita, N. Yamamoto, and H. Arai. Effective of pitting corrosion on local strength of hold frames of bulk carriers (1st report). *Marine Structures*, 17:403–432, 2004.

[76] H. Neuber. Theory of stress concentration for shear-strained prismatical bodies with arbitrary nonlinear stress-strain law. *Transactions of ASME*, 12:544–550, 1961.

[77] H. Neuber and H. G. Hahn. Stress concentration in scientific research and engineering. *Applied Mechanics Reviews*, 19:187–199, 1966.

[78] Heinz Neuber. *Theory of Notch Stresses Principles for Exact Stress Calculation*. Edwards Brothers, Inc, Ann Arbor, Michigan, 1946.

[79] Nippon. Transactions of nippon kaiji kyoukai, 1991. 217, 237-252.

[80] Nippon. Transactions of nippon kaiji kyoukai, 1995. 230, 16-24.

[81] D. Ok, Y. Pu, and A. Incecik. Computation of ultimate strength of locally corroded unstiffened plates under uniaxial compression. *Marine Structures*, 20:100–114, 2007.

[82] J. K Paik, J.M. Lee, and M. J. Ko. Ultimate compressive strength of plate elements with pit corrosion wastage. *Journal of Engineering of the Maritime Environment*, 217:185–200, 2003.

[83] J. K Paik, J.M. Lee, and M. J. Ko. Ultimate shear strength of plate elements with pit corrosion wastage. *Thin-walled structures*, 42:1161–1176, 2004.

[84] J. K. Paik and A. K. Thayamballi. *Ultimate Limit State Design of Steel-Plated Structures*. Wiley, New York, 2003.

[85] Vladmir Panc. Theory of elastic-plastic stress state for shear-strained prismatical bodies with symmetrical sharp notches. *ACTA TECHNICA CSAV*, 3:282–299, 1965.

[86] J. Parunov and C. Guedes Soares. Effects of common structural rules on hull-girder reliability of an aframax oil tanker. *Reliability Engineering and System Safety*, 93:1317–1327, 2008.

[87] J. A. Pelesko and X. Y. Chen. Electrostatic deflections of circular elastic membranes. *Journal of Electrostatics*, 57:1–12, 2003.

[88] R. H. Plaut. Linearly elastic annular and circular membranes under radial, transverse, and torsional loading. part i: Large unwrinkled axisymmetric deformations. *Acta Mech.*, 202:79–99, 2009.

[89] R. H. Plaut. Linearly elastic annular and circular membranes under radial, transverse, and torsional loading. part ii: Vibrations about deformed equilibria. *Acta Mech.*, 202:101–110, 2009.

[90] R. Rackwitz and B. Fiessler. Structural reliability under combined random load sequences. *Computers and Structures*, 9:489494, 1978.

[91] E. Reissner. Note on membrane theory of shells of revolution. *Journal of Mathematics and Physics*, 26:290–293, 1948.

[92] E. Reissner. On axisymmetrical deformation of thin shells of revolution. *Prc. Symp. Appl. Math.*, III:27–52, 1950.

[93] Christopher J. Roy. Review of code and solution verification procedures for computational simulation. *Journal of Computational Physics*, 205:131–156, 2005.

[94] S. Roy, S. Grigory, M. Smith, M. F. Kanninen, and M. Anderson. Numerical simulations of full-scale corroded pipe tests with combined loading. *ASME J. Pressure Vessel Technology*, 119:457–466, 1997.

[95] K. Saito and I. Nakahara. Transactions of japan soc. mech. engrs., 3 1967. 343.

[96] E. Schwerin. Uber spannungen und formanderungen kreisringformiger membranen. *Zeitschrift angewandte Mathematik und Mechanik*, 12:651–659, 1929.

[97] O. N. Scott, M. R. Begley, U. Komaragiri, and T. J. Mackin. Indentation of freestanding circular elastomer films using spherical indenters. *Acta Materialia*, 52:4877–4885, 2004.

[98] Timm Seeger and Paul Heuler. Generalized application of neuber's rule. *Journal of Testing and Evaluation, JTEVA*, 8:199–204, 1980.

[99] W. N. Sharpe and K. C. Wang. Evaluation of a modified monotonic neuber relation. *Journal of Engineering Materials and Technology*, 113:1–8, 1991.

[100] B. A. Shaw and R. G. Kelly. What is corrosion? *The Electrochemical Society Interface*, Spring:24–26, 2006.

[101] D. J. Shim, Y. J. Kim, and Y. J. Kim. Reference stress based approach to predict failure strength of pipes with local wall thinning under combined loading. *ASME J. Pressure Vessel Technol.*, 127:76–83, 2005.

[102] L. L. Shreir, R. A. Jarman, and G. T. Burstein, editors. *Corrosion.* Oxford ; Boston : Butterworth-Heinemann, 1994.

[103] B. Simonsen and R. Tornqvist. Experimental and numerical modeling of ductile crack propagation in large-scale shell structures. *Marine Structures*, 17:1–27, 2004.

[104] B. C. Simonsen. Ship grounding on rock-ii. validation and application. *Marine Structures*, 10:563–584, 1997.

[105] C. Guedes Soares and Y. Garbatov. Reliability of maintained ship hull girders subjected to corrosion and fatigue. *Structural Safety*, 20:201–219, 1998.

[106] C. Guedes Soares and Y. Garbatov. Reliability of maintained ship hulls subjected to corrosion and fatigue under combined loading. *Journal of Constructional Steel Research*, 52:93–115, 1999.

[107] Y. Sumi. Strength and deformability of corroded steel plates estimated by replicated specimens. In *10th international symposium on practical design of ships and other floating structures*, 2007.

[108] F. Teruaki, S. Takashi, T. Eiichiro, and N. Ichiro. Stress concentration due to a hemispherical pit at a free surface of a thick plate under all-round tension. *Bulletin of the JSME*, 21:561–565, 1978.

[109] P. Thoft-Christensen and M. J. Baker. *Structural Reliability, Theory and its Application.* Springer-Verlag, 1982.

[110] C. H. Tsao, A. Ching, and S. Okubo. Stress-concentration factors for semielliptical notches in beams under pure bending. *Expil. Mech. 5*, 3:19–23, 1965.

[111] E. Tsuchida and I. Nakahara. Transactions of japan soc. mech. engrs., 5 1967. 696.

[112] Christopher Y. Tuan. Ponding on circular membranes. *Int. J. Solids Structures*, 35:269–283, 1998.

[113] S. Valluri, D. Jeffrey, and R. Corless. Some applications of the lambert w function to physics. *Canad. J. Phys*, 78:823–831, 2000.

[114] Y. Wang. Current status and future directions for reliability analysis of ship structures under corrosion. *Chuan Bo Li Xue*, 11:307–320, 2007.

[115] Stewart Way. Bending of circular plates with large deflection. *American Society of Mechanical Engineers-Transactions*, 56:627–633, 1934.

[116] H. J. Weinitschke. On axisymmetric deformations of nonlinear elastic membranes. *Mechanics Today 5, S. Nemat-Nasser (ed.) (Reissner Anniversary Volume), Pergamon, Oxford*, pages 523–541, 1980.

[117] H. J. Weinitschke and Erlangen. On finite displacements of circular elastic membranes. *Mathematical methods on the applied sciences*, 9:76–98, 1987.

[118] T. Wierzbicki, Y-B Bao, Y-W Lee, and Y-L Bai. Calibration and evaluation of seven fracture models. *Int. J. of Mechanical Sciences*, 47:719–743, 2005.

[119] T. Wierzbicki and G. N. Nurick. Large deflection of thin plates under localized impulsive loading. *International Journal of Impact Engineering*, 18:899–918, 1996.

[120] Wikipedia.org. http://en.wikipedia.org.

[121] W. H. Yang and K. H. Hsu. Indentation of a circular membrane. *Journal of Applied Mechanics*, 38:227–230, 1971.

[122] Weiwei Yu, Hyun Chung, Ge Wang, and Dale G. Karr. Analysis of ductile fracture initiation in corroded plates. In *Proceedings of the 27th International Conference on Offshore Mechanics and Arctic Engineering*, 2008.

[123] Weiwei Yu and Dale G. Karr. Symmetrical solutions for edge-loaded annular elastic membranes. *Journal of Applied Mechanics*, 76:031010 1–7, 2009.

[124] S. Zhang. Plate tearing and bottom damage in ship grounding. *Marine Structures*, 15:101–117, 2002.

[125] M. Zheng, J. H. Luo, X. W. Zhao, G. Zhou, and H. L. Li. Modified expression for estimating the limit bending moment of local corroded pipeline. *International Journal of Pressure Vessels and Piping*, 81:725–729, 2004.